Call for Ideas: NEO Encounter 2029

NEO deflection through a multi-mirror system

Final Report

Authors: Massimiliano Vasile, Christie Alisa Maddock, Gianmarco Radice
Affiliation: Department of Aerospace Engineering, University of Glasgow, UK

Authors: Colin McInnes
Affiliation: Department of Mechanical Engineering, Strathclyde University, UK

ESA Researcher: Leopold Summerer

Date: 12 May 2009

Contacts:

Massimiliano Vasile
Tel: +44 (0)141 330 6465
Fax: +44 (0)141 330 5560
e-mail: m.vasile@aero.gla.ac.uk

Leopold Summerer
Tel: +31 (0)7156 55174
Fax: +31 (0)7156 58018
e-mail: act@esa.int

Available on the ACT website
http://www.esa.int/act

Ariadna ID: 08/4301
Study Duration: 4 months
Contract Number: 21665/08/NL/CB

Executive Summary

In 2004, astronomers first sighted the asteroid 2004 MN4, later to be named Apophis. Based on tracking data, it is known that in 2029 the asteroid will have a close approach with the Earth. Depending on the outcome of that fly-by, due to the interaction with the Earth's gravity field, it has the potential to set up two possible impact dates in 2036 and 2037. Apophis is only one of 4187 Near Earth Objects (NEO) currently being monitored, with 792 listed as potentially hazardous, out of an estimated 1–2 million. While the probability of an impact is currently very low, it is not impossible. It is estimated that on average, a 100 m diameter asteroid impacts every 100 years, an event equivalent to 2000 atomic bombs. Due the potential danger posed by an impact, many scientists in the last few decades have proposed several deflection methods.

Based on a quantitative comparison of the various options for NEO deflection, one of the more interesting and promising methods employs solar sublimation to actively deviate the orbit of the asteroid. The original concept envisioned a single large reflector; this idea was expanded by the authors to a formation of spacecraft orbiting in the vicinity of the NEO, each equipped with a smaller concentrator assembly capable of focusing the solar power at a distance around 1 km and greater. This relieved the strict constraint on the proximity to the asteroid surface, mitigating the effects of the inhomogeneous gravity field, as well as temperature concerns by the high magnification ratio. Furthermore, one of the critical aspects of this deflection concept is properly placing the concentrators in the proximity of the asteroid in order to avoid the plume impingement and the occultation from the asteroid itself.

Two concepts, and the corresponding dynamics and control, are presented based on previous trade-off and optimization studies. The first uses a paraboloidic reflector to concentrate the solar radiation onto a solar-pumped laser, which is then directed onto a specific spot on the NEO by a small directional mirror. The spacecraft orbits are designed to fly in formation with the asteroid around the Sun, and are based on the orbital element differences. The formation orbits were optimized for two objective functions, one minimizing the range while restricting the orbit to outside a limit sphere (in order to avoid the non-linearities of the close-proximity gravitation field of the asteroid), and the other maximizing the distance in the x-z plane in order to avoid the debris plume. A feedback control law is presented for the orbital maintenance required to counteract the solar radiation pressure (due primarily to the large surface area of the primary reflector), and the third-body effects due to the gravitational field of the asteroid.

The second option takes advantage of the balance between the gravity attraction of the NEO and solar pressure acting on the collector. Instead of using

a laser and directional mirror, the mirror focuses the light directly onto the asteroid surface, controlling the beam by adjusting the focal point of the primary reflector. By altering the shape of the mirror surface, both the focal point and the vector of the solar radiation pressure (SRP) can be manipulated. This has the advantage of being frequency independent, compared to the laser which is restricted to a given wavelength but is in closer proximity to the asteroid. A minimal amount of control, on the order of 10^{-5} N, is required to keep the spacecraft at an artificial equilibrium point, which oscillates with true anomaly.

A key requirement for the successful implementation of the multi-mirror approach is that each spacecraft must know their position relative to both the NEO and the other spacecraft in the formation, and be able to find and maintain the direction of the beam onto a precise spot on the surface of the asteroid. In this paper we propose a navigation strategy based on the attitude measurements, the inertial position of each spacecraft, the intersatellite position and velocity measurements, and a 2D image from a rotating onboard camera. Once the formation is deployed in the vicinity of the NEO one spacecraft is temporarily designated as leader and searches the predicted location of the NEO until it is within the field of view of the camera. Using simple geometry, the centroid of the image is determined, and aligned with the boresight of the camera. The pointing vector from the lead spacecraft is then relayed to the whole formation. Once all the spacecraft have acquired the center of the NEO, the spacecraft-asteroid range can be triangulated. Each of these estimations on the position of the NEO can be fed into a batch filter and used for both the orbital control of the spacecraft and for directing the beams.

The results of simulations of a hypothetical deflection mission of the NEO Apophis are presented for the dynamics, control, attitude and navigation, accounting for solar radiation pressure, the gravity field of the asteroid, and the deviation of the NEO orbit.

At the end of this report we present a preliminary design budget with an estimation of the mass of each spacecraft in the formation for both the analysed concepts.

The results in this paper show that both concepts provide the required deflection with a feasible mass at launch, solving most of the issues related to the solar sublimation method. Although some of the pieces of technology required for the efficient implementation of this deflection method are currently at TRL 2, this study demonstrates that both concepts are feasible with components that are currently at or expected to be at a higher TRL in few years, independent of the development of the solar sublimation method.

Acknowledgments

The authors of this report would like to thank Dr. Marco Molina, head of the thermo-mechanical division of Gavazzi Space, for his suggestions on the conceptual analysis of the cooling system for the laser options and Dr. Marc Sorel from the Electronics Engineering department at the University of Glasgow for his help on the current and future state of the art for semiconductor lasers and innovative solar arrays.

Furthermore, though this study was performed by Christie Maddock and Massimiliano Vasile (the PI of this activity) with the contribution of Prof. Colin McInnes, the authors would like to thank Camilla Colombo and Joan Pau Sanchez Cuartielles of the Glasgow Space Advanced Research Team for their work on, respectively, the development of the analytical deflection formulas and of the thrust model for the solar sublimation method.

Contents

Nomenclature

Acronyms

AEP	Artificial Equilibrium Points
ATSM	American Society for Testing and Materials
AU	Astronomical Unit (149597870.7 km)
CCD	Charged Coupled Device
CFRP	Carbon Fibre Reinforced Plastic
FEEP	Field Emission Electric Propulsion
FOV	Field of View
GEO	Geosynchronous Earth Orbit
IAE	Inflatable Antenna Experiment
IR	Infra-red
LEO	Low Earth Orbit
MJD	Modified Julian Days, days
MJD2000	Modified Julian Days since 01 January 2000 12:00:00 GMT, days
MOID	Minimum Orbital Interception Distance
NEO/A	Near Earth Object/Asteroid
RAAN	Right Ascension of the Ascending Node (Ω)
RF	Radio Frequency
SRP	Solar Radiation Pressure
SpaceART	University of Glasgow Space Advanced Research Team
TRL	Technology Readiness Level
UV	Ultra-violet

Variables

a	Semi-major axis, m
$[a_I, b_I, c_I]$	Radial dimensions of an ellipse, m
A	Area, m^2
$\mathbf{A}$	Matrix of Gauss planetary equations (for use in a least-squares solution)
c	Speed of light (299792.458 km/s^2) or heat capacity (J/kg·K)
C_r	Concentration ratio
C_{20}, C_{22}	Harmonic coefficients for a second-order, second-degree gravity field
C_{ineq}	Inequality constraint in optimisation
d	Diameter, m
D	Search space for a solution vector
$\mathbf{D}$	Directional cosine matrix

e	Eccentricity
$\mathbf{e}$	Euler vector
E	Energy, J
E_a	Activation energy, J
f_ℓ	Optical focal length, m
$\mathbf{F}, F$	Force, N
i	Inclination, rad
I_{sp}	Engine specific impulse, s
h	Angular momentum, or height, m
H	Enthalpy of sublimation, J
l	Length, m
L	Distance, or depth, from the surface of the asteroid, m
j_c	Jet constant
J	Objective function
$\mathbf{k}$	Set of Keplerian orbital parameters $[a, e, i, \Omega, \omega, \nu]$
$\delta\mathbf{k}$	Set of Keplerian orbital element differences between two orbits, $[\delta a, \delta e, \delta i, \delta\Omega, \delta\omega, \delta M]$
K	Conductivity of a material, W/m·K
m	Mass, kg
M	Mean anomaly, rad
n	Mean motion, m/s or index of refraction
n_{sc}	Number of spacecraft in the formation
$\mathbf{n}$	Normal vector
q	Quaternions
Q, Q^*	Control functions
Q_{rad}	Heat loss due to radiation, J
Q_{cond}	Heat loss due to conduction, J
p	Semi-latus rectum, m
$\mathbf{p}$	Set of points on the surface of simulated NEO mapped onto the 2D camera plane
P	Power, W
P_0	Solar power at 1 AU (S_0/c), W
px	Pixel, m
$\mathbf{r}, r$	Position or radius, m
$\bar{R}$	Gas constant (8.314472 J/K·mol)
$\mathbf{s}$	Acceleration induced by solar radiation pressure, m/s^2
S_0	Solar flux at a distance of 1 AU (1367 W/m^2)
t	Time, s
$\bar{t}_{res}$	Average time of residence of a contaminant on a surface, s
T	Temperature, K
T_{A}	Orbital period of the NEA, days
$u, \mathbf{u}$	Control acceleration, m/s^2
U_{20+22}	Gravitational potential function for a second-order, second-degree gravity field
$\mathbf{v}, v$	Velocity, m/s
$\bar{v}$	Average velocity of particles according to Maxwell's distribution of an ideal gas, m/s
w	Rotational velocity, rad/s
W	Weights

Λ	Scattering factor
Ω	Right ascension of the ascending node (RAAN), rad
Θ	Elevation angle of spacecraft in the asteroid Hill reference frame $\mathcal{A}$, rad
α	Absorptivity, %
$\alpha_{in}, \alpha_{out}$	In-plane and out-of-plane thrust angles for control, rad
β	Sun aspect angle, rad
$\Delta\beta$	Angle between the incoming sunlight and the direction of the focal point of the mirror, rad
γ	Angular out-of-plane component in gravity field, rad
ϵ	Elevation angle of the artificial equilibrium point, rad
$\epsilon_\square$	Emissivity
ζ	Variable used in calculation of $\delta r(\delta\mathbf{k})$
η	Efficiency, %
θ	True latitude ($\nu + \omega$), rad
κ	Angular in-plane component in gravity field, rad
λ	Wavelength, m
μ	Gravitational constant ($\mu_\odot = 132724487690$ km^3/s^2)
ν	True anomaly, rad
ξ	Variable used in calculation of $\delta r(\delta\mathbf{k})$
ρ	Density, g/m^2
$\sigma_\square$	Coefficient of reflectivity, %
σ	Stefan-Boltzmann constant ($5.670400E$-8 W/m^{2}K^4)
τ	Torque, N·m
τ_0	Oscillation period of a molecule, s
ϕ	Angle of reflection between mirror normal and incoming (or outgoing) ray, rad
χ	Thermal diffusivity of the material
ψ	Euler angle, rad
ω	Argument of periapsis, rad
ϖ	Variable used in calculation of $\delta r(\delta\mathbf{k})$
ϱ	Variable used in calculation of $\delta r(\delta\mathbf{k})$

Subscripts

0	Initial value
A	Asteroid
AU	Value taken at a distance of 1 AU
dev	Deviation
exp	Expelled (mass)
i, j	i^{th} or j^{th} value in a set
$ineq$	Inequality (used with constraints in optimisation)
ir	Infra-red
f	Focal location or distance
g	Gap or hole in mirror to allow light to pass through to the other side
L	Laser
LIM	Limit or boundary condition
$light$	Light projected onto the asteroid

M	Mirror
max	Maximum allowable value
$pert$	Perturbations
R	Radiator
r	At distance r
rot	Rotational
sa	Solar arrys used for power conversion for the indirect pumped laser
sc	Spacecraft
sp	Solar panels
T	Target value
$spot$	Illuminated spot beam on asteroid surface
$\odot$,sun	Sun

Superscripts

$\mathcal{A}$	Relative rotating asteroid-centric Hill reference frame ($\hat{x}$ radial, $\hat{y}$ transverse, $\hat{z}$ normal)
$\mathcal{C}$	Relative rotating camera-centric reference frame ($\hat{z}$ in direction of boresight of camera field of view, $\hat{y}$ in direction of angular momentum)
$\mathcal{M}$	Relative rotating mirror-centric reference frame ($\hat{x}$ radial, $\hat{y}$ transverse, $\hat{z}$ normal)
$\mathcal{O}$	Inertial heliocentric reference frame ($\hat{x}$ is towards the vernal equinox Υ, $\hat{z}$ in normal to the Earth orbital plane)
$\mathcal{S}$	Relative rotating spacecraft-centric Hill reference frame ($\hat{x}$ radial, $\hat{y}$ transverse, $\hat{z}$ normal)

1 Introduction

1.1 Deflection of Near Earth Objects

Over the last few years, the possible scenario of an asteroid threatening to impact the Earth has stimulated intense debate among the scientific community about possible deviation methods. Small celestial bodies like Near Earth Objects (NEO) have become a common subject of study because of their importance in uncovering the mysteries of the formation, evolution and composition of the solar system. Among all asteroids, NEOs have stepped into prominence because of two important aspects: they are among the easiest celestial bodies to reach from Earth, in some cases, they can be reached with less demanding trajectories than a simple Earth-Moon trajectory and, even more meaningful, they may represent a threat to our planet.

It is hypothesized that every 26-30 million years a 10 km diameter asteroid strikes the Earth, while every 100 years there is a Tunguska class (100 m in diameter) asteroid impact. Each of these impacts permanently alters the characteristics of our planet to varying degrees. These events, and the risks they pose to our fragile ecosystem, have made the space community turn their attention to the issue of NEOs. Evidence of this new found interest is the prolific and successful asteroid exploration program of the last decade, with many completed missions such as NEAR, Deep Space 1, Deep Impact or Stardust, ongoing missions like Rosetta, Hayabusa and Dawn and future missions such as Don Quijote, which will not only study the target asteroid but also test the capability to deflect its course with a high velocity impact. In order to predict the effects of a deflection strategy, some studies have addressed the asteroid deviation problem either with an analytical approach [1, 2, 3, 4, 5] or by means of a numerical procedure based on a n-body model [6].

A few authors have performed a partial comparative assessment of the numerous proposed mitigation strategies [7]. Some of these emphasize a classification system based on NEO/spacecraft coupling, other systems are based on technology readiness and a third category on time to impact and/or intervention on the asteroid.

All these different techniques can be grouped into several families depending on the type of asteroid-spacecraft interaction:

- techniques producing an impulsive change in the linear momentum of the asteroid, such as kinetic impactors and nuclear interceptors,
- techniques actively producing a controlled continuous low-thrust, such as attached propulsion devices (e.g., electric/chemical engines, solar sails) or gravitational tugs

- techniques producing a passive low-thrust by an induced change of the thermo-optical properties of the asteroid surface, such as enhanced Yarkovsky effect or enhanced emissivity through white paint
- techniques producing a controlled thrust by the ablation of the asteroid surface (e.g., through laser beams or solar mirrors), or
- techniques producing a multi-impulsive change of the asteroid linear momentum by the ejection of surface material, such as the mass driver.

In 2006 the PI of this study performed, with a group of PhD students in Space Advanced Research Team (SpaceART*) of the University of Glasgow, a thorough comparison of a number of deflection methods proposed in the literature: nuclear explosion, low-thrust tug, gravity tractor, solar sublimation, kinetic impact, mass driver. Rather than using only one of the comparison criteria used by previous authors, the comparison was based on a multi-criteria approach. Miss distance at the Earth, warning time (time between launch and expected impact with the Earth), mass into space were simultaneously used to assess the optimality of a particular method. These three criteria (miss distance, warning time and mass into orbit) express quantitatively how easy deflecting an asteroid with a given method is and whether we can implement a given deviation strategy with present launch capabilities. The warning time, in particular, besides giving quantitative information on the time to react (how far in advance we need to know that an impact is going to occur), it gives an indication on the time available to repair a failed deflection operation. Furthermore, rather than using purely hypothetical scenarios or simple theoretical consideration, a wide range or real launch opportunity for each method over a period of 20 years were used to characterise the optimality of a particular method.

In order to take into account real mission opportunities and the three criteria at the same time, the concept of set dominance was introduced [8]: given a pair of deflection methods A and B, method A dominates method B if the number of mission opportunities of A that are dominating the mission opportunities of B is higher than the number of mission opportunity of B dominating the mission opportunities of A.

Where a mission (made of launch, transfer, interception and deviation) is dominant over another mission if all the three criteria are better.

In other words, a method was better than the other if there were more mission opportunities with a better value for all the three criteria. On top of this a TRL factor was applied to all the mission delaying the warning time to keep into account the required effort to bring the current technology readiness level to TRL 9.

This comparison approach required the development of a mathematical model for each of the deflection methods. Note that some methods were excluded from the comparison since the beginning because they require an excessively long warning time (for example, methods based on the Yarkovsky effect). Other methods instead were considered as the heavier counterpart of the ones included in the comparison (for example, surface ablation with a laser powered with a nuclear reactor is a heavier counterpart of solar sublimation).

The methodology used to model and compare the deflection methods has busted some myths. For example: kinetic impact methods are not always better

*http://www.aero.gla.ac.uk/Research/SpaceArt

than low-thrust tugs, though from a theoretical point of view it may appear so. In fact the direction of the impact is rarely optimal while the thrust direction of low-thrust tugs can be steered quite efficiently; or gravity tractors are not insensitive to the morphology of the asteroid because hovering at a distance require the knowledge of the mass distribution of the asteroid.

From the comparison the conclusion was that nuclear stand-off explosions were the most effective on the widest range of asteroids. The second best was solar sublimation with all the other methods order of magnitude less effective (according to the proposed comparison criteria).

Although nuclear explosions were the most effective, a subsequent study by SpaceART [9] demonstrated that for both nuclear explosions and kinetic impacts, the risk of a catastrophic fragmentation of the asteroid is not negligible. In particular, the total damage caused by an asteroid that was fragmented, as a consequence of a deflection attempt, was demonstrated to be greater than the expected damage caused by the unfragmented asteroid. The analysis showed that for deflection energy levels such that the nuclear explosion is significantly better than the other deflection methods a fragmentation is highly possible. For lower levels of energy the asteroids either does not fragment catastrophically or re-aggregate after fragmentation due to gravity forces.

Due to the possible catastrophic outcome of the nuclear option, the solar sublimation method appeared to be the most interesting deflection method.

In the following, we introduce an ablation-based technique called *Mirror Bees* and provide some results based on a preliminary feasibility study that supports this technique.

1.2 From solar sublimation to Mirror Bees

In 1992 Lunan et al. [10] and later in 1993, Melosh *et al.* [11, 12] proposed the use of a mirror (solar concentrator) to focus the solar energy onto a small portion of the surface of an asteroid. The resulting heat would sublimate the surface material creating a jet of gas and dust that would produce a continuous thrust. A conceptually similar idea is to use a laser beam, either powered by a nuclear reactor or solar arrays, to induce the required sublimation of the surface material. Melosh was comparing the solar concentrator idea against the nuclear blast option showing the advantage in using the collector. However, he was proposing the use of a substantially large structure in space, a primary mirror of 1 km to 10 km in diameter focusing the light of the Sun directly on the surface of the asteroid or onto a secondary mirror used to steer the beam.

In a more recent study, Kahle *et al.* [13] pointed out a number of technological limits of the solar collector idea proposed by Melosh. In particular:

- If the light of the Sun is directly focused on the surface of the asteroid, in order to have enough power density the mirror should be at relatively close distance from the asteroid. Kahle *et al.* were talking a distance of 1.25 km for a 630 m diameter mirror. As a consequence, the mirror should operate and manoeuvre under the effect of the irregular gravity field of the asteroid. Furthermore, at such a distance the contamination of the primary mirror, due to the ejected gasses, would be significantly fast. A longer distance would imply a larger mirror with a consequent increased difficulty in the control of the attitude.

- If a secondary steering mirror is used, the contamination of the primary can be reduced but the secondary would suffer the full contamination problem. Kahle *et al.* proposed some solutions to the contamination issue but all imply a significant increase in the complexity and mass of the system.
- The deployment and control of a large mirror represents a significant technological challenge and represents a single point failure for the entire mission.
- The total light pressure on the primary mirror would induce a significant force on the spacecraft requiring a constant orbit control.
- The high power collected by the primary would cause the secondary to operate at high temperature, in particular if the surface is contaminated and absorptivity increases with a reduction in reflectivity.

All these problems can be solved if the light is not focused directly on the surface of the asteroid and if instead of a single mirror, multiple mirrors are used. The idea is to use multiple mirrors of smaller dimensions and to superimpose all the beams of focused light onto the same spot. Furthermore, instead of focusing the light directly on the surface we propose the use of a series of collimating lenses for each primary mirror. The use of a collimating lens (or series of lenses) would allow the placement of the collector at a farther distance from the surface of the asteroid.

The main advantages of a multi-mirror system are:

- Each spacecraft is relatively small and more easily controllable.
- The solar pressure on each satellite is reduced and the total power on the secondary mirror is limited.
- The system is intrinsically redundant: each spacecraft does not represent a single point failure.
- The system is scalable: all the satellites are identical, therefore a larger asteroid would require simply more satellites without the need for a new design and development.

The challenge for a multi-mirror system is to superimpose all the beams and maintain pointing. Although the control of each individual satellite is easier, the coordination of multiple satellites represents a key issue that needs to be addressed to prove the actual feasibility of this concept.

Furthermore, the use of an adaptive optics to collimate the beam gives more flexibility for the placement of the mirrors but requires the development of the control of the optics. In particular, one of the issues that need to be addressed is the control of the optics, which includes the lenses and the shape of the mirror, especially since the primary mirror is to be deployed in space.

2 Conceptual Bee Design

The design of the device that is using the light of the Sun to sublimate the surface of the asteroid is a critical aspect of this deflection method. The device has to be able to concentrate a minimum power density at all times [14], therefore it is required to have the capability to steer the beam of light to hit any part of the asteroid and to control the concentration factor (or amount of light that is focused on a particular spot).

If we consider a direct projection of the light of the Sun onto the surface of the asteroid, the concentration ratio C_r of the system is the amplification of the power density at the input to the system and the output. If the only power provided to the system is the incoming solar radiation of the Sun, the concentration ratio is simply a ratio of the areas.

$$C_r = \frac{A_{\text{M}}}{A_{spot}} \tag{2.1}$$

where A is the total illuminated surface area of the mirror, M, that is *perpendicular* to the Sun, and illuminated spot on the asteroid surface.

In this section we illustrate several possible conceptual designs for the bees. For each design the light of the Sun is used in a different way, in particular the devise that is converting the incoming power of the Sun into an output power useful to sublimate the surface of the asteroid is substantially different. In general we can consider each bee made of three fundamental components:

- a power collecting unit
- a power conversion unit
- a power beaming unit

In the remainder of the report we will investigate in some detail only few of the conceptual designs presented in this section. However, the main open issues related to the implementation of the mirror bee concept are equally applicable to all the conceptual designs. Therefore, we will pick some representative examples useful to derive a general answer to the open questions on this deflection method.

Figure 2.1 shows a collection of 5 possible designs. This is not an exhaustive list but it identifies 5 basic concepts with substantially different technological implications. In particular, if we think of the three fundamental components of a bee, we can have:

1. Fixed mirror collector, with no power conversion and optical system to collimate and steer the beam. More specifically a system of lenses attempt a direct collimation of the light of the Sun and a secondary mirror steer the resulting beam.

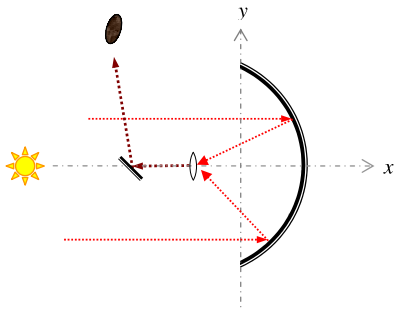

(a) Parabolic reflector with collimating lens, and steering mirror.

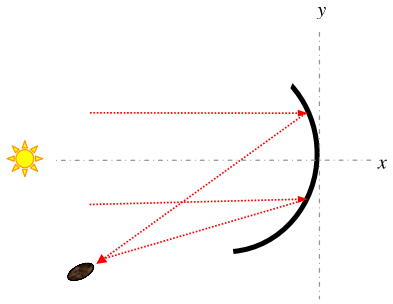

(b) Direct imaging using an adjustable reflector.

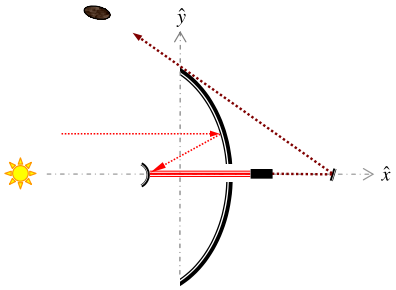

(c) Dual reflector system with a solar-fed laser followed by a steering mirror.

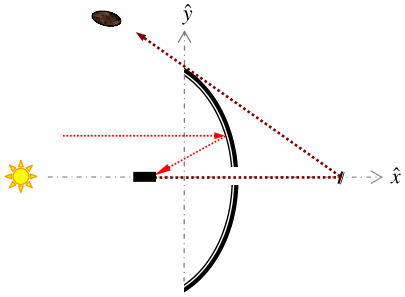

(d) Single reflector with solar-pumped laser and rear directional mirror.

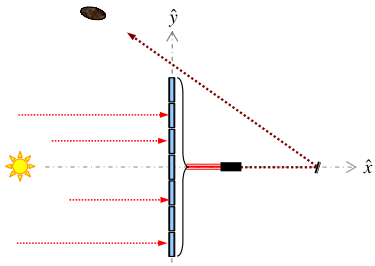

(e) Solar array for an indirect pumped laser system.

Figure 2.1: Possible configurations for the mirror assembly.

2. Adaptive collector, with no power conversion and direct imaging on the surface of the asteroid. In terms of components this is the simplest concept. The whole complexity is in the design of the collector. Note that, unlike the original concept of Melosh there is not steering secondary mirror. The steering is provided by the adaptation of the shape of the mirror,

although, as it will be explain later on in this report, this particular design will work together with a particular orbit design.

3. Dual fixed reflectors as collecting device, a laser (directly pumped or indirectly pumped) as power conversion and a secondary steering mirror as beam control system. In this case both the laser and the secondary mirror are in the shadow cone of the primary mirror.

4. Fixed mirror collector, a laser (directly pumped or indirectly pumped) as power conversion and a secondary steering mirror as beam control system. In this case the laser is in between the primary collector and the Sun while the steering mirror is in the shadow cone of the primary mirror.

5. Large solar array as solar collector, a laser (indirectly pumped) as power conversion and a secondary steering mirror as beam control system. In this case both the laser and the secondary mirror are in the shadow cone of the primary mirror.

In this report we will investigate the dynamical aspects related to options (a) to (d) and in the last section we will give a first estimation of the system budget for all five options.

2.1 Adaptive mirror configuration

The single mirror configuration is composed of an asymmetric adaptive primary mirror. The shape of the primary mirror is assumed to be adaptable such that the focal point can be moved in order to steer the beam in the desired direction.

If the mirror was flat we could define a local Cartesian reference frame with coordinated axes $\mathcal{M}[x_{\text{M}}, y_{\text{M}}, z_{\text{M}}]$ centered in the barycenter of the mirror assembly and with the x_{M} perpendicular to the mirror surface (see Fig. 2.2). Now, we can define the shape of a curved mirror in the same reference frame. Given the position of the focal point in $\mathcal{M}$, the position of the center of a mirror element with infinitesimal area dA_{M} and assuming a perfect reflection, the law of reflection gives us,

$$\frac{dx_{\text{M}}}{dy_{\text{M}}} = \tan\left(\beta - \tfrac{\pi}{2} - \phi\left(x_{\text{M}}, y_{\text{M}}, x_f, y_f, \beta\right)\right) \tag{2.2}$$

where $[y_f, x_f]$ is the position of the focal point, β is the Sun aspect angle with respect to the reference frame $\mathcal{M}$ of the mirror assembly and ϕ is the reflection angle. In Fig. 2.2, the angle β would be angle between the Sun direction and the y_{M} axis. Note that, if we consider the solar rays parallel to the Sun-Asteroid direction the angle β also represents the attitude angle of the mirror reference frame with respect to the Hill reference frame centred in the asteroid and therefore it will be referred to as the attitude angle of the mirror in the following.

By integrating (2.2) with initial conditions y_{M_0} and x_{M_0}, we can get the position and attitude of each section of the mirror in the y_{M}-x_{M} plane given the position of the focal point and the direction of the incoming Sun rays. The mirror is then considered to be symmetric with respect to the y_{M}-x_{M} plane such that each section of the mirror parallel to the y_{M}-z_{M} plane is a parabola.

In this study we coded (2.2) into a Matlab® function and incorporate that into the orbital dynamic model so that for each position of the mirror with respect to the asteroid (the focal point) and every attitude angle we get a different mirror. An example is represented in Fig. 2.3.

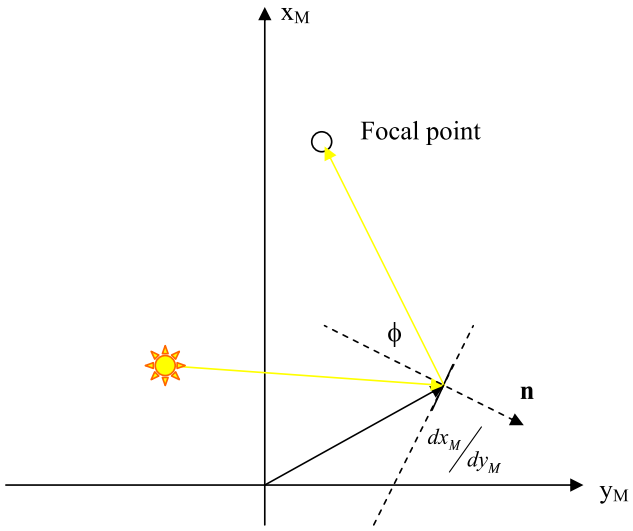

Figure 2.2: Schematic of the mirror reference frame.

2.2 Fixed mirror configuration

The fixed mirror configuration consists of a parabolic reflector which concentrates the reflected sunlight. This beam is then directed onto the desired spot on the surface by means of a flat directional mirror. The primary parabolic mirror is held normal to the Sun to maximize the illuminated surface area, and hence power density on the surface.

As the primary reflector is symmetrical around the z-axis (i.e. the aperture is a circle), the total surface area is calculated based on the focal length f_ℓ accounting for the blockage caused by the directional mirror,

$$A_{\text{M1}} = \int_{\frac{d_g}{2}}^{\frac{d_{\text{M1}}}{2}} \int 4\sqrt{\left(\frac{x}{2f_\ell}\right)^2 + \left(\frac{y}{2f_\ell}\right)^2 + 1}\; dx\, dy \tag{2.3}$$

where d_{M1} is the diameter of the aperture on the parabolic mirror, d_g is the diameter of the gap (equal to the entrance aperture of the laser assembly).

Several options exist for directing the beam onto the surface of the asteroid, as seen in Fig. 2.1. One option is to use a lens system to collimate the beam, while another uses a laser as the collimator. Each system has advantages, and disadvantages depending on the mission type, as will be seen later in this report.

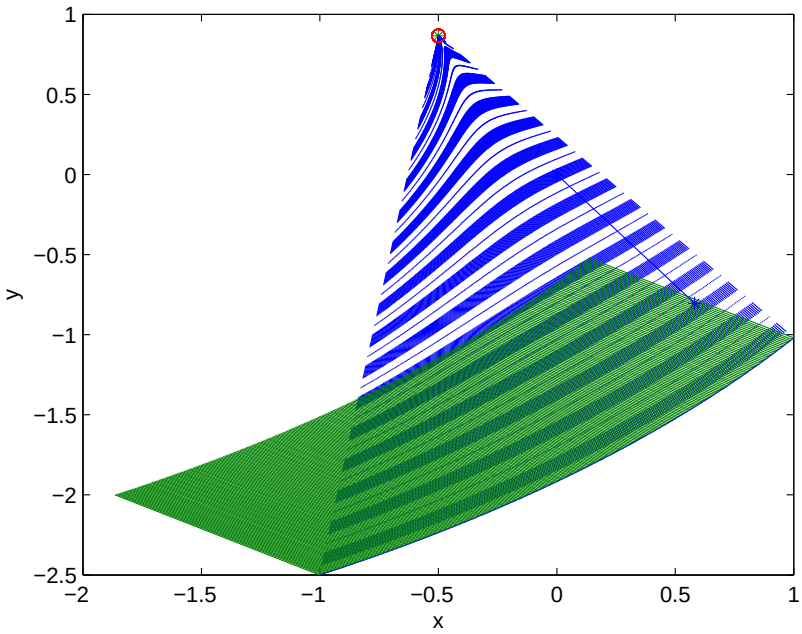

Figure 2.3: Example of a single mirror projecting the light of Sun onto the focal point. Green lines are the Sun rays, blue lines are the reflected rays. The mirror is represented in the x_{M}-y_{M} mirror reference frame: in this reference frame the Sun is at 155° and the focal point at 125°. Axes are reported in normalised units.

3 Focusing and Beaming Systems

3.1 Introduction

This section will describe different options for collecting the light of the Sun and projecting it onto the surface of the asteroid with the required power density.

We will distinguish between the focusing device (or collector) and the beam generation devise. For all the options the focusing devise will be a mirror. The shape of mirror will depend on the strategy used to beam the light onto the surface of the asteroid.

The various options proposed in this study differs for the way collected power of the Sun is projected onto the surface of the asteroid. In particular we will look into three different concepts:

- direct imaging
- indirect imaging through an optical system (collimating lenses)
- laser

Prior to the presentation of the three concepts, this chapter will introduce some basic properties of the Sun and the radiation produced.

3.2 Solar properties

The physical angular measurement of the Sun (or *solar disk*) can be calculated by simple geometry. Given a volumetric mean radius of the Sun of 6.9600E5 km, for the current orbit of Apophis the Sun has an conic half-angle of 6.2349 mrad at the NEO periapsis (0.7461 AU), and 4.2348 mrad at the NEO apoapsis (1.0986 AU).

Figure 3.1 shows the extra-terrestrial solar spectral irradiance for a range of wavelengths (assuming a black body temperature of 5777 K). The database used is the ASTM E-490-000*, published by the American Society for Testing and Materials (ASTM) in 2000 based on data from satellites, space shuttle missions, high-altitude aircraft, rocket soundings, ground-based solar telescopes, and modeled spectral irradiance. The wavelength of visible light falls between violet (380–450 nm) and red (620–750 nm), with the peak irradiance occurring at 450.5 nm (2.2198 MHz).

*www.astm.org/Standards/E490.htm

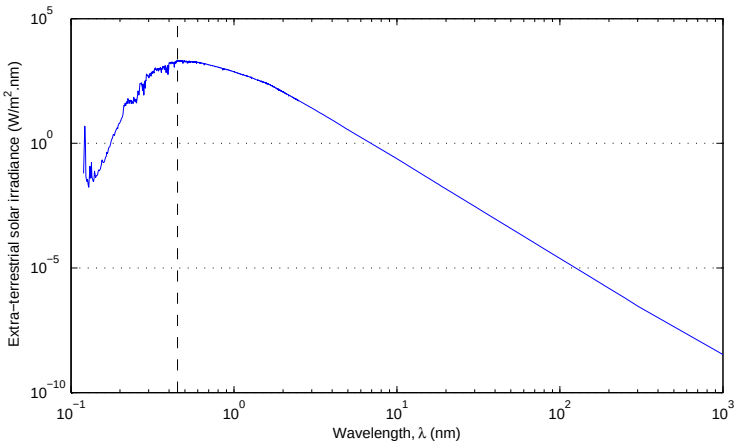

(a) Full spectrum.

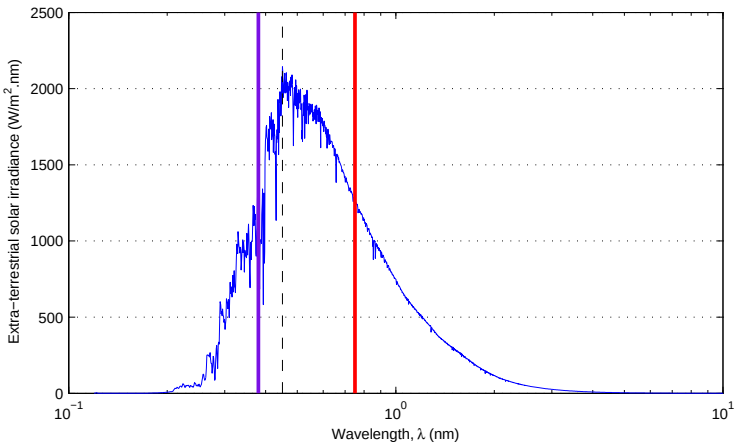

(b) Close-up, showing visible spectrum.

Figure 3.1: 2000a (2006) ASTM Standard Extraterrestrial Spectrum Reference E-490-00. Note, the integrated spectral irradiance has been made to conform to a solar constant of 1366.1 W/m^2.[15]

The solar flux constant, S_0, is defined as the rate at which energy is received from the Sun over a unit area normal to the radiation of the Sun, taken at a mean distance of one astronomical unit. The World Radiation Centre adopted of a mean solar flux value of 1367 W/m^2, with an uncertainty of 1%, which is the one most commonly found in literature. However, as seen from Figure 3.2 which shows the measurements of the solar flux over a period of 25 years, that value may overestimate the amount of energy flux provided.

In the following, the solar flux is assumed to be 1367 W/m^2 and varies quadratically with the distance from the Sun, $S(r) \propto r^{-2}$.

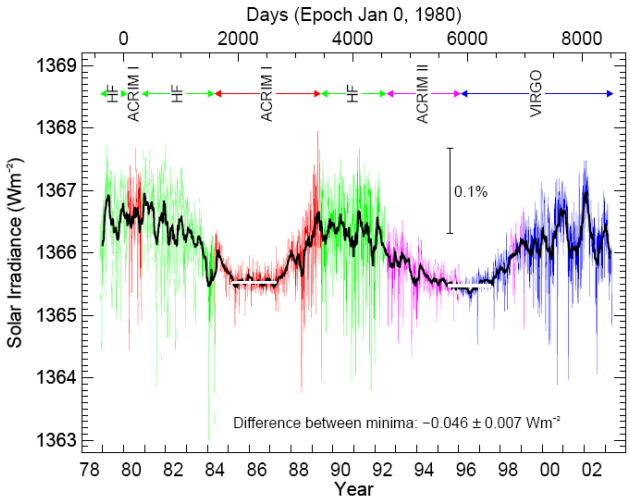

Figure 3.2: Composite of total solar irradiance measured by different space-based radiometers (HF on NIMBUS7, ACRIM-I on SMM, ACRIM-II on UARS, VIRGO on SOHO). The coloured lines show daily averaged values, and the black line is mean (source image from [16]).

3.3 Direct imaging

The simplest design for the mirror assembly is to directly focus the sunlight onto the asteroid, essentially imaging the solar disk onto the asteroid surface. There are a number of restrictions however, given the coupled nature of the variables. The range is determined by the focal point of the mirror. Coupled with a manufacturing limit on maximum size of the mirror, this forces the spacecraft to operate in close proximity to the surface of the asteroid, subjecting it to the largely unknown, and inhomogeneous gravity field of the NEO.

The beam must also be directed towards the asteroid, since the asteroid, Sun and spacecraft are not inline as they would be in a typical imaging system. This means that either the mirror must operate on an angle, translating into a loss of illuminated surface area, or the focal point must be raised or lower relative to the principal optical axis.

Lastly, the spot size is determined by the concentration ratio (magnification) which is a function of the ratio of the distance between the source and the mirror ($r_{\odot/sc}$), and the distance between the mirror and the image ($r_{sc/A}$).

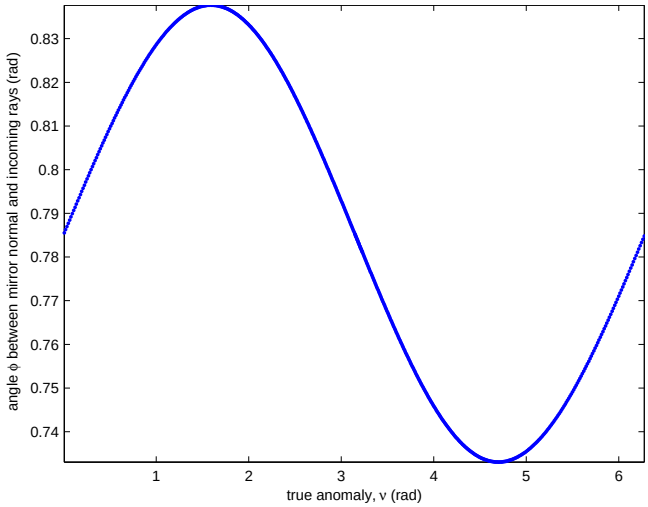

Figure 3.3: Angle of reflection ϕ, between mirror surface normal and incoming (or outgoing) rays.

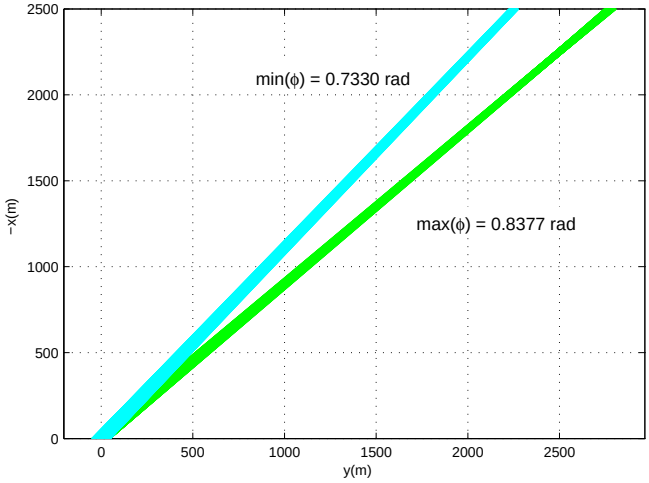

Figure 3.4: Direct imaging of solar disk on Apophis using a fixed paraboloidal reflector.

Given the equation for a x-y symmetrical parabolic reflector,

$$(z - z_0) = \frac{(x - x_0)^2}{4f_\ell} + \frac{(y - y_0)^2}{4f_\ell} \tag{3.1}$$

where f_ℓ is the focal length. The angle between the Sun and one of the spacecraft in the formation is shown in Fig. 3.3; on average, the half-angle ϕ fluctuates between 0.7–0.9 rads. If a parabolic mirror with a 100 m aperture diameter is rotated through the same angular range, the result is shown in Fig. 3.4. The Sun assumed to be along the x direction and Apophis is moving in the positive y direction (see Section 4 for more details on the reference frames used in this study). The spot size at a nominal range of 2.5 km fluctuates between 53 m (at $\min(\phi)$) to 66 m (at $\max(\phi)$). The focal length, for a minimum image size at the nominal range, was set to 5 km. This gives a minimum concentration ratio of 2.5. For the sake of analysis, if we let $\phi = 0$ rad, and place the focal length exactly at the asteroid ($f_\ell \Rightarrow 2.5$ km), then the spot diameter due solely to the effect of the solar disk is 25 m (for a concentration ratio of 20).

The loss due to angle of reflection can be reduced by instead moving the focal point of the mirror by continually altering the shape of the reflector. This maximizes the illuminated area, which allows for a greater concentration ratio. Details on the design of the adaptable reflector shape are given in Section 2.1. Figure 3.5 shows the result of directly focusing of the true Sun disk on an 80 m aperture diameter reflector at a range of 780 m from the NEO. The spot diameter on the surface is 8.2 m, which would correspond to a concentration of about 95. The image was obtained with a simple ray tracing code that was developed within this study contract.

In the work of Sanchez et al. [8], a value of 2500 was used to perform a comparison of the solar sublimation approach against other deflection methods. If 2500 is used as a reference, then 26 satellites with a diameter of 80 meters superimposing their beams would be required to have enough power density on the surface of the asteroid. Note that 2500 is not the minimum concentration ratio required to sublimate the surface of a NEO with a single spacecraft. In Section 7 we will expand on this showing the minimum number of satellites required to deflect Apophis. The number and size of satellites depends on the available time for the deflection action and on the distance from the asteroid. The distance from the asteroid, on the other hand, depends on the available locations in the proximity of the asteroids that would allow the spacecraft to see the Sun and to avoid any plume impingement.

A study commissioned by NASA [17] in the late 1980s investigated concepts for large solar collectors, including an analysis of the effects of errors on the effective concentration ratio of space-borne paraboloidal reflectors. Starting with a perfect paraboloidal reflector with aperture diameter D, see Fig. 3.6a, and assuming the same solar disk angle of $2\epsilon_S \approx 9$ mrad, the resulting image is shown on a receiver plane located just after the focal point $f_\ell = F$, shown in Fig. 3.6b.

The dimensions of the image are [17],

$$u = 2\rho\epsilon_S \tag{3.2}$$

$$v = \frac{2\rho\epsilon_S}{\cos\theta} \tag{3.3}$$

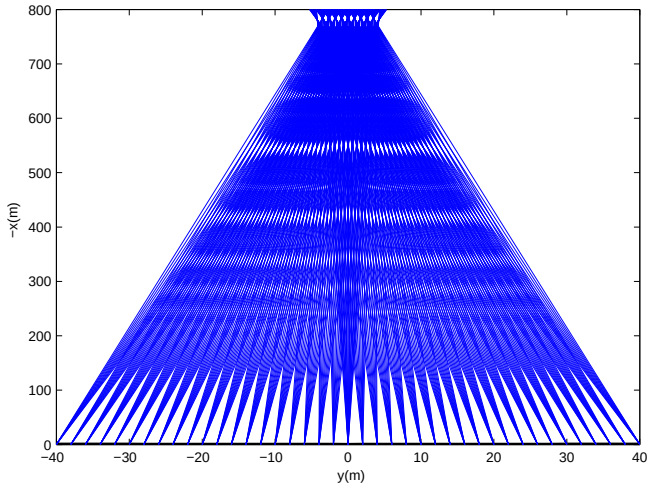

Figure 3.5: Direct imaging of solar disk on Apophis using an adaptive paraboloidal reflector.

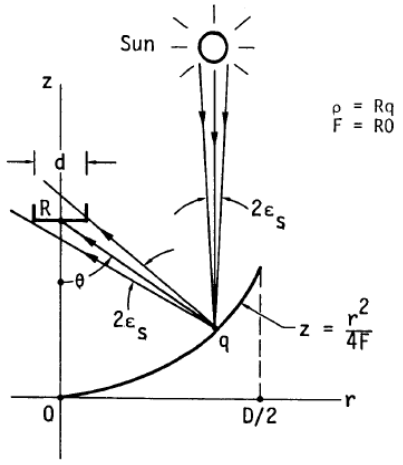

(a) Geometry of a continuous paraboloid reflector.

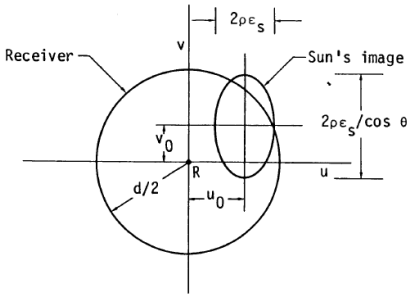

(b) Intersection of the Sun's image and the receiver disk in the receiver plane.

Figure 3.6: Analysis of the image of Sun (source images from [17]); $[u_0, v_0]$ represent an offset due to geometric errors on the reflector surface at the point of reflection q.

where ρ is the distance from the point on the reflector (q) and the focal point. The equations for the image are not accounting for any geometric errors on the structure of the reflector. The effect of any errors would be an offset in the intersection with the focal plane, altering the centre point of the elliptical image (given as $[u_0, v_0]$ in Fig. 3.6b).

As a first approximation we can consider that as the radius of the projected image grows linearly with the distance between the mirror and the target, the

area of the collector, for a fixed concentration ratio, grows quadratically with the distance from the target.

On the other hand it is worth to underline that as the mirror moves away from the Sun the concentration ratio can be increased, at constant distance from the target, by keeping the size of the mirror constant and changing its curvature. Conversely, when the mirror moves toward the Sun the concentration ratio for a fixed distance and fixed size has to go down. The interesting thing is that the solar flux increase quadratically as the mirror approaches the Sun, thus compensating for the loss in concentration factor. This is also true when the mirror moves away from the Sun, therefore by changing the curvature of the mirror the total flux on the target area can be maintained constant as the mirror moves with respect to the Sun.

3.4 Collimating lens

One option investigated to improve the concentration ratio was to considerably reduce the focal length to the same magnitude of the diameter, and add a lens system which minimizes the divergence of the beam after the focal point of the mirror. An in-house ray tracing program was developed (in Matlab) in order to design lens systems based on an objective function. An education-version of the optical software program OSLO[†] was also used to analyse the lens designs, however it was found that the Matlab code was more efficient for this analysis (due to limitations in the educational version of the software, learning curve, etc.). OSLO-EDU does feature a number of lens designs in their standard library; among them are a lens design for a collimating laser communication system (see Fig. 3.7) and the lens system used in the Hubble telescope (see Fig. 3.8). Using these existing design as a basis, single and dual-lens systems were modeled.

A single spherical lens will always be subject to, among other errors, spherical abberations leading to a distortion in the intersection of the beams (i.e. they do not all meet at a single point, but instead create a 'curved envelope' about the original focal point), or going in the other direction, the 'collimated' beams instead diverge.

A common class of lens exist that attempt to minimise both spherical aberrations, and chromatic aberrations that result from using multiple wavelengths (or frequencies) of incoming rays. The two aberrations have a similar corrective approach in that the solution attempts to bring distorted refractive/reflective rays into focus on the same plane. The distortion can be due either to the effects of different frequencies through the lens medium, or by distance from the optical axis and corresponding angle of incidence. The design for an *achromatic lens* (or achromat) uses two lenses cemented together to form a doublet. The first lens generally has a higher index of refraction, while the second has a lower index such that the aberration of one is counteracted by the second.

In this case, an optimisation was run to determine a lens sytems that would collimate the output from a fixed parabolic mirror. The maximum number of lens surfaces was set to 5 (each lens having two surfaces), with the free variables set to the radius of curvature of each surface (assumed to be spherical), and the distance along the optical axis from the previous lens surface to the

[†] `http://www.sinopt.com/`

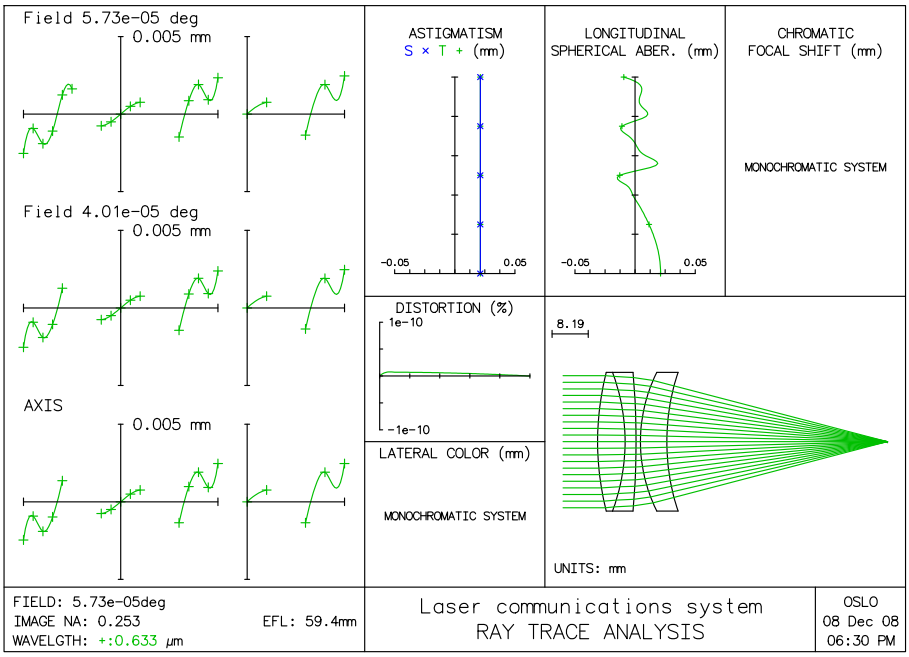

Figure 3.7: Laser communication system: Ray trace analysis (produced by OSLO-EDU).

current surface. Figure 3.9 shows the resulting optimised system of lenses assuming parallel incoming rays from the Sun. The maximum angular divergence is 5.7923E-5 rads, resulting in a spot diameter of 1.6574 m (using a reflector with an aperture diameter of 40 m and a focal length of 60 m). Table 3.1 gives the specific solution vector for the lens system.

However, when the incoming solar rays were modified to account for the size of the solar disk, the results were infeasible. As seen from Fig. 3.10, for the same reflector-lens configuration as above, the divergence results in a spot diameter of just over 900 m. Even when the lens system was re-optimised to account for the off-axis incoming rays, the results of the spot size are still larger than the baseline case with no lenses.

Table 3.1: Dimensions of lens assembly given in Figure 3.9.

	Surface	Radius of curvature (m)	Distance from focal point (m)	Index of refraction*, n
Reflector:	0	$z = \frac{R^2}{4f_\ell} - f_\ell$	-60	1.0
First lens:	1	5.06239	5.220826	1.689
	2	3.4792	1.10455	1.0
Second lens:	3	-18.0540	1.332166	1.673
	4	-3.399048	0.310507	1.564
	5	5.46774	0.615707	1.0

*The index of refraction listed is for the material from surface i to $(i+1)$.

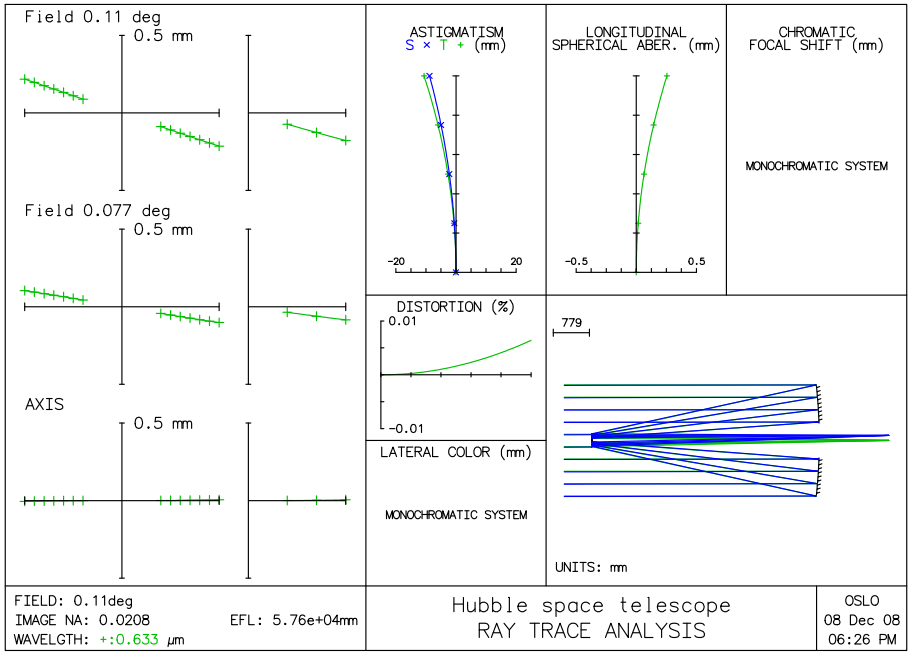

Figure 3.8: Hubble space telescope: Ray trace analysis (produced by OSLO-EDU).

If the lens system worked with very little distortion, the other concern would be due to the monochromatic nature of glass lenses versus mirrors, which are frequency-independent. Superachromatic lens can focus up to four wavelengths bracketing the visible spectrum, which contains the highest energy segment of the solar spectrum, however the system would still have to account for a loss of power density due to the frequency limitation. Other, more complex options include a gradiation of the index of refraction of the material, or using slotted or notched lenses (similar to concept to Fresnel lens, for example). However these would have to specifically manufactured for a fixed set of angles; given the variance in the angle of incidence/reflection this poses numerous difficulties in the design. It is possible to fix the angle of incidence, and instead remove the constraint of the primary mirror remaining inline with the Sun-pointing vector however at a cost of a decrease in available solar power (due to the shadows introduced onto the reflector surface).

3.5 Solar-pumped laser

The concept of converting emitted radiation from the Sun, a broad-band renewable energy source, into a narrow, coherent beam is decades old [18]. The barrier has been making the process efficient given the broad frequency band of the Sun' radiation, compared with the narrow absorption bands of most lasing crystals.

Lasers work on the premise of exciting electrons by the stimulating them with the addition of photons (or quantum energy), which temporarily boost

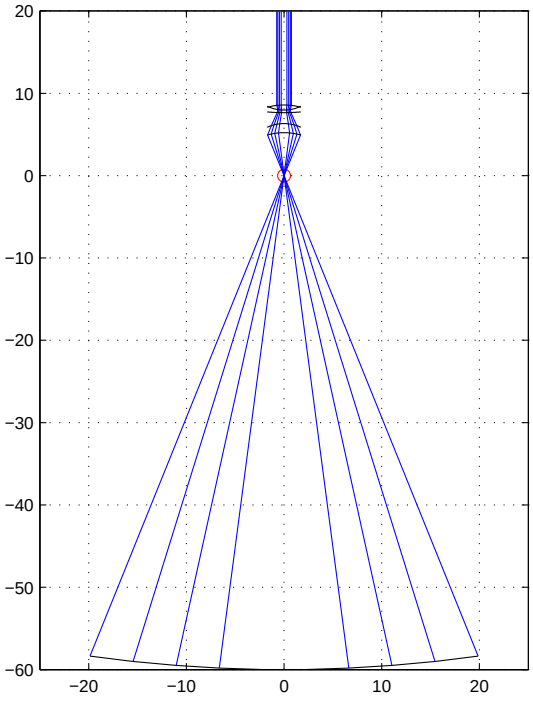

(a)

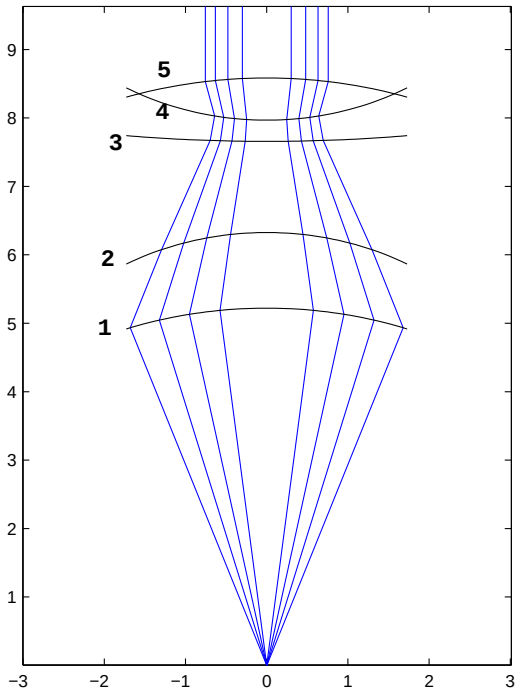

(b)

Figure 3.9: Lens configuration for collimating a beam assuming parallel incoming solar rays. The axes are in metres, with the focal point of the reflector at (0,0).

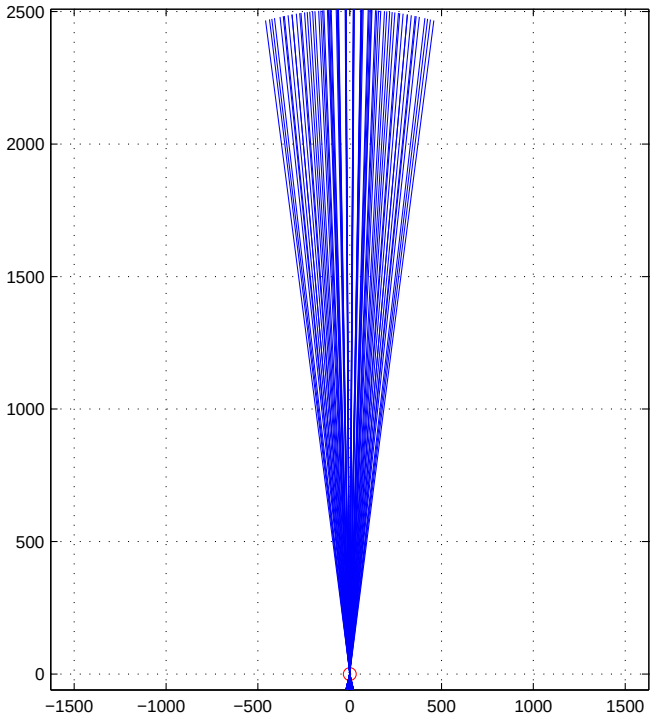

(a)

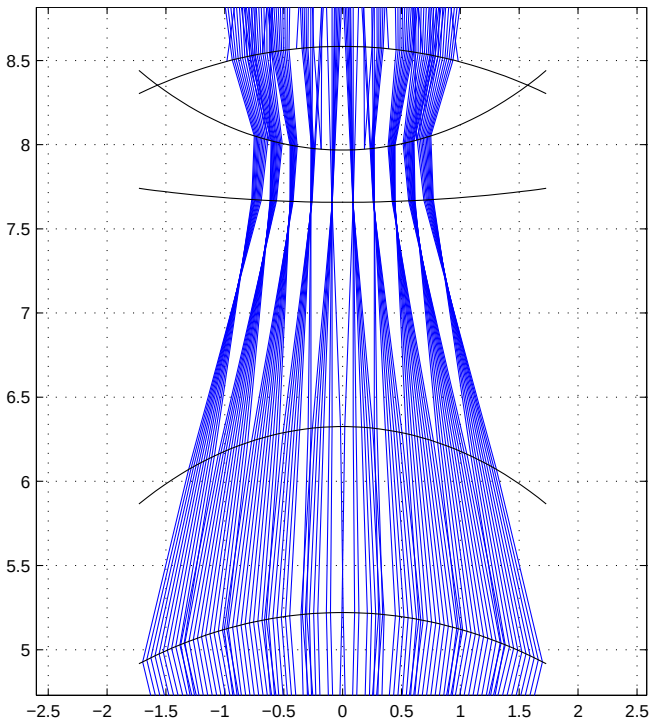

(b)

Figure 3.10: Effect of off-axis rays (accounting for the solar disk) on the lens system in Fig. 3.9. The axes are in metres, with the focal point of the reflector at (0,0).

them up to a higher energy state. This simulation continues until a popular inversion exists, where there are more electrons at a higher energy state, e.g. E_1 than at the lower (or original) state, e.g. E_0. The release of photons when the electrons drop back to their original base state produce an emission that has the same spectral properties of the stimulating radiation, and is therefore highly coherent. There are can be any number of energy state levels and transitions, for e.g. an Nd:YAG laser has four states. The energy that is not released as part of the output emission, is instead released as heat. This means that the laser much be continually cooled, which in space means large radiators.

There are two general methods of powering the laser: *direct pumping*, where the energy is directly used to excite the laser, and *indirect pumping*, where an intermediate step is used to first convert the energy, e.g. solar radiation, into electricity.

3.5.1 Indirect pumping

Indirect solar-pumped lasers convert the solar energy first into electricity, which is then used to power the laser. Photovoltaic cells are an obvious choice for space applications. The drawback, of course, is the addition of an electrical power generator meaning added mass, size and power requirements. An example of indirect pumping concept taken from [19] is represented in Fig. 3.11. The picture represents a solar dynamic system with a primary solar collector and a laser in the shadow cone of the collector.

A possible solution is to use high efficiency solar arrays in conjunction with a solid state laser. Solid state lasers pumped with electric power can currently reach 60% efficiency. If we assume a 30% efficiency for the solar arrays we can have an overall 18% efficiency. If a pumped laser is used, then the focal point can be close to the primary mirror and a high concentration factor can be obtained with a relatively small mirror. For example, if the mirror has an area of 314 m^2 (equivalent to a 10 m circular mirror), then the collected power at 1 AU is 429.5 kW. The solar array + laser system converts only 18% of this power, therefore only 77.3 kW are beamed to the surface of the asteroid, the rest needs to be dissipated.

We can assume to have a radiator in the shadow cone of the primary mirror and dissipating the excess power. In steady state conditions, given a radiator of surface area A_{R}, the temperature of the radiator would be:

$$Q_{radiator} = \sigma \eta_R A_R T_R^4 = P_{sun} - P_{out} - P_{reflected} \tag{3.4}$$

$$T_{\mathrm{R}} = \left(\frac{\alpha_{\mathrm{SA}} S_r A_{\mathrm{M}} - \eta_{\mathrm{SA}} S_r A_{\mathrm{M}} - \sigma \epsilon_{\mathrm{SA}} T_{\mathrm{SA}}^4}{\sigma \epsilon_{\mathrm{R}} A_{\mathrm{R}}} \right)^{\frac{1}{4}} \tag{3.5}$$

where $\alpha_{\mathrm{SA}} = 0.8$ is the absorptivity of the solar converter, S_r is the solar flux at distance $r_{\odot/sc}$ defined in (4.13), A_{M} is the area of a 20 m diameter mirror, η_{SA} is the efficiency of the solar converter, σ is the Stefen-Boltzmann constant, $T_{sa} = 200°\mathrm{C}$ is the operating temperature of the solar converter and lastly $\epsilon_{\mathrm{SA}} = 0.7$, $\epsilon_{\mathrm{R}} = 0.9$ are the emissivity of, respectively, the solar array and the radiator. The solar array was assumed to have a surface area of 1 m^2. Figure 3.12 shows the resulting radiator temperature versus surface area for different efficiencies η_{SA} of the solar array + laser system.

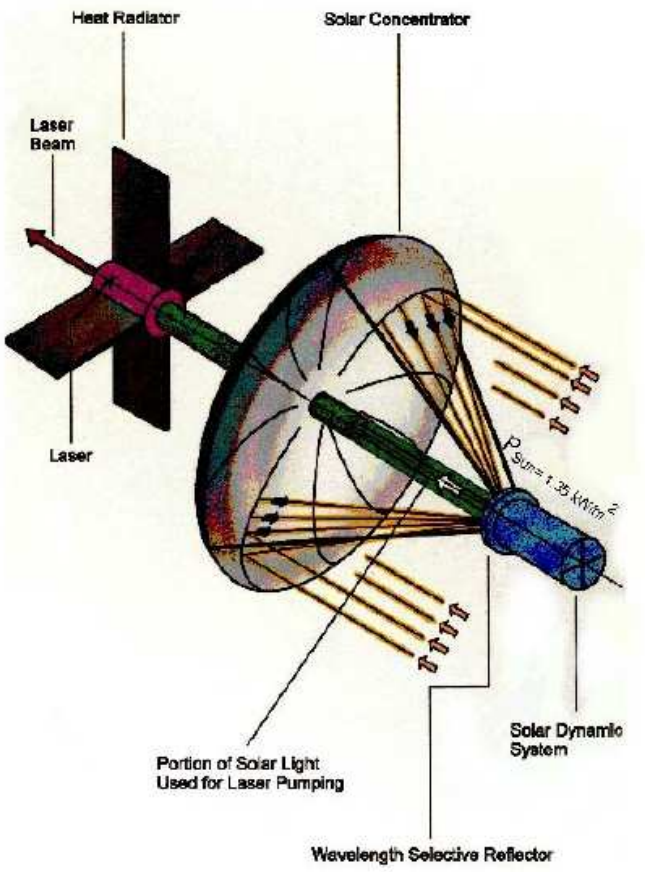

Figure 3.11: Example of a solar laser system (source image from [19]).

The system would need to operate at a temperature higher than the one of the radiator imposing severe conditions on the solar arrays. Therefore, we envisage the following possibilities:

- the heat is dissipated through a large radiator, located in the shadow cone of the primary mirror,
- the efficiency of the solar arrays is substantially increased above 30%,
- the operating temperature of the solar arrays is increased above 200°C.

An alternative could be to use a solar dynamic system with a Stirling engine [20, 21] (or Bryton cycle or Rankine cycle) instead of the solar arrays. This solution would achieve a conversion efficiency of up to 38% and, more importantly, it could operate at higher temperatures (up to 850°C). However, although the scalability of the system has to be considered with care, according to the current status of the research at NASA on Bryton converters [22], and we consider only the mass of the receiver, Bryton engine, heat rejection and associates structure, the power conversion unit can have a specific output power of 27 W/kg. This estimation is based on the advanced technology that NASA was expecting in

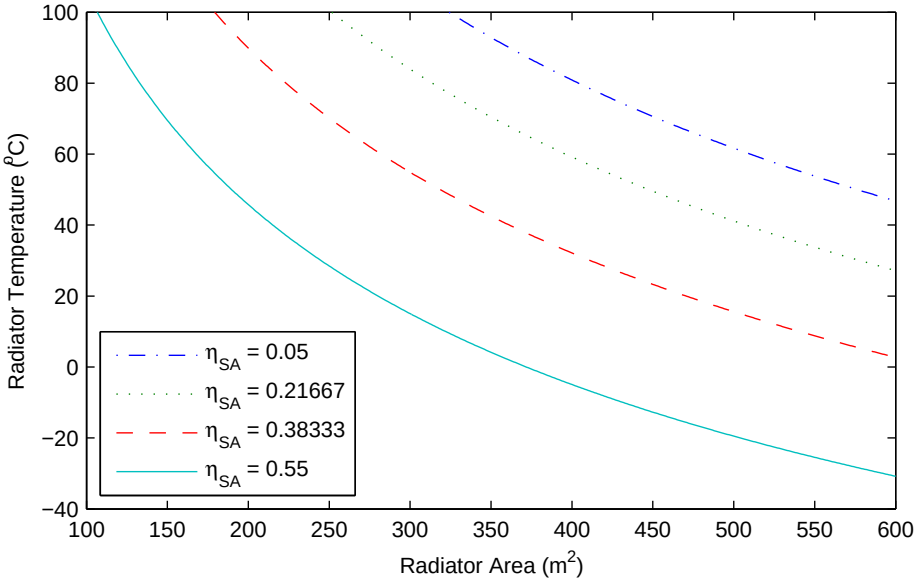

Figure 3.12: Radiator area vs. radiator temperature

1999. Thus, for the example reported above, the mass of the conversion unit would be about 5 MT (for an efficiency of 34%). This mass is still unsatisfactory for a 10 m radius bee. The main problem is to make the receiver and the heat rejection far lighter than what they are at present.

In Section 7 of this report we will provide some estimations of the mass budgets for each of the conceptual designs in Section 2.

3.5.2 Direct pumping

Direct solar-pumped lasers, do precisely what the name suggests: the laser is directly energized using solar radiation. Due to the mismatch between the wide-band emissions of the Sun with the narrow absorption bands of lasers, the loss of available solar power is currently rather high.

3.5.2.1 Lasing Material

In theory, any lasing material that can be optically pumped can also be used as a solar laser. It is not the intent of this report to delve too deeply into the technical details of lasing materials, however a selection of solid-state laser materials are summarized below based on current literature [23, 24, 25].

The Nd:YAG, composed of neodymium ions (Nd^{3+}) in yttrium aluminum garnet ($Y_2Al_5O_{12}$), is the most commonly used in solid-state laser for many cross-platform applications since it is relatively cheap to produce and readily available, and more importantly, has good thermal resistance, durability and lifetime. The absorption bands are relatively narrow however, and with the main peak at 1064 nm (see Fig. 3.13). The overlap between the Nd:YAG absorption spectrum, and the solar radiation spectrum is around 0.14 [24].

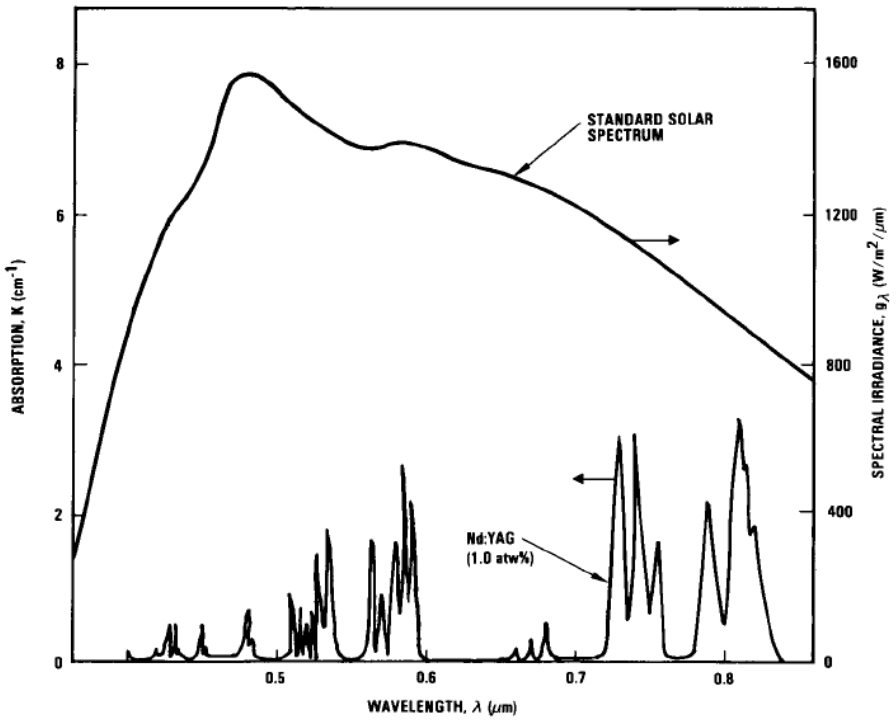

Figure 3.13: Nd:YAG absorption bands compared with the standard extraterrestrial solar spectrum (source image from [24]).

Chromium doping, Cr:Nd:YAG can further improve the power conversion over the undoped, conventional Nd:YAG systems.

Other types of lasers include [23]:

Nd:Cr:GSGG has received considerable attention because of the good spectral match between the flashlamp emission and absorption of the Cr ions. The host of this laser is the Gadolinium Scandium Gallium Garnet (GSGG). An efficient energy transfer between the Cr and Nd ions results in a highly efficient Nd:laser.

Nd:YLF is a good candidate for certain specialized applications, because the output is polarized, and the crystal exhibits lower thermal bi-refringence. Nd:YLF has a higher energy storage capability (due to its lower gain coefficient) compared to Nd:YAG and its output wavelength matches that of phosphate Nd:glass. Therefore modelocked and Q-switched Nd:YLF lasers have become the standard oscillators for large glass lasers employed in fusion research. The host YLF is the uniaxial crystal Yttrium Lithium Fluoride ($YLiF_4$).

Nd:YVO_4 The laser emission cross-sections of Nd:YVO_4 crystal at 1060 nm and 1340 nm are 2.7 and 18 times larger than that in Nd:YAG respectively, and the crystal has good mechanical, physical and chemical properties.

In a paper presented in 1994, Geoffrey Landis of NASA was discussing the use of directly solar pumped laser based on semiconductor technology [26]. As

Landis pointed out, the expected efficiency of directly pumped semiconductor laser would depend on the same efficiency losses of a solar cell, therefore Landis was expecting a lasing efficiency (output/input power ratio) of 35%. Such an efficiency would be order of magnitude higher than the best YAG system, which was expected to reach 6% of overall efficiency.

Direct solar pumping would represent an interesting solution in terms of complexity of the overall system. In fact no cooling system for the photovoltaic conversion and no power transmission would be required. On the other hand the TRL of both solar cells and semiconductor lasers is far higher than the one of a directly pumped laser and an indirectly pumped laser can be expected to be operational very soon.

Furthermore, recent semiconductor laser, electrically pumped, have proven over 73% plug efficiency [27]. A substantial increase in cells efficiency has also to be expected. In particular, in order to achieve a 35% efficiency in direct pumping, semiconductor technology should allow the absorbtion of the solar spectrum over a wide range of frequencies. A high efficiency of a directly pumped laser is therefore expected to correspond to a high efficiency of solar cells. An increase of solar cell technology up to 50% [28] is reasonable which would make an indirect pumping system of comparable efficiency to a 35% direct pumping system.

3.6 Discussion

From the analysis of the methods for collimation of the solar light we can argue that collimating the solar light at long distances is not possible with conventional optics. Though a more thorough investigation would be needed to conclude that this technological solution is not feasible we can say that the other solutions analyzed in this chapter appear more promising.

In particular it is worth underlining that the direct imaging option appear feasible. As we will see in Section 4 a proper placement and control of the mirror in proximity of the asteroid is also possible. Therefore the direct imaging option with adaptive control of the focal point is a viable solution for this deflection method. The advantage of a direct imaging system stands in its reduced number of components and the virtual zero dependence on the frequency of the light beamed on the surface of the asteroid. In other words if the surface material has, for example, an average absorptivity of 0.7 over the visible spectrum we can say that the surface material is absorbing 70% of the incoming radiation. This is not true for the monochromatic beam generated by a laser since we should be sure that the surface material has a maximum absorption at the frequency of the laser beam. The main disadvantage of a direct imaging system is that it is strongly dependent on the distance from the asteroid. In fact, as we have seen in this chapter, for a constant concentration ratio the size of the mirror grows fast with the distance from the asteroid.

The laser option has the fundamental advantage to be far less dependent on the distance from the asteroid. Therefore it allows for a more flexible beaming of the light onto the surface of the asteroid. On the other hand the number of components in the system is higher. The choice between a directly pumped system versus an indirectly pumped one is not conclusive. At this particular stage of the research in laser technology and solar cell technology the most

short term solution with acceptable efficiency would be the indirect pumping. On the other hand, a 35% direct pumping laser would significantly reduce the complexity of the system. Last but not least the laser option would require a minimum knowledge of absorption frequency of the surface material of the asteroid.

The impact on the number of satellites required to achieve a given deflection can be seen in Fig. 3.14 where the concentration ration used in Sanchez *et al.* [8] is taken as a reference for the required power density on the surface of the asteroid. The two figures represent for two different efficiencies of the laser system (laser+solar arrays in the case of the indirect pumping) the number of satellites as a function of the surface area on the collector for each satellite.

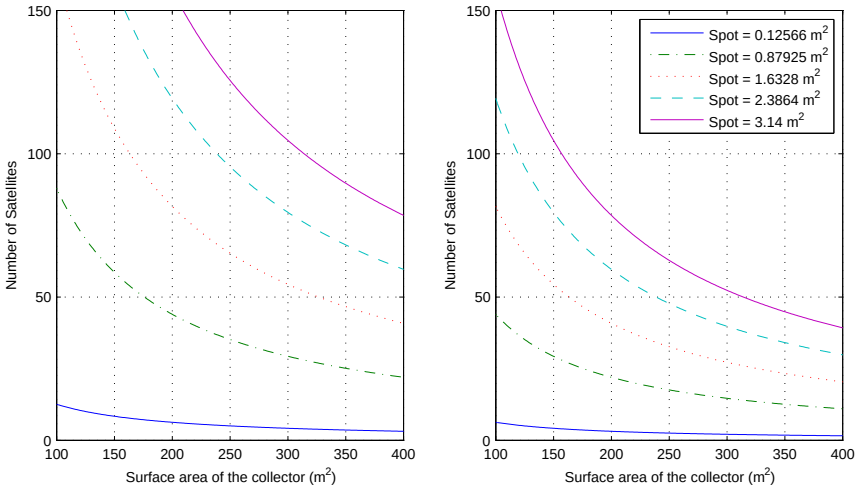

(a) System efficiency of 20%.

(b) System efficiency of 40%.

Figure 3.14: Surface area of reflector versus number of spacecraft, for various concentration ratios.

4 Spacecraft Dynamics and Control

4.1 Introduction

In this section we will analyse the dynamics of the spacecraft in the proximity of the asteroid. The aim of this section is to identify possible solutions to properly place the spacecraft close enough to the asteroid to guarantee the required power density and far enough from the plume or from any eclipse or occultation that my prevent the spacecraft from seeing the Sun.

The analysis of the dynamics and control of the mirror in the proximity of the asteroid is one of the key points of this study for the following reasons:

- One of the main issues related to the use of this deflection strategy is the contamination of the system (collector and beaming device) due to the debris coming from the asteroid during the deflection process.
- The relative motion of the spacecraft with respect to the asteroid imposes some severe constraints on the control of the projected beam of light both for the direct imaging and for the laser concept.
- The use of a single mirror implies a number of difficulties in the control of the orbit and attitude of the spacecraft and in the overall system design. On the other hand, the use of multiple mirrors will require pointing control of the beams in order to maintain the superposition.

We propose the study of two different ways of positioning and controlling the spacecraft in the proximity of the asteroid: close formation and artificial equilibrium points.

4.2 Mirror configurations

Two mirror assembly configurations were chosen for further study: an adjustable convex reflector (see Fig. 2.1a), and a fixed parabolic reflector (see Fig. 2.1c). The first, due to the ability to alter the location of focal point, can focus the light directly onto the surface of the asteroid without the need for any secondary directional system. This means a simpler design however requires that the spacecraft orbit in relatively close position to the asteroid.

Due to the large size of the spacecraft design, the perturbing forces, and in particular solar radiation pressure (SRP) must be accounted for in the design and analysis of the orbit and orbital maintenance. Figure 4.1 shows the effect of

Table 4.1: Estimated and observed orbital and physical properties of Apophis 99942.

Element		Measured Value
Semi-major axis	a_{A}	0.9223 AU
Eccentricity	e_{A}	0.1911
Inclination	i_{A}	0.05814 rad
Right ascension of the ascending node	Ω_{A}	3.5683 rad
Argument of periapsis	ω_{A}	2.2059 rad
Period	T_{A}	323.50 days
Mean motion	n_{A}	$2.2479E$-7 rad/s
Mass	m_{A}	$2.7E10$ kg
Gravitational constant	μ_{A}	$1.8015993E$-9 km^3/s^2
Physical dimensions*	a_I, b_I, c_I	191 m, 135 m, 95 m
Rotational velocity	w_{A}	$5.8177E$-5 rad/s

* The physical dimensions estimated using an ellipsoidal model for the asteroid, based on the observed magnitude, where $a_{\text{I}} \leq b_{\text{I}} \leq c_{\text{I}}$ are the three radii along the three orthogonal axes (see Fig. 4.2) [30].

SRP on the various configuration options for the focusing and beaming assembly, presented in Section 2.

4.3 Asteroid deflection model

From the initial observations, Apophis is expected to have a close encounter with the Earth in 2029. During that event Apophis could pass through a gravitational keyhole, a precise region in space no more than about 400 m across, which would set up future resonant impacts starting on 13 April 2036. Table 4.1 give the orbital and physical data for the asteroid [29].

The minimum orbital intersection distance (MOID) is defined as the separation distance at the closest point between two orbits, e.g. Apophis and the Earth. The deviation distance is defined here as the difference in r_{A} between the original, undeviated orbit and the deviated orbit at t_{MOID} [2]. Non-linear equations were derived for determining the difference in r_{A} are expressed as a function of the ephemeris in the Hill reference frame $\mathcal{A}$ (see Fig. 4.3) centered on the asteroid, with $\mathbf{\Delta k}$ giving the difference in Keplerian parameters between the undeviated and deviated orbit.

The deflection formulas in [2] are based on proximal motion kinematics and, though of general validity (see the book of Schaub and Junkins [31] for more details on proximal motion in general), are based on a first order approximation. However, if the relative distance between spacecraft and asteroid increase with respect to the length of the Sun-Asteroid vector or the deflection at the Earth increase with respect to the length of the Sun-Earth vectors, then the accuracy is compromised.

Therefore, we derived a more general set of fomulas that contain no approximation:

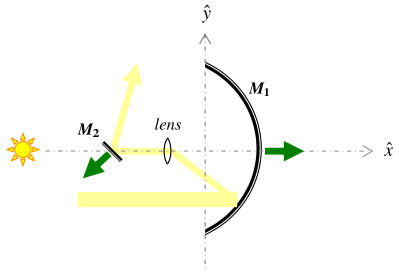

(a) Parabolic reflector with collimating lens, and steering mirror.

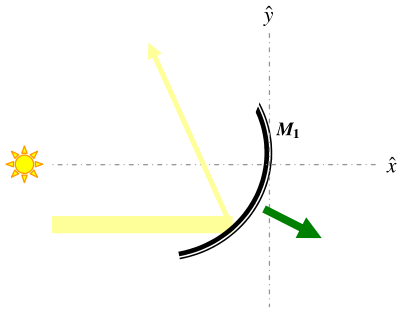

(b) Direct imaging using an adjustable reflector.

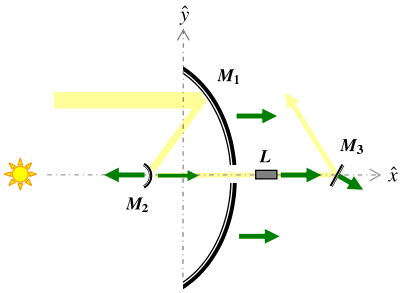

(c) Dual reflector system with a solar-fed laser followed by a steering mirror.

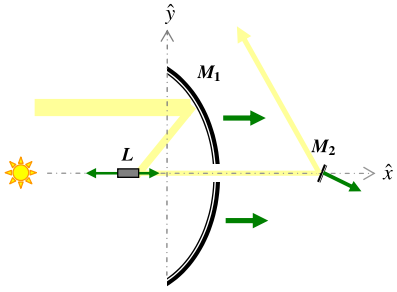

(d) Single reflector with solar-pumped laser and rear directional mirror.

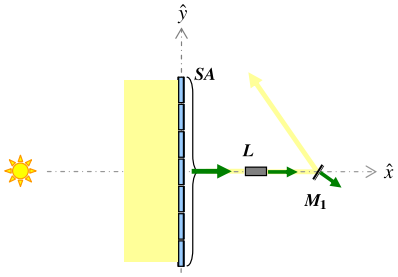

(e) Solar array for an indirect pumped laser system.

Figure 4.1: Forces due to SRP on the different configuration options for the mirror assembly.

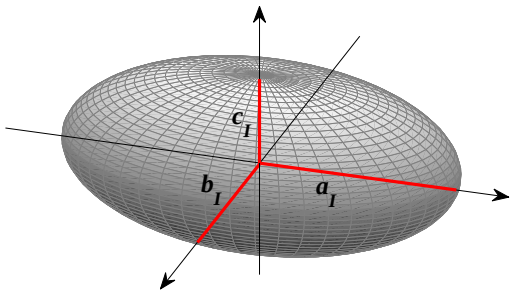

Figure 4.2: Ellipsoid model used for the asteroid, with a_I, b_I and c_I giving the radial dimensions.

$$\Delta\mathbf{r} = \begin{bmatrix} \varrho\cos\theta + \zeta\sin\theta \\ -\zeta\cos\theta + \varrho\sin\theta \\ -\cos(\Delta\theta-\theta)\sin\Delta\Omega\sin i + \varpi\sin(\Delta\theta-\theta) \end{bmatrix} \tag{4.1}$$

where

$$\varpi = \cos i\sin(\Delta i - i) + \cos\Delta\Omega\cos(\Delta i - i)\sin i \tag{4.2a}$$
$$\xi = \cos\Delta\Omega\cos(\Delta i - i)\cos i - \sin(\Delta i - i)\sin i \tag{4.2b}$$
$$\varrho = -\cos\Delta\Omega\cos(\Delta\theta-\theta) + \cos(\Delta i - i)\sin\Delta\Omega\sin(\Delta\theta-\theta) \tag{4.2c}$$
$$\zeta = \cos i\cos(\Delta\theta-\theta)\sin\Delta\Omega + \xi\sin(\Delta\theta-\theta) \tag{4.2d}$$

In the remainder of this report, the $\Delta\mathbf{r}$ in (4.1) will be used to compute both the relative position of the spacecraft with respect to the asteroid and the deflection at the Earth.

By definition of the coordinate system, $\mathbf{r}_A = [r_A,\ 0,\ 0]^T$. The change in the orbital parameters are calculated by numerically integrating the Gauss planetary equations [32] using a tangential thrust vector $\mathbf{u}_{dev}$ induced by the sublimation method.

$$\Delta k = \int_{t_0}^{t_i} \frac{dk(\mathbf{u}_{dev})}{dt}\,dt \tag{4.3}$$

The change in angular location, in this case given by the mean anomaly, is calculated at the MOID by [2],

$$\Delta M = \int_{t_0}^{t_i} \frac{dM}{dt}\,dt + n_{A_0}\left(t_0 - t_{\mathrm{MOID}}\right) + n_{A_i}\left(t_{\mathrm{MOID}} - t_i\right) \tag{4.4}$$

where the mean motion is given by,

$$n = \sqrt{\frac{\mu}{a^3}}$$

The thrust produced by the deflection method is a direct function of the rate of the expelled surface matter, $\dot{m}_{exp}$[8].

$$\frac{dm_{exp}}{dt} = 2v_{rot}\int_{y_0}^{y_{max}}\int_{t_{in}}^{t_{out}} \frac{1}{H}\left(P_{in} - Q_{rad} - Q_{cond}\sqrt{\frac{1}{t}}\right)\,dt\,dy \tag{4.5}$$

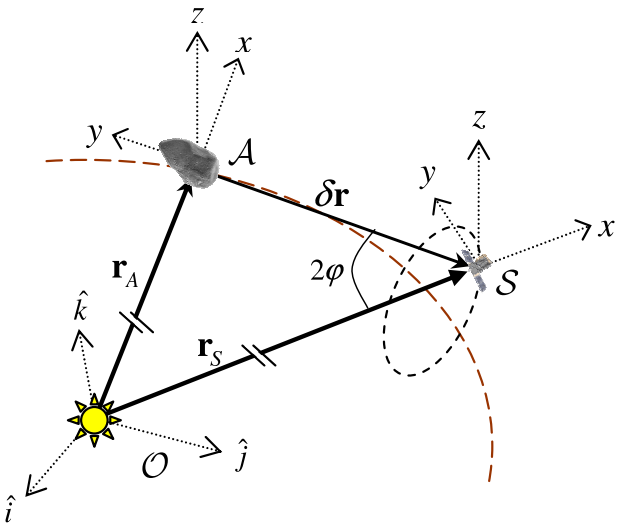

Figure 4.3: Definition of relative reference frames: $\mathcal{A}$ which is centered on the asteroid, and $\mathcal{S}$ which is centered on the spacecraft. Both are measured in radial x, transversal y and normal z directions.

where $[t_{in}, t_{out}]$ is the duration for which the point is illuminated, $[y_0, y_{max}]$ are the limits of the vertical illuminated surface area (i.e. orthogonal to the direction of rotation of the asteroid v_{rot}), H is the enthalpy of sublimation, P_{in} is the input power due to the solar concentrators, Q_{rad} is the heat loss due to black-body radiation and Q_{cond} is the conduction loss.

The magnitude of the induced acceleration can then determined by [8],

$$\mathbf{u}_{dev} = \frac{\Lambda\, \overline{v}\, \dot{m}_{exp}}{m_{A_i}} \cdot \hat{\mathbf{v}}_{\mathrm{A}} \tag{4.6}$$

where $\hat{\mathbf{v}}_{\mathrm{A}}$ is direction of velocity vector of the NEO, $\Lambda \simeq \left(\frac{2}{\pi}\right)$ is the scattering factor assuming the debris plume is uniformly distributed over a half-sphere, $\overline{v}$ is the average velocity of the debris particles according to Maxwell's distribution of an ideal gas, and the remaining mass of the asteroid m_{A_i} is calculated by numerically integrating (4.5).

4.4 Spacecraft orbital dynamics

4.4.1 Artificial equilibrium points

If solar pressure and the gravity field of the asteroid are taken into account then the mirrors can be designed so that the two forces are in equilibrium, with the spacecraft hovering at a fixed location and distance from the asteroid, using the single-mirror configuration to control the beam. These points, called here artificial equilibrium points (AEP), are in fact static points where the forces are balanced, or momentarily in equilibrium. It should be noted, these are not in dynamic equilibrium in which the spacecraft could remain indefinitely at a fixed point in space, due to the constantly changing forces at work.

If we consider a perfectly spherical and homogenous gravity field of the asteroid, the dynamics of the mirror is governed by the following set of equations,

$$\ddot{x} = 2\dot{\nu}(\dot{y} - y\frac{\dot{r}_A}{r_A}) + x\dot{\nu}^2 + \frac{\mu_\odot}{r_A^2} - \frac{\mu_\odot}{\delta r^3}(r_A + x) - \frac{\mu_A}{\delta r^3}x + \frac{F_{s_x}(x,y,z)}{m_{sc}} + \frac{F_{u_x}}{m_{sc}} \tag{4.7a}$$

$$\ddot{y} = -2\dot{\nu}(\dot{x} - x\frac{\dot{r}_A}{r_A}) + y\dot{\nu}^2 - \frac{\mu_\odot}{r_{sc}^3}y - \frac{\mu_A}{\delta r^3}y + \frac{F_{s_y}(x,y,z)}{m_{sc}} + \frac{F_{u_y}}{m_{sc}} \tag{4.7b}$$

$$\ddot{z} = -\frac{\mu_\odot}{r_{sc}^3}z - \frac{\mu_A}{\delta r^3}z + \frac{F_{s_z}(x,y,z)}{m_{sc}} + \frac{F_{u_z}}{m_{sc}} \tag{4.7c}$$

where m_{sc} is the estimated mass of the spacecraft, $\mathbf{F}_{\text{SRP}} = [F_{s_x}, F_{s_y}, F_{s_z}]$ is the solar force in (4.21) and $\mathbf{F}_u = [F_{u_x}, F_{u_y}, F_{u_z}]$ is the control force. We are now interested in solutions of the following system,

$$2\dot{\nu}(-y\frac{\dot{r}_A}{r_A}) + x\dot{\nu}^2 + \frac{\mu_\odot}{r_A^2} - \frac{\mu_\odot}{r_{sc}^3}(r_A + x) - \frac{\mu_A}{\delta r^3}x + \frac{F_{s_x}(x,y,z,\beta,f_\ell)}{m_{sc}} = 0 \tag{4.8a}$$

$$-2\dot{\nu}(-x\frac{\dot{r}_A}{r_A}) + y\dot{\nu}^2 - \frac{\mu_\odot}{r_{sc}^3}y - \frac{\mu_A}{\delta r^3}y + \frac{F_{s_y}(x,y,z,\beta,f_\ell)}{m_{sc}} = 0 \tag{4.8b}$$

$$-\frac{\mu_\odot}{r_{sc}^3}z - \frac{\mu_A}{\delta r^3}z + \frac{F_{s_z}(x,y,z,\beta,f_\ell)}{m_{sc}} = 0 \tag{4.8c}$$

The third equation (4.8c) is always satisfied if the mirror is in the x_{M}-y_{M} plane therefore in the following we will focus on the motion in this plane. Now, considering that the mirror has to constantly reflect the light onto the surface of the asteroid, if the mirror is flat the only possible equilibrium configuration is with the asteroid-mirror direction aligned with the spacecraft-Sun direction. If the mirror is not flat, then we can look for possible position vector $\delta\mathbf{r}$, solar aspect angle β and focal distance f_ℓ such that the vector $\mathbf{F}_{\text{SRP}}$ is aligned with the asteroid-mirror direction (see Fig. 4.4).

Figure 4.6 represents the misalignment of the force vector due to the solar pressure with respect to the spacecraft-asteroid direction. The angle β is the direction of the light impacting on the mirror while $\Delta\beta$ is the angle between the incoming sunlight and the direction of the focal point of the mirror. The direction of the focal point identifies the pointing direction. We consider only one quadrant of the Hill frame with positive x and negative y. For positive x and positive y the solutions are symmetric; there are no solutions in the other two quadrants.

As it can be seen for $\beta = \pi/2$, the only artificial equilibrium points are along the Sun-asteroid direction. However, in this case the mirror would be in shadow and therefore no equilibrium points can exist along that direction. For higher values of β, equilibrium points can exist at higher angular distances from the radial direction. For example, for $\beta = 139°$ the mirror can be placed at $\delta\mathbf{r} = [1.3699, 0.48225, 0]$ km, which is about 20° from the radial direction (Fig. 4.5 shows the level of acceleration acting on the spacecraft).

This artificial equilibrium point offers a good location for projecting the light of the Sun on the side of the asteroid along the y direction, and away from the plume of gases. If we assume that the lens produces a collimated light beam with negligible divergence, and that the beam is projected at the intersection

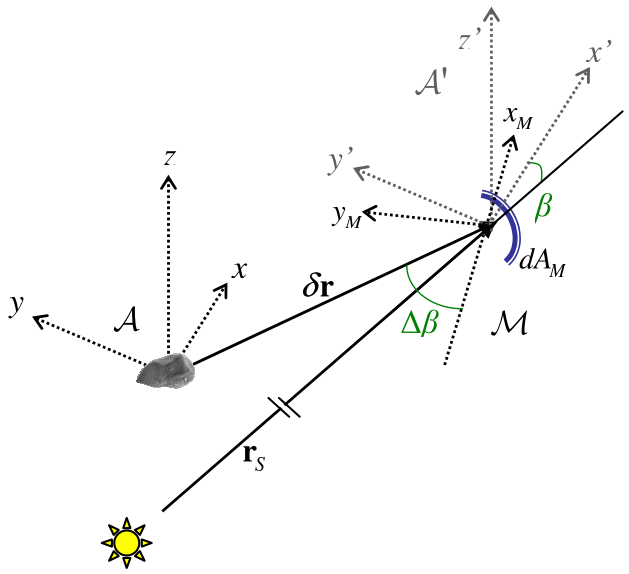

Figure 4.4: Definition of mirror-centric relative reference frame $\mathcal{M}$. The reference frame $\mathcal{A}'$ is the translated from the barycenter of the asteroid to that of the mirror, with $\mathcal{A}' \parallel \mathcal{A}$.

of the surface of the asteroid with the y-axis, then we can compute where the two extreme points of the beam intersect the surface of the asteroid. From this intersection, we can compute the spot size given the beam size and the elevation over the y-axis. As can be seen in Fig. 4.8, for a beam size between 0.5 and 1 m in diameter, the increase in spot size due to an elevation of 70° degrees along the y-axis and 20° from the radial x-axis, is still limited.

It should be noted that due to the movement of the asteroid along its orbit the AEPs do not keep a fixed position since the modulus of the solar force is changing with the inverse of the square of the distance from the Sun. If we compute the AEP for every position of the asteroid along its orbit we get the result in Fig. 4.9.

These results are useful to identify AEPs in the case of a perfectly spherical asteroid. On the other hand, the actual shape of Apophis and of a general asteroid cannot be considered spherical, therefore consistent with studies by other authors, the asteroid was modeled as an ellipsoid with semi-axes a_I, b_I and c_I (see Table 4.1). We assume that the semi-axis c_I is aligned with the z-axis of the $\mathcal{A}$ Hill frame and that the asteroid is rotating around the z-axis with angular velocity w_A. The gravity field of the asteroid can be expressed as the sum of a spherical field plus a second-degree and second-order field [33, 34],

$$U_{20+22} = \frac{\mu_{\mathrm{A}}}{\delta r^3}\left(C_{20}\left(1-\frac{3}{2}\cos^2\gamma\right)+3C_{22}\,\cos^2\gamma\cos 2\kappa\right) \tag{4.9}$$

where the harmonic coefficients C_{20} and C_{22} can be expressed as a function of

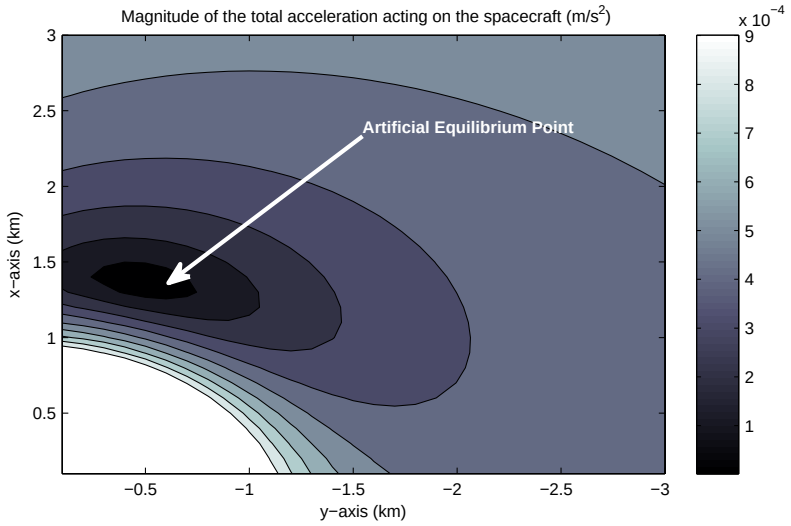

Figure 4.5: Example of AEP at 20° from the radial direction.

the semi-axes,

$$C_{20} = -\frac{1}{10}(2c_I^2 - a_I^2 - b_I^2) \tag{4.10a}$$

$$C_{22} = \frac{1}{20}(a_I^2 - b_I^2) \tag{4.10b}$$

where κ is defined as,

$$\kappa = \arctan\left(\frac{y}{x}\right) + w_A\, t$$

and $\gamma = 0$ since we are only interested in the in-plane motion. The angular speed is assumed to be $w_A = 5.8177E\text{-}5$ rad/s, or one revolution every 30 hours [8]. Therefore, the equations for the orbital dynamics of the spacecraft can be expressed as,

$$2\dot{\nu}(-y\frac{\dot{r}_A}{r_A}) + x\dot{\nu}^2 + \frac{\mu_\odot}{r_A^2} - \frac{\mu_\odot}{r_{sc}^3}(r_A + x) - \frac{\mu_A}{\delta r^3}x + \frac{F_{s_x}(x,y,z,\beta,f_\ell)}{m_{sc}} + \frac{\partial U_{20+22}}{\partial x} = 0 \tag{4.11a}$$

$$-2\dot{\nu}(-x\frac{\dot{r}_A}{r_A}) + y\dot{\nu}^2 - \frac{\mu_\odot}{r_{sc}^3}y - \frac{\mu_A}{\delta r^3}y + \frac{F_{s_y}(x,y,z,\beta,f_\ell)}{m_{sc}} + \frac{\partial U_{20+22}}{\partial y} = 0 \tag{4.11b}$$

$$-\frac{\mu_\odot}{r_{sc}^3}z - \frac{\mu_A}{\delta r^3}z + \frac{F_{s_z}(x,y,z,\beta,f_\ell)}{m_{sc}} + \frac{\partial U_{20+22}}{\partial z} = 0 \tag{4.11c}$$

Note that even in this case (4.11c) is satisfied for $z = 0$. If the actual shape of the asteroid is considered the AEP position is not moving along a rectilinear line anymore but is following a spiralling path as in Fig. 4.10.

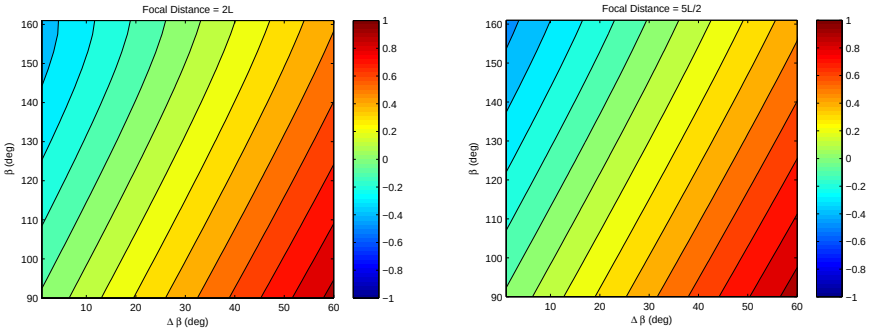

(a) Misalignment for a focal distance equal to $2L$.

(b) Misalignment for a focal distance equal to $2.5L$.

Figure 4.6: Misalignment between the position vector $\delta\mathbf{r}$ and the direction of resultant force due to solar pressure, where L is the length of the projection of the mirror on the y_{M} axis.

4.4.1.1 AEP in three dimensional space

The analysis in the previous section was useful to identify the existence of regions around the asteroid where it is possible to have a balance between the solar pressure and the gravity attraction. The initial analysis was performed considering only the two dimensional motion and a high concentration ratio, i.e. short focal distance and small size of the mirror. As a consequence the elevation from the y-axis and distance from the centre of the asteroid were limited. In fact at low elevation angles, equilibrium points may exist only for high solar aspect angles. However, for short focal distances, high curvature of the mirror and high solar aspect angles, the edges of the mirror were shadowing part of its surface.

If the direct imaging concept is used, then the focal point is at the asteroid and the mirror is almost flat. This removes the limitation on the elevation angle and on the solar aspect angle. Furthermore, an increase in the surface area implies a higher solar pressure and therefore a demand for a closer positioning of the mirror with respect to the asteroid. We can estimate the distance from the asteroid for different surface areas and different spacecraft masses by integrating,

$$dF = \frac{\mu_{\text{A}}}{\delta r^2} - P_r \sigma_{\text{M}} \frac{A_{\text{M}}}{m_{sc}} = 0 \tag{4.12}$$

where P_r is the solar pressure at a distance $r_{\odot/s}$ from the Sun given by,

$$P_r = \frac{S_0}{c}\left(\frac{r_{\text{AU}}}{r_{\odot/sc}}\right)^2 = P_0\left(\frac{r_{\text{AU}}}{r_{\odot/sc}}\right)^2 \tag{4.13}$$

S_0 is the solar flux, c is the speed of light, μ_{A} is given in Table 4.1, σ_{M} is the coefficient of reflectivity of the mirror, A_{M} is the perpendicular surface area, and r_{sc} and r_{AU} are the distance between the Sun and spacecraft, and the Sun and the Earth (1 AU) respectively.

For a distance of $r_{sc} = 1$ AU, (4.12) gives the curves in Figs. 4.11a and 4.11b for a spacecraft mass of 1000 kg and 2000 kg respectively, where the curve

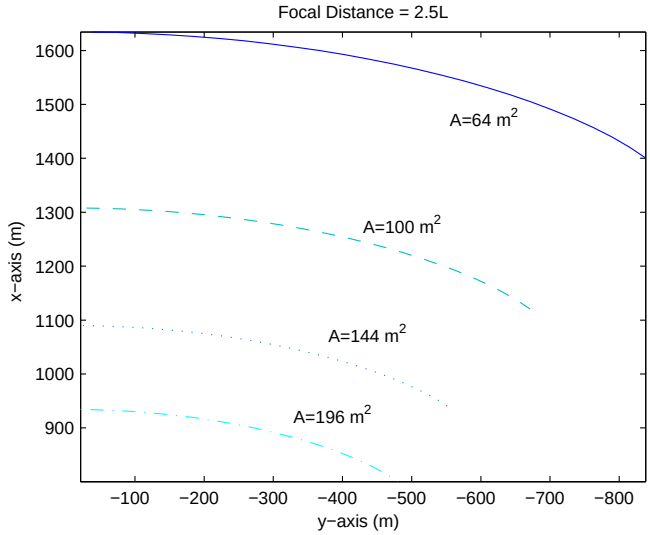

Figure 4.7: Artificial equilibrium points for different mirror sizes.

labeled with $r - Sp$ represent the equilibrium between gravity attraction and solar pressure for each distance and surface area. On the same graph, the curves were plotted at constant concentration factors in the range [20, 200]. The two plots shows that for a low concentration factor the surface area of the mirror is small and therefore the distance from the asteroid can be high. On the other hand, for high concentration factors the surface area of the mirror is high and the distance from the asteroid must be low to have a balance between gravity and solar pressure.

The situation works concurrently, because for a shorter distance from the asteroid would imply little space to place multiple mirrors while larger distance would allow for multiple spacecraft. On the other hand a larger distance implies bigger mirrors. As a consequence, if we consider a constant concentration factor, the number of spacecraft that can be placed on the surface of a sphere centred in the asteroid is constant with the distance from the asteroid. For example if we consider a concentration factor of 2000 and an arc of 60° on each side of the y-z plane, we could accommodate 5 satellites, each one with an edge length (assuming a square shape) of 288 m. If the concentration factor is reduced to 100 then we can accommodate 22 spacecraft with an edge length of 64 m.

On the other hand, the distance from the asteroid is limited by the size of the asteroid, the extension of the plume and the shadow projected by the asteroid. If we move away from the curve with zero dF, in Fig. 4.11, along a curve with constant concentration factor, we can increase the distance from the asteroid but the solar pressure would dominate the gravity attraction. An alternative is to compensate for the unbalanced force with a low thrust propulsion system.

Figure 4.12 shows the strategy in the two dimensional case (i.e. x-y plane only). Assuming an elevation of 60°, the plume can flow in to a cone with an angular extension of up to 120° (red line). Higher elevations are limited by the shadow projected by the asteroid. Furthermore the plume is partially shadowing the mirrors. The number of spacecraft is therefore limited. Note

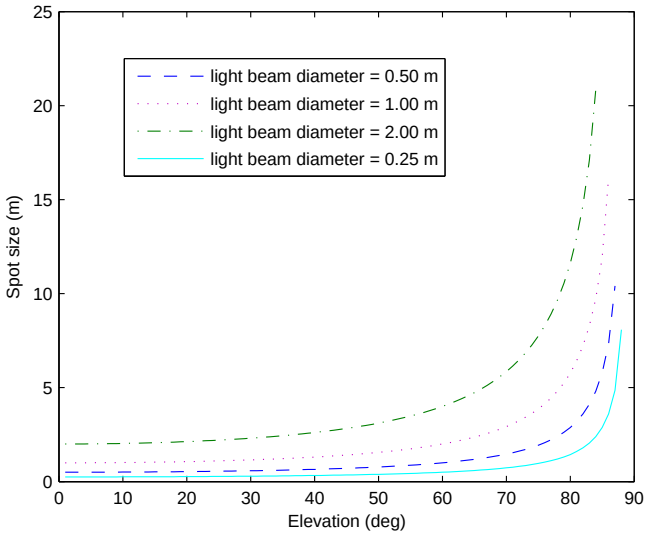

Figure 4.8: Increase in the spot size as a function of the elevation above the y axis.

that the spacecraft can be equally placed ahead of the asteroid or trailing the asteroid (as in Fig. 4.12) but not on both sides.

It is worth to underline that the strategy in Fig. 4.12 is based on the assumption that thrusting along the y axis is optimal for this deflection method (see [2, 1, 35] for further reference on the optimality of deflection methods). Thrusting along x would solve a number of problems and would allow placing the spacecraft both along the positive and negative y axis. On the other hand thrusting in the x direction is suboptimal for long warning times [2, 35] and requires a higher level of thrust which implies more satellites.

Figure 4.13 instead shows the strategy in the three dimensional case. The spacecraft are clear of the plume and can be placed on both sides of the plume (along the z axis) at any elevation angle apart from the shadow cone projected by the asteroid. High elevations would however lead to a stretch of the spot on the surface of the asteroid, therefore, even in this case a good compromise is required.

The other interesting aspect is that the concentration factor is proportional to the inverse of the square of the distance from the Sun, therefore as the spacecraft moves toward the Sun the power collected increases and the concentration factor decreases, while moving away from the Sun the concentration factor increases and the power of the Sun light decreases. The product of the two remains constant, if the curvature of the mirror can be adapted, therefore the power density on the surface of the asteroid remains constant.

The approach used to design the mirror in three dimensions is similar to the one used in two dimensions. We define a local mirror reference frame $\mathcal{M}$ (see Fig. 4.14) and express the position of the light source $(x_\odot,\ y_\odot,\ z_\odot)$ and of the focal point $(x_f,\ y_f,\ z_f)$ in this reference frame. For each triplet $(x,\ y,\ z)$ we can define the direction of the normal vector $\hat{\mathbf{n}}$ such that a ray coming from the source of light is reflected onto the focal point. For each surface element we can

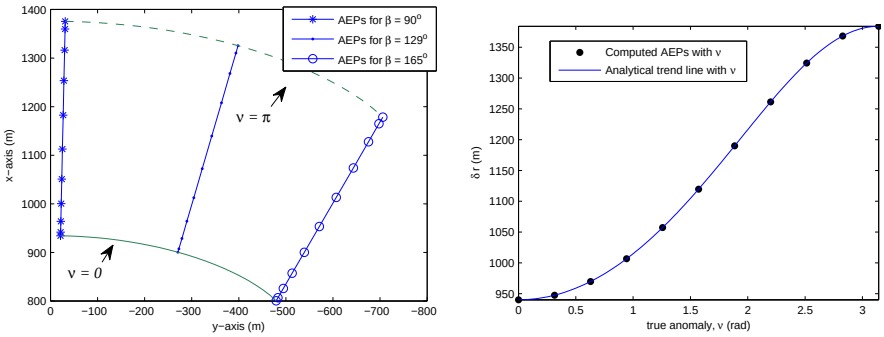

(a) Position of the equilibrium points over a full orbit of the asteroid Apophis.

(b) Variation of the position of the AEP for a mirror attitude of 129°, over half an orbit.

Figure 4.9: Variation of the equilibrium points with the true anomaly for $A = 196\ \mathrm{m}^2$.

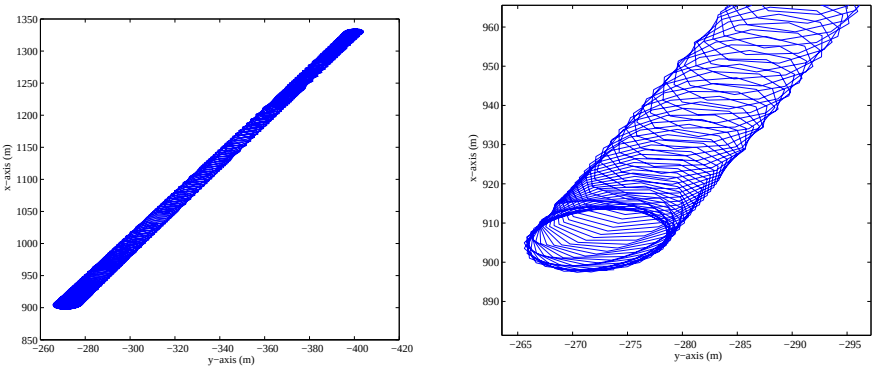

(a) Overview.

(b) Close-up view.

Figure 4.10: Variation of the equilibrium points with the true anomaly for a mirror of surface area $A = 196\ \mathrm{m}^2$, and using an ellipsoidal model for the asteroid.

then compute the magnitude of the solar force in the mirror reference frame F_{M},

$$\mathbf{F}_{\mathrm{M}} = 2\sigma_{\mathrm{M}} P_r \int_{A_{\mathrm{M}}} \cos^2\phi\ \hat{\mathbf{n}}\ dA \tag{4.14}$$

where ϕ is the angle of reflection, and P_r is the solar pressure at a distance $r_{\odot/s}$ from the Sun given by (4.13).

The force vector in the mirror reference frame $\mathcal{M}$ is then transformed in the force vector defined in the local Hill reference frame $\mathcal{S}$ through the rotation matrix $\mathbf{Q}(\mathbf{q})$,

$$\mathbf{F}_s = \mathbf{Q}(\mathbf{q})\mathbf{F}_{\mathrm{M}} \tag{4.15}$$

Therefore for each position of the mirror in the spacecraft-centric Hill reference frame $\mathcal{S}$, the goal is to find the correct attitude and shape of the mirror that allows an equilibrium state between the gravity force and solar pressure force.

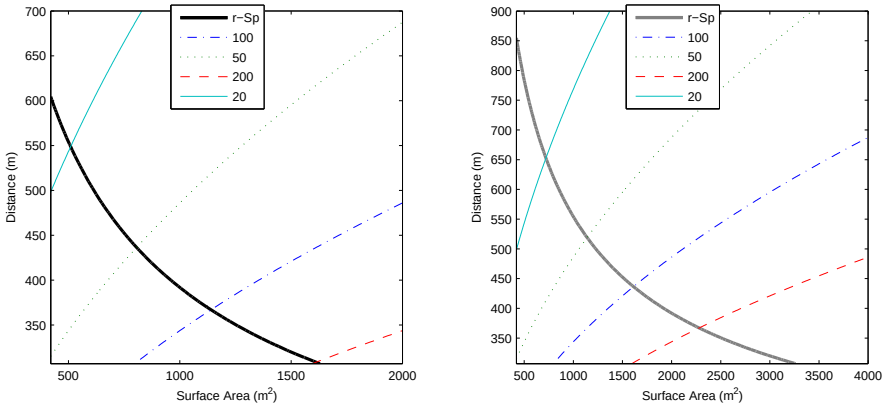

(a) Spacecraft mass of 1000 kg. (b) Spacecraft mass of 2000 kg.

Figure 4.11: Balance between solar pressure and gravity forces.

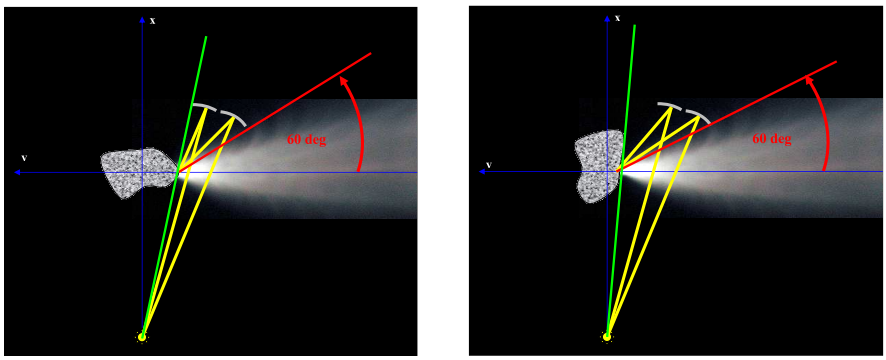

(a) Asteroid *major* axis along y-axis. (b) Asteroid *minor* axis along y-axis.

Figure 4.12: Spacecraft configuration with respect to the asteroid.

Due to the limited time of this study we could map completely the space around Apophis. However, regions of equilibrium exist also in the 3D case, but if the right concentration factor for a direct imaging is used they are too close to the asteroid.

A possible solution would be to move away from the equilibrium positions and use a low-thrust system to compensate for the solar pressure (the dominant component). The other possibility is to use a solar pumped laser also in this case. If a solar pumped laser solution is adopted, then smaller mirrors can be used and the analysis of the 2D case is valid.

4.4.2 Funnel reference orbits

An alternate approach is to have the mirrors flying in formation with the asteroid, orbiting in tandem around the Sun. The spacecraft have to maintain their relative position with respect to the asteroid in order to keep the required

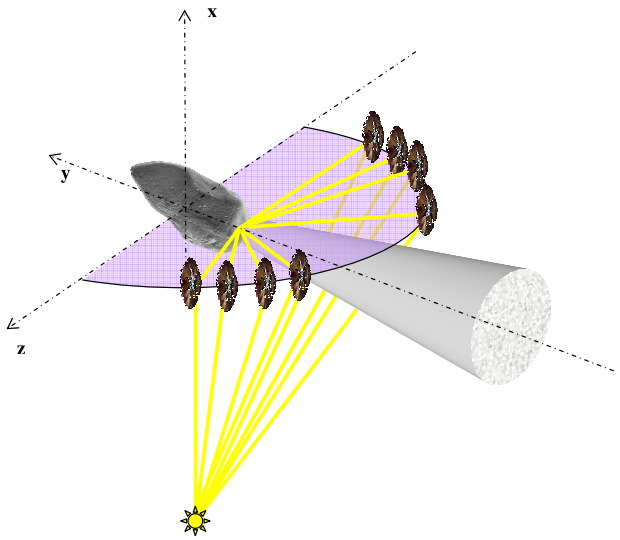

Figure 4.13: Spacecraft configuration in 3D

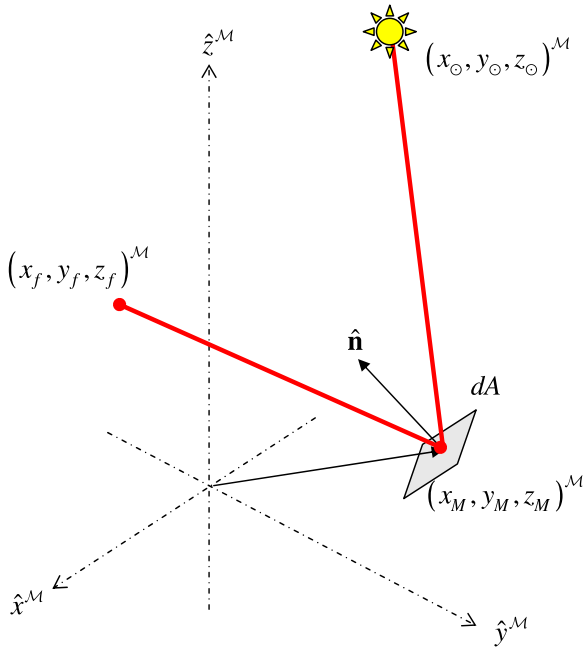

Figure 4.14: Reference frame for the three dimensional mirror design.

power density on the same spot of the surface of the asteroid. Therefore, the formation orbits have to be periodic and in close proximity with low excursion in the relative distance from the asteroid. On the other hand the spacecraft should avoid, as much as possible, to fly in the irregular regions of the gravity field of the asteroid. In addition, should also avoid any impingement with the

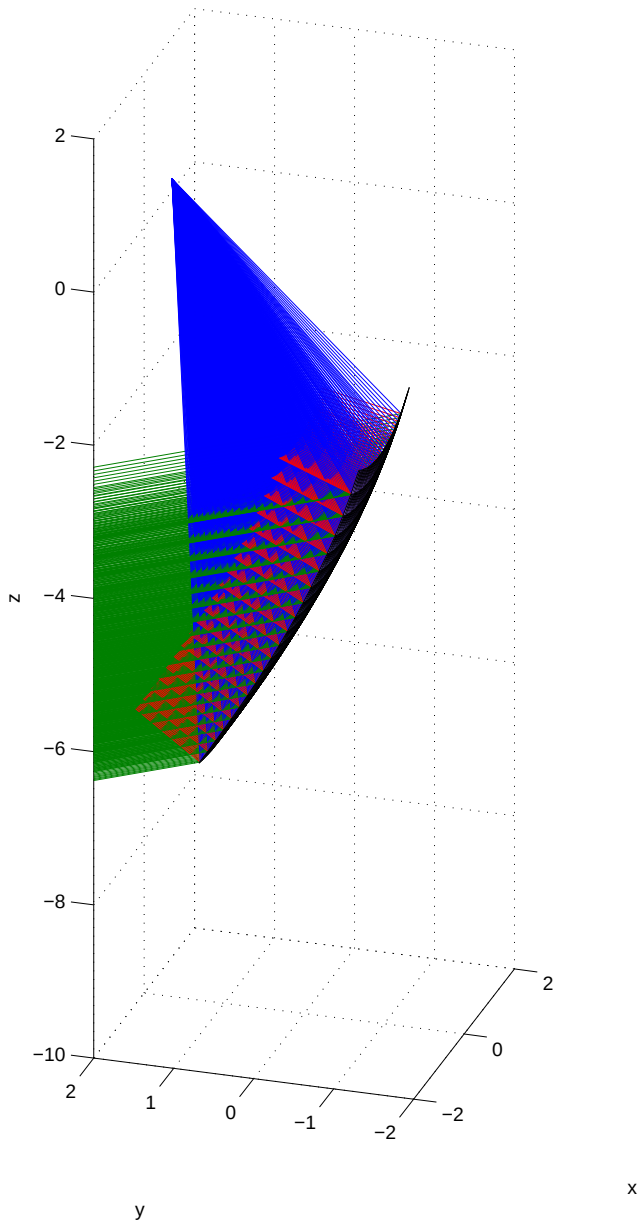

Figure 4.15: Example of a single mirror projecting the light of Sun onto the focal point. Green lines are the Sun rays, blue lines are the reflected rays, red lines are the local normals to the surface of the mirror. The mirror is represented in the mirror reference frame $\mathcal{M}$. Axes are reported in normalised units.

plume of debris and gas coming from the sublimation of the surface material. In order to design the desired formation orbits, we start by considering the relative equations of motion which use the orbital element differences between a chief orbit (which can be virtual, and is located at the origin of the Hill reference frame) and a spacecraft in the formation [31].

$$\ddot{x}(t) = 2\dot{\nu}\left(\dot{y} - y\frac{\dot{r_{\mathrm{A}}}}{r_{\mathrm{A}}}\right) + x\dot{\nu}^2 + \frac{\mu_\odot}{r_{\mathrm{A}}^2} - \frac{\mu_\odot}{r_{sc}^3}\left(r_{\mathrm{A}} + x\right) \tag{4.16a}$$

$$\ddot{y}(t) = -2\dot{\nu}\left(\dot{x} - x\frac{\dot{r_{\mathrm{A}}}}{r_{\mathrm{A}}}\right) + y\dot{\nu}^2 - \frac{\mu_\odot}{r_{sc}^3}y \tag{4.16b}$$

$$\ddot{z}(t) = \frac{\mu_\odot}{r_{sc}^3}z \tag{4.16c}$$

with

$$\mathbf{r}_{sc} = \mathbf{r}_{\mathrm{A}} + \delta\mathbf{r}, \;\; r_{sc} = \sqrt{\left(x + r_{\mathrm{A}}\right)^2 + y^2 + z^2}$$

where $\mathbf{r}_{sc}$ and $\mathbf{r}_{\mathrm{A}}$ are the vectors from the Sun to the formation spacecraft and asteroid respectively, and $\dot{\nu}$ is the angular rate of change of the solar orbit. This is a first approximation of the motion of the spacecraft that does not take into account the gravity field of the asteroid and the solar pressure but it is useful to identify some orbit geometries that answer to our requirements.

The formation orbit can be thought of as an orbit around the Sun with a small offset in the initial position $\delta\mathbf{r}_0$ and velocity $\delta\mathbf{v}_0$. This offset can also be expressed as the difference between the orbital parameters of the chief (e.g. Apophis) and the formation. As long as there is no difference in semi-major axes, the two orbits will remain periodic.

$$\delta\mathbf{k} = \mathbf{k}_{sc} - \mathbf{k}_A = [\delta a \;\; \delta e \;\; \delta i \;\; \delta\Omega \;\; \delta\omega \;\; \delta M] \tag{4.17}$$

As the mean anomaly is a function of the semi-major axis, the difference in mean anomaly will remain constant through out the orbit so long as $\delta a = 0$.

Schaub and Junkins [31] developed a linear mapping between Hill frame coordinates, and orbit element differences. The linearisation holds true so long as $\delta r \ll r_{\mathrm{A}}$. For the deviation of the asteroid, however, a non-linear form of the relative motion equations had to be developed (see (4.1)) due to the larger scale of Δr. Since the computation time is roughly equivalent, the more exact, non-linear form was used for the formation orbits.

If the optimal thrust direction that maximizes the deviation is along the unperturbed velocity vector of the asteroid, [2] then the exhaust gases will flow along the y-axis of the local Hill reference frame. Therefore, the size of the formation orbits projected in the x-z plane should be maximal. All the requirements on the formation orbits can be formulated in mathematical terms as a multi-objective optimization problem,

$$\min_{\delta\mathbf{k}\in D} \min_{\nu} J_1 = \delta r \tag{4.18}$$

$$\min_{\delta\mathbf{k}\in D} \min_{\nu} J_2 = -\sqrt{x^2 + z^2} \tag{4.19}$$

subject to the constraint:

$$C_{ineq} = \min_{\nu} \left(\delta r(\nu) - r_{\mathrm{LIM}}\right) > 0 \tag{4.20}$$

where r_{LIM} is a minimum-radius sphere imposed to avoid non-linearities in the asteroid gravity field [14], and D is the search space for the solution vector $\delta\mathbf{k}$.

The problem in (4.18)–(4.20) was solved with a hybrid stochastic-deterministic approach based on a multiagent search technique combined with a decomposition of the search space [36, 37]. The result was several groupings, or *families*, of formation orbits. As can be seen in Fig. 4.16, the solutions are symmetrically distributed about the 0-value of the $\delta\mathbf{k}$ parameters. The existence of families can be seen, for example, through $\delta\omega$ and $\delta\Omega$, where for a given input value there are multiple values for the objective functions J_1 and J_2. Figure 4.17a shows the formation orbits in the $\mathcal{A}$ Hill frame. Figure 4.17b instead shows some particular solutions, close to the limit sphere. These solutions belong to four symmetric families of formation orbits, each one corresponding to a funnel.

4.5 Spacecraft orbital maintenance

4.5.1 Artificial equilibrium points

Solar pressure depends on the distance from the Sun, therefore, if the size of the mirror is constant, as the asteroid moves around the Sun the force acting to the spacecraft changes with the true anomaly ν. As a consequence, the position of the equilibrium points changes with time unless the orbit of the asteroid is circular.

Once the shape and orientation of the mirror are defined, the total force acting on the mirror assembly can be computed by integrating the following expression over the surface of the mirror A_M:

$$d\mathbf{F} = 2\sigma_{\text{M}} P_r \cos^2\phi\ \mathbf{n}\ dA \tag{4.21}$$

$$\mathbf{F}_{\text{SRP}} = 2\sigma_{\text{M}} P_r \int_{A_{\text{M}}} \cos^2\phi\ \hat{\mathbf{n}}\ dA \tag{4.22}$$

where σ_{M} is the efficiency of the mirror, or coefficient of reflectivity, and P_r is the solar pressure at a distance $r_{\odot/s}$ from the Sun given in (4.13). See Fig. 4.1b for the force diagram.

Figure 4.9a shows, for different attitudes of the mirror, the position of the equilibrium points over a full orbit of the asteroid Apophis. Figure 4.9b instead shows the variation of the position of the AEP for a particular attitude of the mirror, over half an orbit. The black dots represent the computed position of the equilibrium points for an angle $\beta = 129°$ while the continuous line is given by the following equations,

$$x_{\text{AEP}} = \delta r_{\text{AEP}_0} \cos\epsilon \left(\frac{1 + e\cos\nu_0}{1 + e\cos\nu}\right) \tag{4.23a}$$

$$y_{\text{AEP}} = \delta r_{\text{AEP}_0} \sin\epsilon \left(\frac{1 + e\cos\nu_0}{1 + e\cos\nu}\right) \tag{4.23b}$$

where

$$\epsilon = \arctan\left(\frac{y_{\text{AEP}}(\nu_0)}{x_{\text{AEP}}(\nu_0)}\right)$$

is the angular position of the AEP at $\nu = \nu_0$.

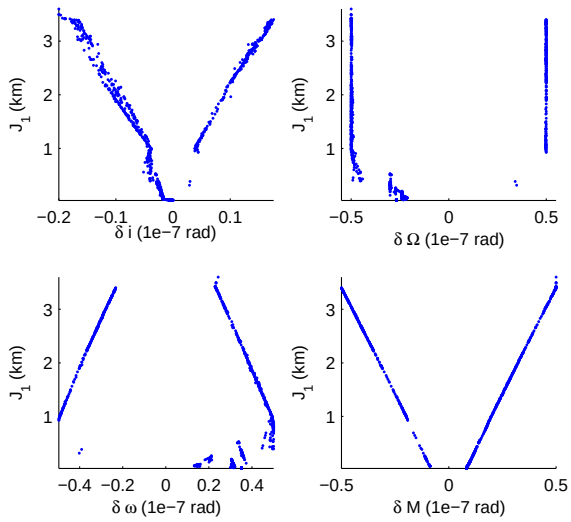

(a) J_1 set.

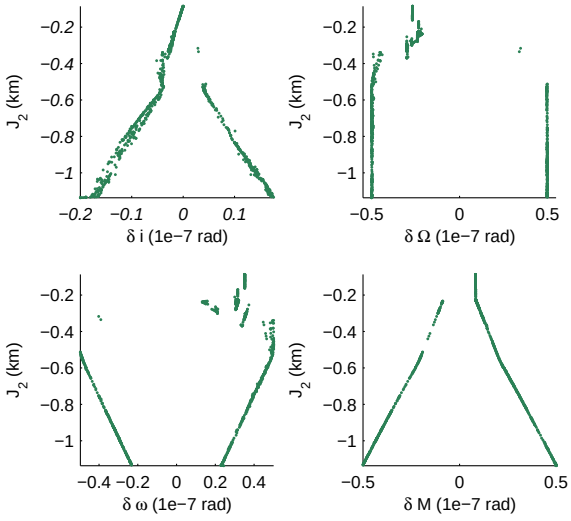

(b) J_2 set.

Figure 4.16: $\delta\mathbf{k}$ parameters of the set of Pareto optimal solutions.

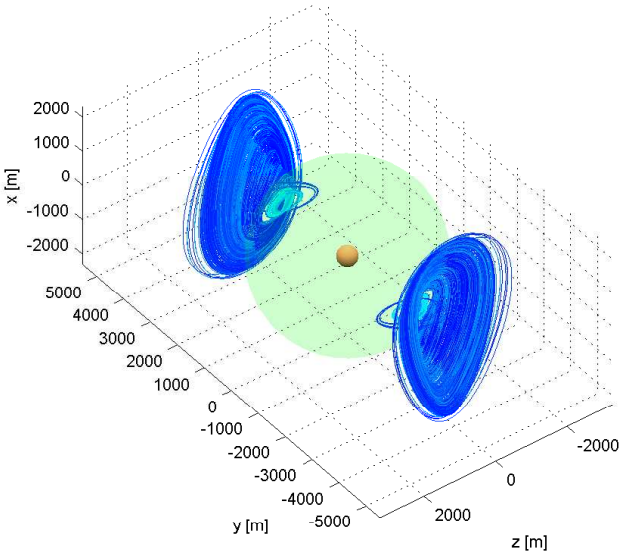

(a) Overview.

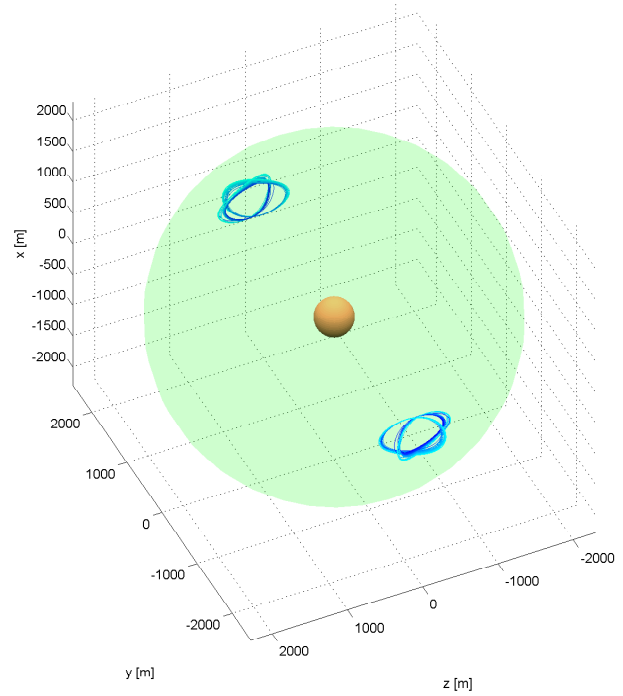

(b) Zoom, in close proximity to the NEO.

Figure 4.17: Funnel configuration for the solutions of (4.18).

Then, the distance of the AEP from the asteroid varies with the following law,

$$\delta r_{\text{AEP}} = \delta r_{\text{AEP}_0} \frac{1 + e\cos\nu_0}{1 + e\cos\nu} \tag{4.24}$$

Since the AEPs are moving a spacecraft placed at an AEP would depart toward the asteroid or away from the asteroid depending on the initial true anomaly ν. In particular, for the true anomaly $\nu \in [0,\, \pi]$ the spacecraft would fall toward the asteroid, while for $\nu \in [\pi,\, 2\pi]$ the spacecraft would escape along a radial direction.

We can envisage two strategies to maintain the orbital position of the mirror: we compensate for the between solar pressure and gravity attraction with an active control (low-thrust), or we let the spacecraft drift along the radial direction chasing the position of the equilibrium points.

In order to chase the AEPs the spacecraft has to move with the same kinematics, therefore we can impose the following velocity and acceleration,

$$\frac{dx}{dt} = \frac{d(\delta r_{\text{AEP}})}{dt}\cos\epsilon \qquad \frac{dy}{dt} = \frac{d(\delta r_{\text{AEP}})}{dt}\sin\epsilon \tag{4.25}$$

$$\frac{d^2x}{dt^2} = \frac{d^2(\delta r_{\text{AEP}})}{dt^2}\cos\epsilon \qquad \frac{d^2y}{dt^2} = \frac{d^2(\delta r_{\text{AEP}})}{dt^2}\sin\epsilon \tag{4.26}$$

with

$$\frac{d(\delta r_{\text{AEP}})}{dt} = \frac{\delta r_{\text{AEP}}^2 e\dot{\nu}\sin\nu}{\delta r_{\text{AEP}_0}} \tag{4.27}$$

$$\frac{d^2\left(\delta r_{\text{AEP}}\right)}{dt^2} = \frac{e\,\delta r_{\text{AEP}}}{\delta r_{\text{AEP}_0}}\left(2\,\delta\dot{r}_{\text{AEP}}\dot{\nu}\sin\nu + \delta r_{\text{AEP}}\dot{\nu}^2\cos\nu + \delta r_{\text{AEP}}\ddot{\nu}\sin\nu\right) \tag{4.28}$$

Equations (4.25) and (4.26) represent an imposed shape to the motion of the spacecraft. If we then substitute (4.23a), (4.25) and (4.26) into the dynamic equations in (4.11) and solve for the controls, we can get the required thrust components to follow the prescribed kinematics.

Figure 4.18 presents an example of the required thrust profile to maintain a fixed position for an AEP computed at the perihelion. By comparison, Fig. 4.19 shows the required control profile to make the spacecraft drift following the motion of the AEP for different values of the true anomaly. Both figures assume a spherical model for the asteroid.

As can be seen the control capability required to maintain a fixed position is greater than the one required to chase the AEP. A possible scenario, therefore, is that the swarm can be distributed around the asteroid at different angles ϵ and the mirrors would move back and forth along the radial directions. As can be seen from the figures, the control authority required to maintain the position of an AEP is several order of magnitude higher, though still very small, than what required to chase the AEP. Figure 4.20, instead, shows the required control profile to follow the motion of the AEP computed for a spherical asteroid when the gravity field for an elongated body is considered.

4.5.2 Funnel control

While the design of the artificial equilibrium points accounts for the additional perturbations, the funnel formation design does not. Instead, a control law is

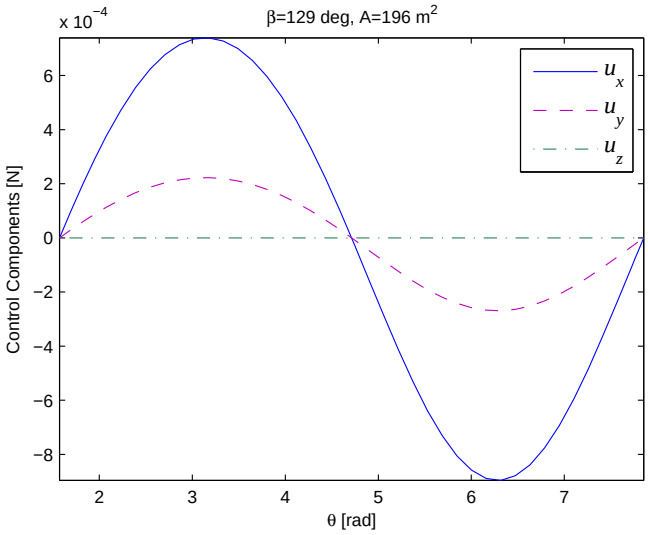

Figure 4.18: Control profile for maintaining a fixed position in the Hill frame.

required to compensate not only for the solar pressure and third body effects, but also for the constantly changing orbit of the asteroid.

The aim of the control law is to match the relative orbital parameters to those determined by the Funnel orbits, using as feedback the measured position and velocity of the spacecraft relative to the NEO since these values are needed for the tracking and deviation the asteroid. Our initial approach was to use the proximity-quotient, or Q-law, originally developed by Petropoulos [38] for the restricted two-body problem. The Q-law is based on a Lyapunov feedback control law, and calculates the optimal thrust angles based on the proximity to the target orbit (i.e. the difference in the static Keplerian parameters) and the current location of the spacecraft on the orbit (i.e. true anomaly).

$$Q = \sum_{\delta \mathbf{k}} W_k \left(\frac{k_i - k_T}{\dot{k}(\alpha_{in_{max}}, \alpha_{out_{max}}, \nu_{max})} \right)^2 \rightarrow \min(\dot{Q}) \tag{4.29}$$

where $\dot{k}$ is given by the Gauss equations, setting the thrust angles and orbital location $\alpha_{in} = \alpha_{in_{max}}, \alpha_{out} = \alpha_{out_{max}}, \nu = \nu_{max}$ that give the maximum rate of change for each element a, e, i, Ω and ω. The Q-law was developed to provide a first-guess solution for transfers between orbits, not point-to-point, so the mean anomaly M (or true anomaly ν) was left as a free variable. The equations were updated to include the $\dot{M}$ term, and account for SRP and third body effects in the Gauss equations $\dot{\mathbf{k}}$ required for this test case.

However, there were a number of issues that arose: the first was due to the high degree of accuracy need to maintain the funnel orbits. The difference in Keplerian between the NEO and the spacecraft are on the order of 10^{-7}, and need to remain constant even as the NEO deviates. This resulted in a lot of 'chatter' (over-shooting) around the target orbital elements, due to strong dependance on the time step δt and the magnitude of the control (which employed on-off shooting). Even at very small time steps, the magnitude of the over-shooting

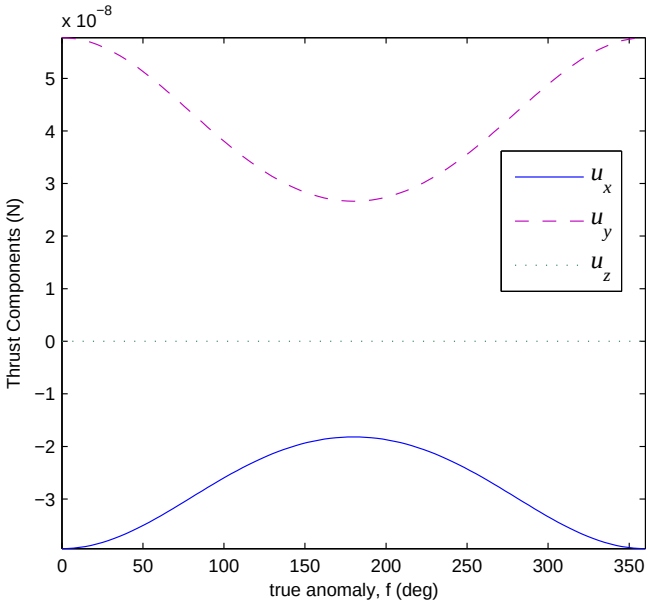

Figure 4.19: Control profile for orbit maintenance for ($A = 196$ m^2, $\beta = 139°$) following the motion of the AEP.

was too large for the system requirements. The effects of the perturbations are also relatively large, on the scale of mN in the radial direction (see Fig. 4.26) and need to be compensated for on a continuous basis.

Therefore, an alternative approach was developed to deal with these mission-specific limitations. The first was to switch from minimizing only with respect to the thrust angles, to minimizing with respect to the components $[u_x, u_y, u_z]^T$, which has the benefit of finding the optimal magnitude for the thrust, as well as the required angles. We considered the new Q^* function,

$$Q^* = \sum_{j=1}^{6} W_j \left(\Delta k_{T,j} - \int_0^{\delta t} \frac{dk_j}{dt} dt \right)^2 \tag{4.30}$$

where $\Delta \mathbf{k}_T = (\mathbf{k}_i - \mathbf{k}_T)$ is the desired variation of the orbital parameters in the time interval δt. The function Q^* is then minimized with respect to the control components $[u_x, u_y, u_z]^T$ every δt units of time.

4.5.2.1 Least-squares solution

If we consider that over very small time steps, we can assume as first approximation that the orbital parameters in the Gauss equations are constant, than we can solve directly for control function,

$$\sum W_j \left(\Delta k_{T,j} - \frac{dk_j}{dt} \delta t \right)^2 \tag{4.31}$$

Inherently, if the desired change in the j^{th} element $(k_{i,j} - k_{T,j})$ is negative, than the rate of change is positive, and vice versa. As such, the control equation will

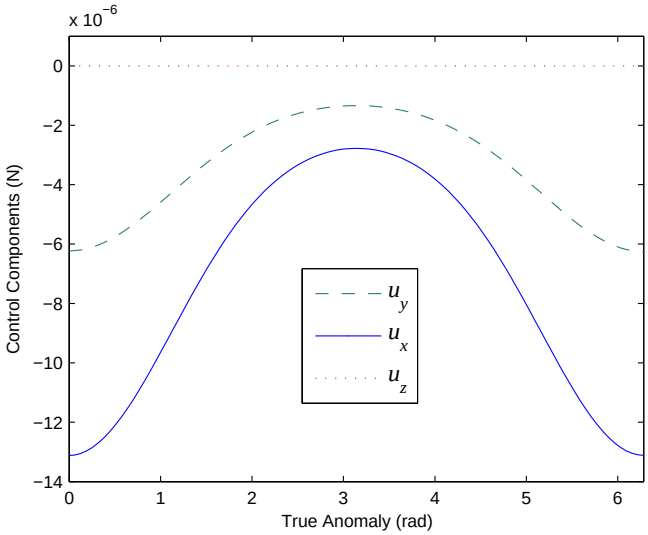

Figure 4.20: Control required to follow the AEP motion originally computed assuming a spherical asteroid (see Fig. 4.19) for a non-spherical asteroid.

always have a single minimum. Therefore there is no need to minimize the time derivative.

The solution for the control vector $\mathbf{u}_c$ is found by using an ordinary least squares fitting to the linear systems of equations, $\mathbf{A}\mathbf{u}_c = \mathbf{b}$. In our case, $\mathbf{A}$ is set equal to the Gauss equations [32],

$$\frac{d\mathbf{k}}{dt} = \mathbf{A} \cdot \mathbf{u}_c \tag{4.32}$$

$$\begin{bmatrix} \dot{a} \\ \dot{e} \\ \dot{i} \\ \dot{\Omega} \\ \dot{\omega} \\ \dot{M}^* \end{bmatrix} = \begin{bmatrix} \frac{2a^2 e \sin\nu}{h} & \frac{2a^2 p}{hr} & 0 \\ \frac{p\sin\nu}{h} & \frac{(p+r)\cos\nu + re}{h} & 0 \\ 0 & 0 & \frac{r\cos\theta}{h} \\ 0 & 0 & \frac{r\sin\theta}{h\sin i} \\ -\frac{p\cos\nu}{he} & \frac{(p+r)\sin\nu}{he} & -\frac{r\sin\theta\cos i}{h\sin i} \\ \frac{p\cos\nu - 2re}{e\sqrt{a\mu}} & -\frac{(p+r)\sin\nu}{e\sqrt{a\mu}} & 0 \end{bmatrix} \begin{bmatrix} u_x \\ u_y \\ u_z \end{bmatrix} \tag{4.33}$$

where $[u_x,\, u_y,\, u_z]^T$ are the components of the disturbing acceleration in the radial, transversal and normal directions respectively. The actual Gauss equation for dM/dt also includes a term for the mean motion n to account for the rotation around the Sun. In this case however, we do not want the control to compensate for the nominal motion of the orbit, just those induced by the perturbations and deviation of the asteroid. The mean motion is added to M^* after each iteration of the simulation control loop, where $M_i = M^* + n_{sc}\delta t$ (since the nominal rate of the change of the mean anomaly is linear).

The matrix $\mathbf{b}$ is solved by,

$$\mathbf{b} = \frac{\mathbf{k}_T - \mathbf{k}_i}{\delta t} - \mathbf{A}(\mathbf{u}_{pert}) \tag{4.34}$$

Again, this is equivalent to minimizing the quadratic function

$$\sum W_j(\Delta k_j - \Delta k_{T,j})^2$$

where Δk_j is the change of the j^{th} orbital element over time δt achieved with Gauss, and $\Delta k_{T,j}$ is the desired change.

An integration approach can also be used with the same control function Q^* in (4.30) which numerically integrates the Gauss equations to determine $\Delta k_{i,j}$.

$$\Delta k_{i,j} = \int_0^{\delta t} \frac{dk_j}{dt} dt \tag{4.35}$$

The least-squares approach provides a computationally faster solution (for the same time step) but is less accurate, especially over larger time steps.

4.5.2.2 Perturbations

The solar radiation pressure (SRP) must be accounted for within the control law for each surface area exposed to either the Sun or the focused beam.

For the fixed mirror configuration in Fig. 4.21a, this includes: the primary reflector (M_1), the secondary reflector (M_2), the laser (L), the directional mirror (M_3), and the solar panels. The spacecraft body and radiators are both blocked by the primary mirror.

The force from the solar radiation pressure on the primary reflector is given by,

$$\mathbf{F}_1 = 2P_r A_{\text{M}_1} \sigma_1 \cdot \hat{\mathbf{r}}_{\odot/s} \tag{4.36}$$

where σ is the coefficient of reflectivity of the surface, A_{M_1} is the illuminated surface area perpendicular to the Sun (i.e. the area of the aperture), and P_r is the solar power at distance r_{sc} from the Sun, given in (4.13).

The secondary reflector is exposed to both the direct sunlight (on the 'back' of the mirror), and the focused light from the primary reflector.

$$\mathbf{F}_2 = (2P_r \sigma_2 A_{\text{M}_2} - F_1 \sigma_2) \cdot \hat{\mathbf{r}}_{\odot/s} \tag{4.37}$$

In order to help balance the forces on the mirror, the coefficient of reflectivity on the back is the set the same as the front, meaning that both sides are equally reflective.

The focused beam from the second mirror is fed directly into the laser assembly,

$$\mathbf{F}_{\text{L}} = \left(\tfrac{1}{2} F_1 \sigma_2\right) \sigma_{\text{L}} \cdot \hat{\mathbf{r}}_{\odot/s} \tag{4.38}$$

The output of the laser is then directed onto the asteroid by means of a small directional mirror,

$$\mathbf{F}_3 = \eta_{\text{L}} F_{\text{L}} \sigma_4 \cos^2 \phi \cdot \hat{\mathbf{n}} \tag{4.39}$$

where η_{L} is the efficiency of the laser, here set to 18%.

Lastly, the pressure on the solar panels powering the spacecraft must be accounted for,

$$\mathbf{F}_{sp} = P_r A_{sp} \sigma_{sp} \cdot \hat{\mathbf{r}}_{\odot/s} \tag{4.40}$$

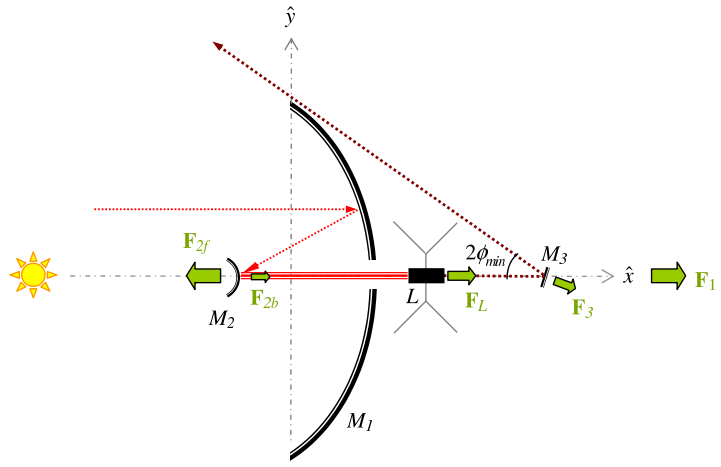

(a)

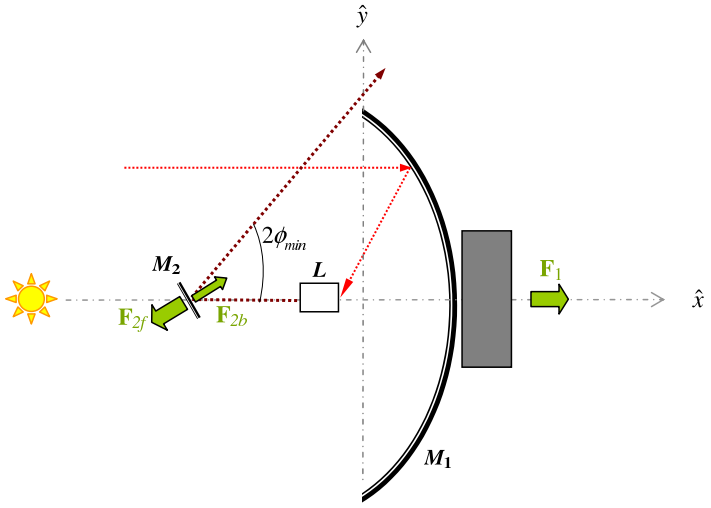

(b)

Figure 4.21: Vectors of solar radiation pressure on two fixed mirror configurations.

The total acceleration on the spacecraft due to SRP is then,

$$\mathbf{u}_{srp} = \frac{\mathbf{F}_1 + \mathbf{F}_2 + \mathbf{F}_L + \mathbf{F}_3 + \mathbf{F}_{sp}}{m_{sc}} \tag{4.41}$$

The configuration in Fig. 4.21b was originally used with the lens design, however could easily be used with a laser instead. The method for determining the solar radiation forces is the same as above, accounting for the primary mirror $\mathbf{F}_{M_1}$, the directional mirror ($\mathbf{F}_{M_{2f}} + \mathbf{F}_{M_{2b}}$), and the laser $\mathbf{F}_L$ plus any solar panels $\mathbf{F}_{sp}$.

The equations for the solar pressure given in (4.36)–(4.40) can be rewritten in terms of the orbital elements of the formation, and the orbital element differences $\delta\mathbf{k}$ compared with the asteroid. All the equations are relative to the $\mathcal{S}$ Hill frame.

$$\begin{aligned}\cos^2\phi = \frac{1}{2\delta r}\Big(&\delta r + r_{sc} - r_A\big(\cos\delta\Omega\cos(\delta\theta-\theta)\cos\theta \\ &- \cos(\delta i - i)\cos\theta\sin\delta\Omega\sin(\delta\theta-\theta) \\ &- \cos i\cos(\delta\theta-\theta)\sin\delta\Omega\sin\theta - \varpi\sin(\delta\theta-\theta)\sin\theta\big)\Big)\end{aligned} \tag{4.42}$$

where ϕ is the angle of reflection from the optical axis of the mirror (normal to the surface), and $\theta = \nu + \omega$ is the true latitude. For the two-mirror case (Fig. 4.21b), the angle would be rotated by π around the $z^{\mathcal{S}}$-axis.

The unit vector $\hat{\mathbf{n}}$ gives the direction of the net force due to the SRP on the directional mirror M_3,

$$\hat{\mathbf{n}} = \frac{\mathbf{n}_3}{\|\mathbf{n}_3\|} \tag{4.43}$$

$$\mathbf{n}_3 = \begin{bmatrix} -r_{\mathrm{A}}\left(\cos(\delta\theta-\theta)\sin\delta\Omega\sin i + \varpi\sin(\delta\theta-\theta)\right)\left(\sqrt{\frac{2\Gamma}{\delta r}} + 2\left(r_{sc} + r_{\mathrm{A}}\varrho\cos\theta + r_{\mathrm{A}}\zeta\sin\theta\right)\right) \\ r_{\mathrm{A}}\left(\cos i\cos(\delta\theta-\theta)\cos\theta\sin\delta\Omega \;+ \xi\cos\theta\sin(\delta\theta-\theta) - \varrho\sin\theta\right) \\ -\sqrt{\frac{\Gamma}{2\,\delta r}}\left(r_{sc} + r_{\mathrm{A}}\varrho\cos\theta + r_{\mathrm{A}}\zeta\sin\theta\right) \end{bmatrix}^{\mathcal{S}} \tag{4.44}$$

where ϖ, ξ, ϱ, ζ are defined in (4.2), and

$$\begin{aligned}\Gamma = \delta r + r_{sc} - r_{\mathrm{A}}\Big(&\cos\delta\Omega\cos(\delta\theta-\theta)\cos\theta \\ &+ \cos(\delta i - i)\cos\theta\sin\delta\Omega\sin(\delta\theta-\theta) + \zeta\sin\theta\Big)\end{aligned} \tag{4.45}$$

Since the effects of the asteroid's gravity field outside the imposed limiting sphere are relatively linear [14], and much less compared to those due the solar radiation pressure, the asteroid is treated, as a first approximation, as a point mass with $\mu_{\mathrm{A}} = 1.8016E\text{-}9$ km^3/s^2. The acceleration due to a third body is given by [39],

$$\ddot{\mathbf{r}}_{\odot/s} = -\frac{\mu_\odot \mathbf{r}_{\odot/s}}{r^3_{\odot/s}} + \mu_A\left(\frac{\mathbf{r}_{sc/A}}{r^3_{sc/A}} - \frac{\mathbf{r}_{\odot/A}}{r^3_{\odot/A}}\right) \tag{4.46}$$

assuming $m_\odot \gg m_A \gg m_{sc}$. Adding the perturbing acceleration due to the

asteroid, the perturbing control vector becomes,

$$\mathbf{u}_{pert} = \begin{bmatrix} \dfrac{F_1 + F_2 + F_L + F_{sp}}{m_{sc}} + \dfrac{F_3}{m_{sc}}\hat{n}_x + \mu_{\text{A}}\left(\dfrac{\delta r_x}{|\delta r|^3} - \dfrac{r_{sc} + \delta r_x}{|r_A|^3}\right) \\ \dfrac{F_3}{m_{sc}}\hat{n}_y + \mu_{\text{A}}\left(\dfrac{\delta r_y}{|\delta r|^3} - \dfrac{\delta r_y}{|r_A|^3}\right) \\ \dfrac{F_3}{m_{sc}}\hat{n}_z + \mu_{\text{A}}\left(\dfrac{\delta r_z}{|\delta r|^3} - \dfrac{\delta r_z}{|r_A|^3}\right) \end{bmatrix}^{\mathcal{S}} \tag{4.47}$$

Figures 4.22–4.25 show the forces acting on the spacecraft due to the solar radiation pressure and third body effects from Apophis. Formation orbit $\delta\mathbf{k}_{5/1}$ from Table 4.2 was used as the representative case. The spacecraft mass was set to 2000 kg, with a 20 m diameter primary dish, with a focal length of 5 m, a 1 m secondary and tertiary mirrors, and solar arrays of dimensions 8×2 m.

4.5.2.3 Simulation

The individual steps of the simulation routine are described in Algorithm 1.

Simulations were run using the integration method control loop with time step $\delta t = 5$ s, using a five test orbits chosen out of the set of Pareto optimal Funnel solutions (see Table 4.2), and the least squares method for with times steps of $\delta t = [1, 10]$ s using formation orbit $\delta\mathbf{k}_{5/1}$. The thrust leg of the mission was started 13 April 2031 – 5 years before the first potential impact. The required thrust duration is 552.30 days to reach a deviation distance of 384400 km (equal to the Earth-Moon distance) in 2036.

Figure 4.28 shows the deviation of the orbital elements of the NEO during the thrusting segment. Figures 4.29–4.33 show the change in Keplerian elements, and the thrust profile for the integration method, while Figs. 4.34 and 4.35 use the least squares method.

Table 4.2: Test case formation orbits, $\delta\mathbf{k}$ parameters.

Spacecraft	δa	δe	δi	$\delta\Omega$	$\delta\omega$	δM
$\delta\mathbf{k}_{5/1}$	0	1.0000E-11	-6.6861E-9	-5.0000E-8	4.4815E-8	2.5043E-8
$\delta\mathbf{k}_{5/2}$	0	3.3323E-12	-3.7934E-9	-4.7308E-8	4.9561E-8	1.5711E-8
$\delta\mathbf{k}_{5/3}$	0	6.1028E-13	-1.3168E-8	-4.9986E-8	2.8846E-8	4.4166E-8
$\delta\mathbf{k}_{5/4}$	0	-8.5308E-13	-2.0467E-9	-2.4000E-8	3.0878E-8	9.9775E-9
$\delta\mathbf{k}_{5/5}$	0	-6.8000E-12	-1.4403E-9	-2.1705E-8	3.0000E-8	8.4145E-9

4.6 Discussion

This section presented two possible options for placing the mirrors in the proximity of Apophis avoiding plume impingement and occultation. The preliminary analysis of the dynamics, coupled with the optical characteristics, of the mirror suggests that for a direct imaging solution the mirror can be placed at a distance from the asteroid to minimise the difference between gravity attraction of the asteroid and solar pressure. In the specific case of Apophis, however, the

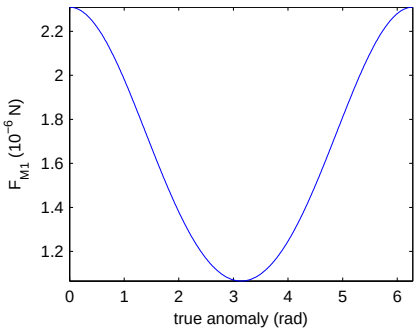

(a) Primary mirror.

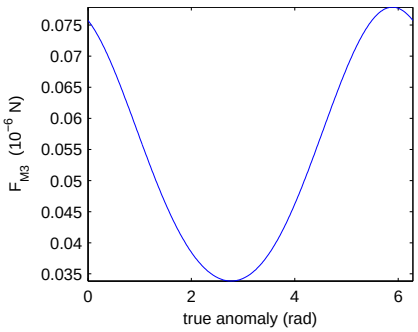

(b) Tertiary mirror.

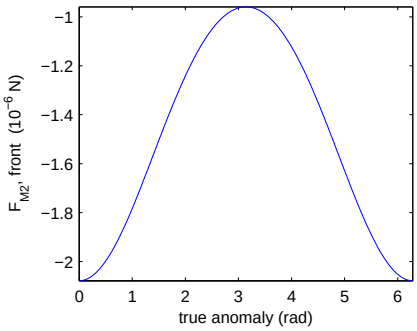

(c) Front of secondary mirror (facing primary).

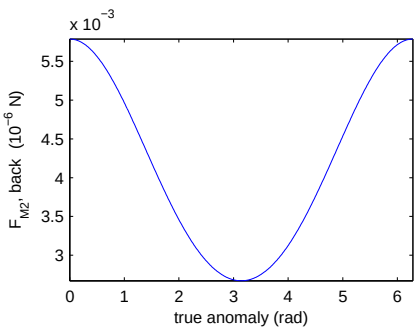

(d) Back of secondary mirror (facing Sun).

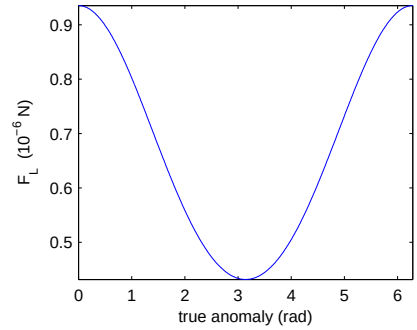

(e) Laser.

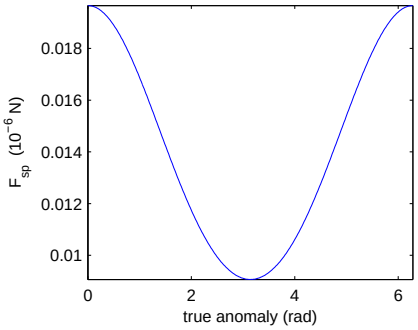

(f) Solar panels.

Figure 4.22: Force due to solar radiation pressure on the various surfaces of the spacecraft.

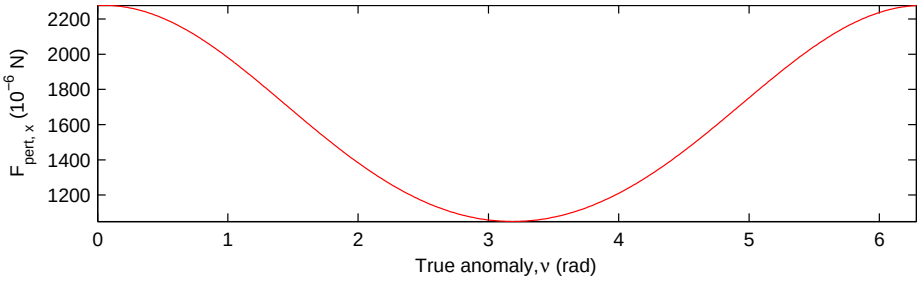

(a) Radial component.

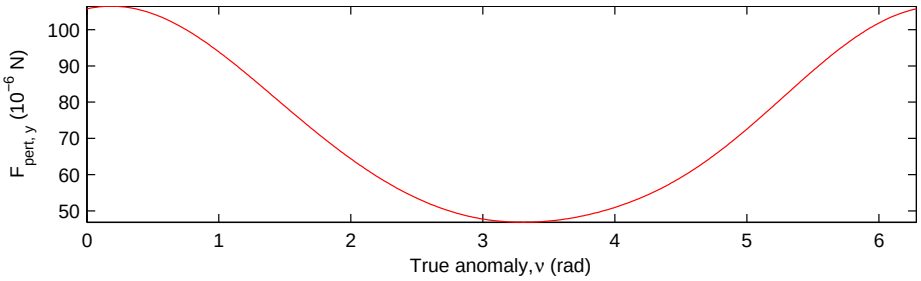

(b) Transverse component.

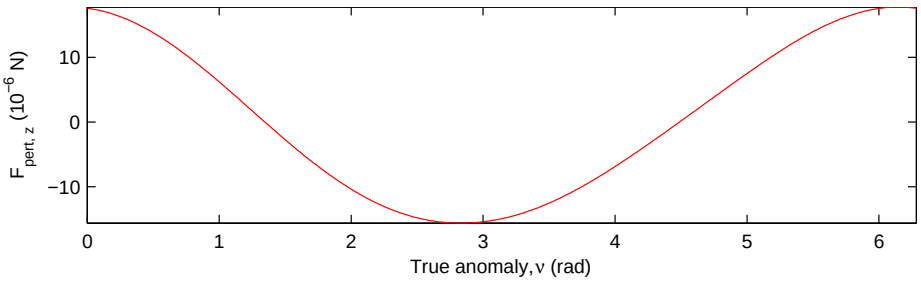

(c) Normal component.

Figure 4.23: Total force due to solar radiation pressure.

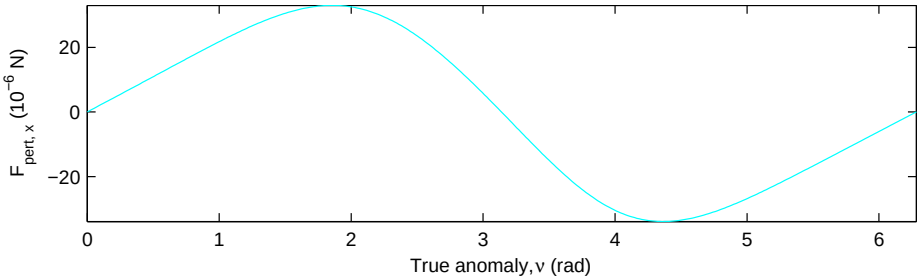

(a) Radial component.

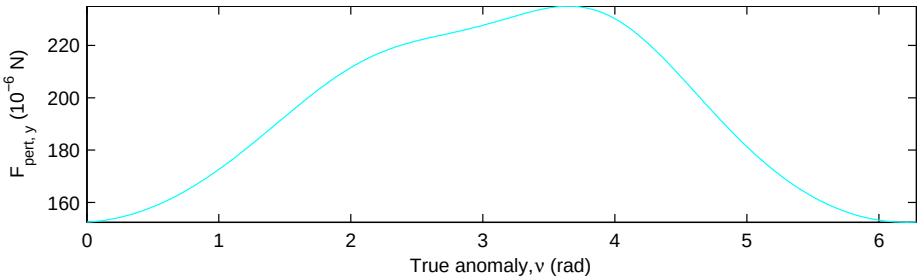

(b) Transverse component.

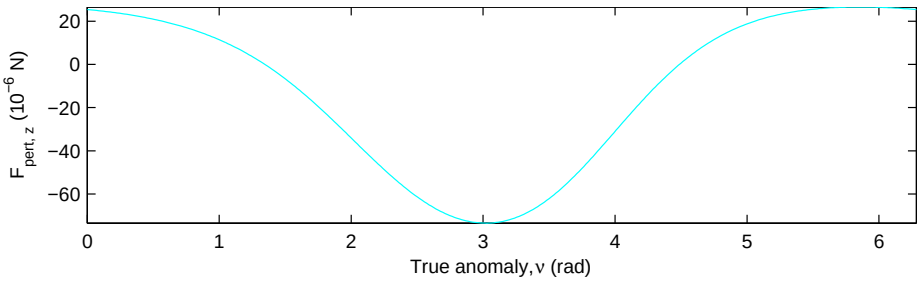

(c) Normal component.

Figure 4.24: Force due to third body effects from the NEO.

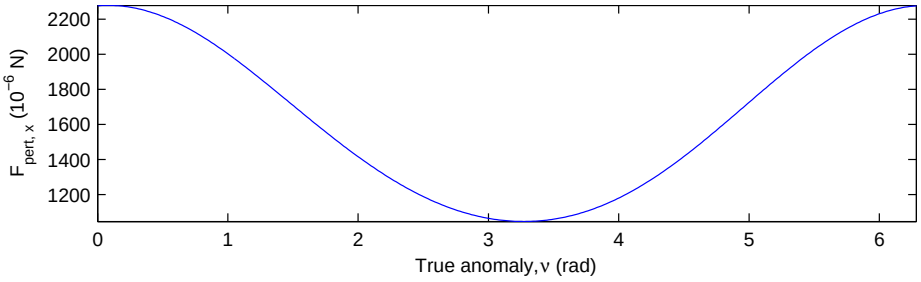

(a) Radial component.

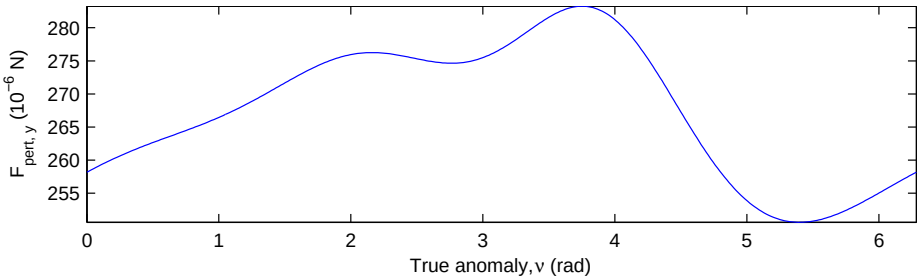

(b) Transverse component.

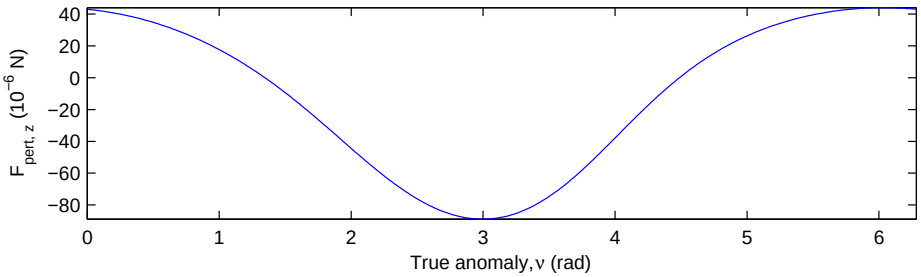

(c) Normal component.

Figure 4.25: Total perturbing force acting on the spacecraft.

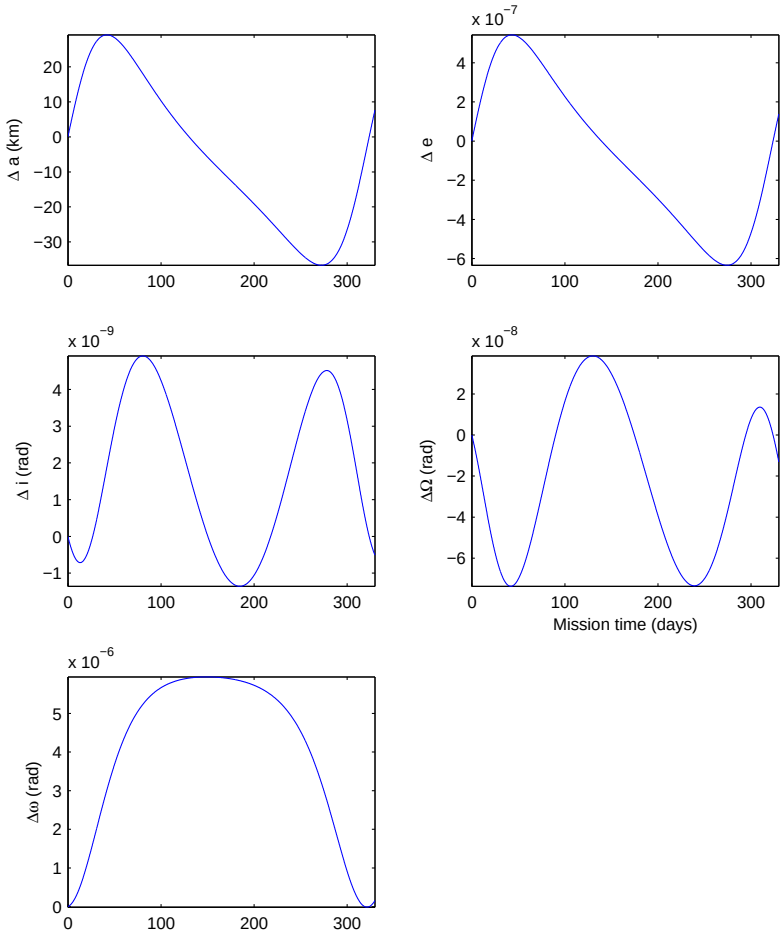

Figure 4.26: Effect of total perturbing acceleration on the spacecraft orbit parameters.

Algorithm 1 Feedback Control Simulation

1: **Identify starting conditions for spacecraft**:
   - number of spacecraft $n_{sc} = 20$
   - mass-in-orbit of each spacecraft $m_{sc} = 2000$ kg
   - aperture diameter, depth and illuminated surface area for the parabolic mirror $f_\ell = 5$ m (depth of 4.472 m), $d_{M_1} = 20$ m $\rightarrow A_{M_1} = 448.52$ m^2
   - directional mirror $d_{M_2} = 1$ m $\rightarrow A_{M_2} = 0.7853$ m^2

   The starting positions at t_0 relative to the asteroid are given in Table 4.2.
2: **Identify starting conditions for NEO Apophis**:
   - time and true anomaly at calculated MOID, $t_{\text{MOID}} = 13251.87$ MJD2000 (13 April 2036 08:52) and $\nu_{\text{MOID}} = 4.0747$ rad,
   - time when the spacecraft starts the deviation action (i.e. solar sublimation) $t_0 = t_{\text{MOID}} = 728.5$ days,
   - target deviation distance nominally set equal to the Earth-Moon distance $\Delta r_{dev_T} = 384401$ km,
   - initial mass of asteroid $m_{\text{A}} = 2.7E10$ kg,
   - initial Keplerian orbital parameters given in Table 4.1.
3: Initial target elements are set equal to initial starting position $\mathbf{k}_T = \mathbf{k}_i = \mathbf{k}_0$.
4: Determine optimal control vector $\mathbf{u}_c = [u_{c_r}, u_{c_t}, u_{c_h}]$ solving the linear system of equations $\mathbf{A}\mathbf{u}_c = \mathbf{b}$ given in (4.32)–(4.34) by the method of ordinary least squares fitting, given: $\mathbf{k}_i, \mathbf{k}_T, \delta\mathbf{k}, m_{A_i}$.
5: Propagate spacecraft forward by time step δt using Gauss equations with input $\mathbf{u} = \mathbf{u}_c + \mathbf{u}_{pert}$.
6: **Update** $\mathbf{k}_i$
7: Propagate asteroid forward by time step δt using Gauss equations with input $\mathbf{u} = \mathbf{u}_{dev}$.
8: **Update** $\mathbf{k}_{\text{A}}$, m_{A_i} and $\delta\mathbf{k}_i = \mathbf{k}_i - \mathbf{k}_{\text{A}}$.
9: Update target vector to reflect the deviated orbit of Apophis, $\mathbf{k}_T = \mathbf{k}_A + \delta\mathbf{k}_0$.
10: Calculate achieved deviation distance Δr_A.
11: **if** $\Delta r_A \geq \Delta r_{dev_T}$ **then**
12: **Termination**
13: **else**
14: *goto* Step 4
15: **end if**

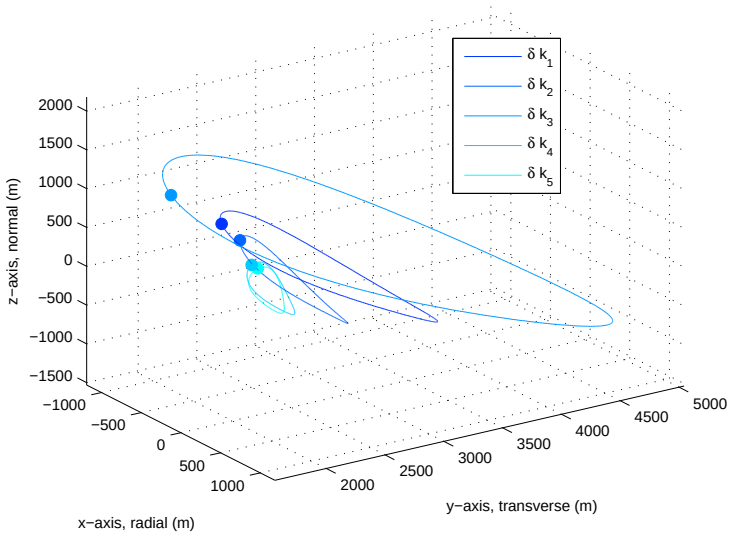

Figure 4.27: Formation orbits for test cases, shown in the Hill reference frame $\mathcal{A}$ relative to Apophis, located at (0,0).

equilibrium solutions are too close to the asteroid and for further away locations an active control is required. In this case a single mirror would require a higher level of control than a set of smaller mirrors.

Note that, unlike in the case of previous works on artificial equilibrium points [40, 41, 42], in this case there is a strict constraint on the pointing direction, furthermore the reflector does not act simply as a sail but by changing its shape can control the direction and magnitude of the resultant force. From the results in this section, we can also argue, that the existence of a fixed point were the forces are balancing for every point along the orbit is not a strict requirement. In fact, provided that the direction can be controlled at minimum cost, the distance of the mirror from the asteroid can vary, reaching its maximum at perihelion and its minimum at aphelion. In fact, though a longer distance would imply a lower concentration factor, the increase in power density due to the reduced distance from the Sun would compensate for the reduction in the concentration factor.

If the solar-pumped laser option is considered, instead, the mirror can be placed either at equilibrium points around the asteroid or on periodic formation orbits (funnel orbits). This second solution would imply a more complex thermal control system unless a new efficient solar-pumped laser is developed but would also allow the use of smaller mirrors. In this case we can envisage a further architecture for the formation with a primary (or master) spacecraft carrying the laser and a secondary (or slave) spacecraft serving as reflector (see Fig. 4.36). The master spacecraft would be leading the asteroid, complectly out of any plume impingement or occultation, while the slave spacecraft would trail the asteroid positioned at an equilibrium point at a distance from the asteroid.

For the control, more work is needed on minimizing the oscillations in the integration control. Due to the time limit of the study, only a short simulation could be run however a full simulation is necessary.

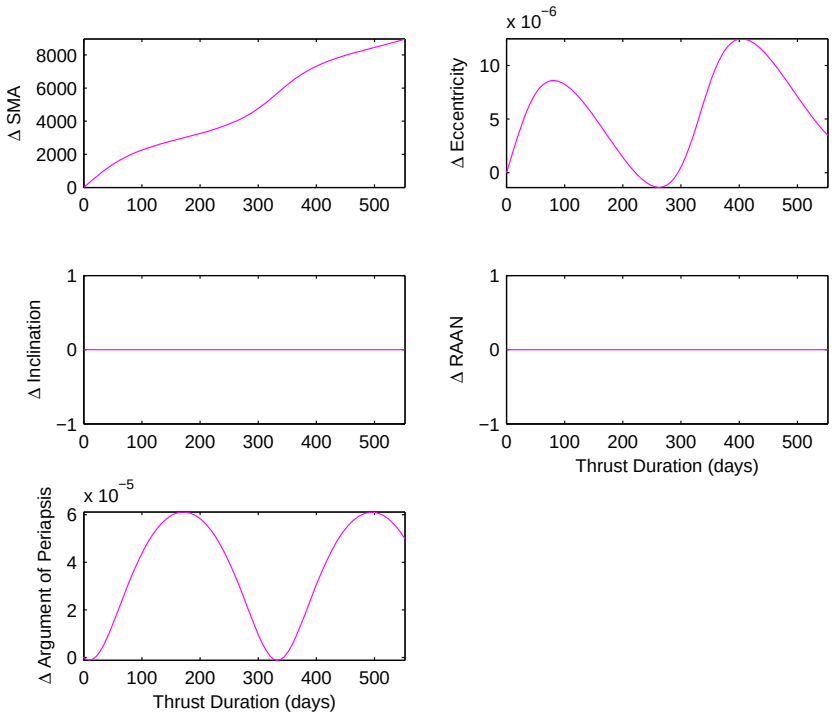

Figure 4.28: Deviation of Keplerian elements for Apophis, with a warning time of 5 years before the 2036 potential impact for a deviation distance of 384400 km in 2036.

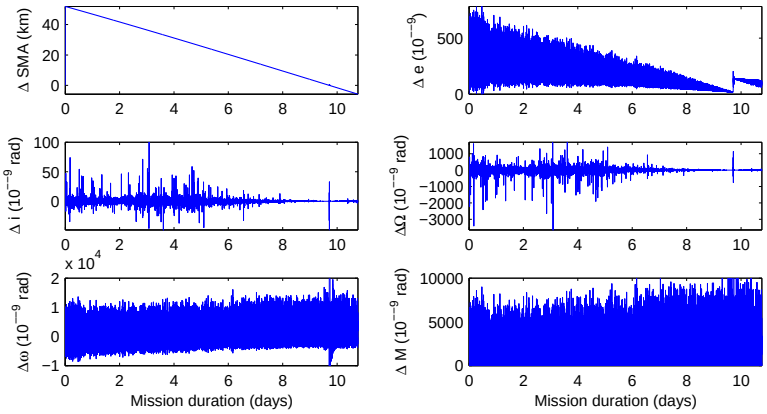

(a) Variations in the orbital element differences.

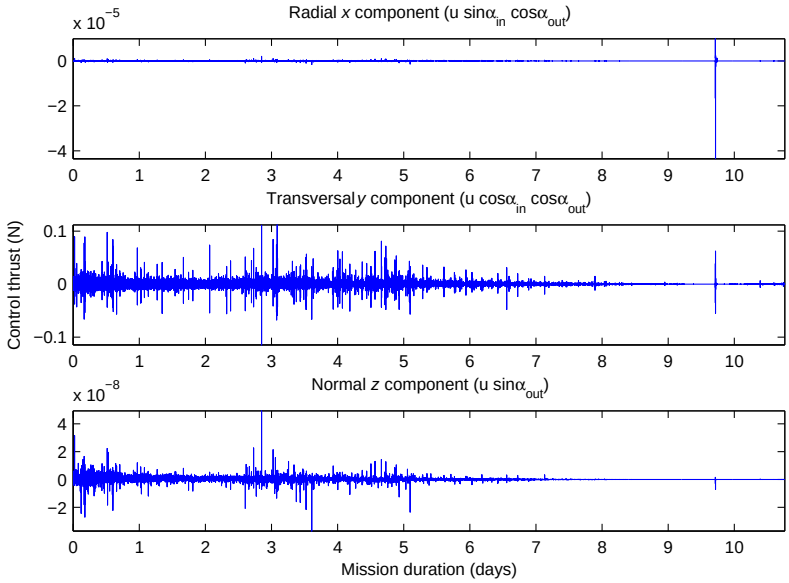

(b) Control thrust components.

Figure 4.29: Integration control law for spacecraft formation $\delta\mathbf{k}_{5/1}$ with triple fixed mirror configuration.

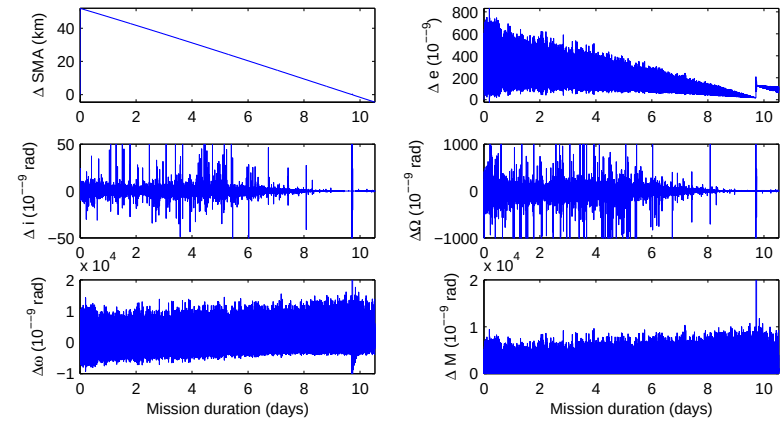

(a) Variations in the orbital element differences.

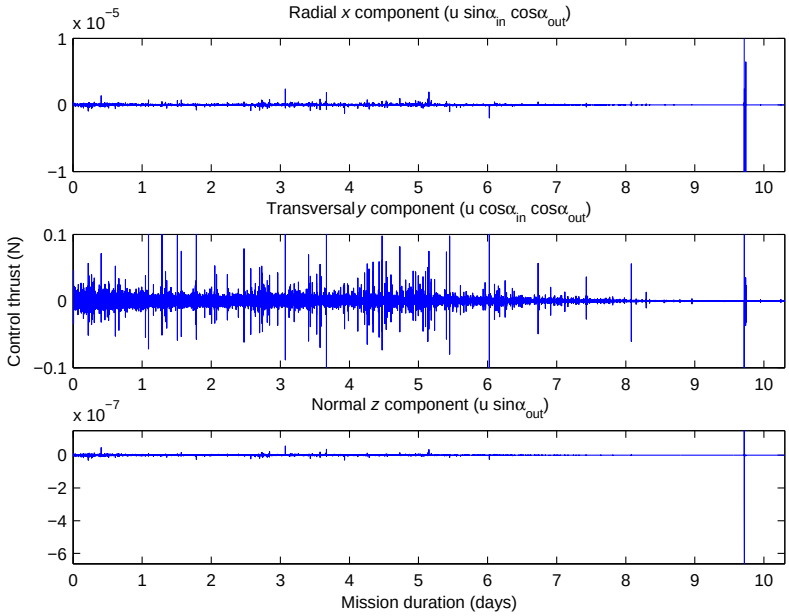

(b) Control thrust components.

Figure 4.30: Integration control law for spacecraft formation $\delta\mathbf{k}_{5/2}$ with triple fixed mirror configuration.

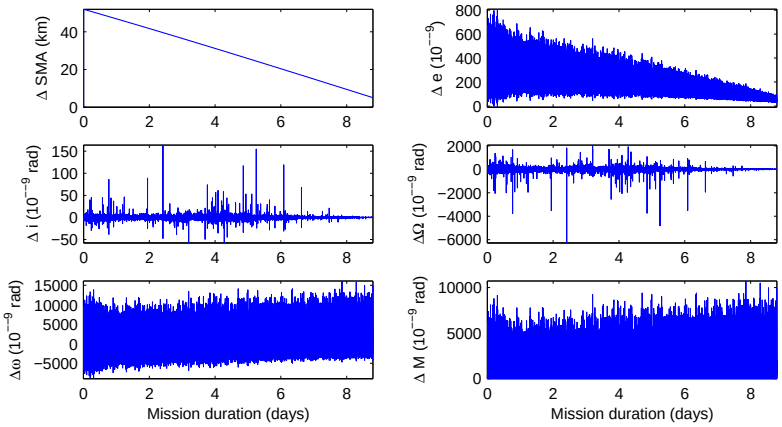

(a) Variations in the orbital element differences.

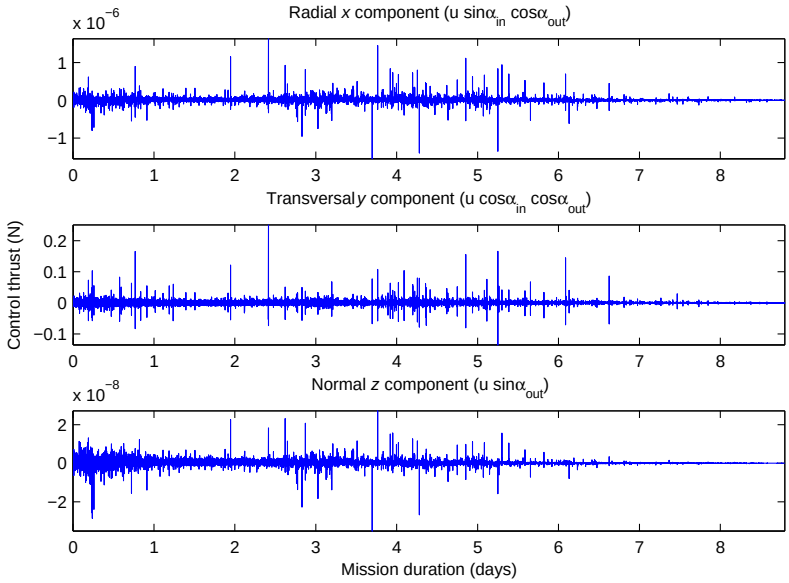

(b) Control thrust components.

Figure 4.31: Integration control law for spacecraft formation $\delta\mathbf{k}_{5/3}$ with triple fixed mirror configuration.

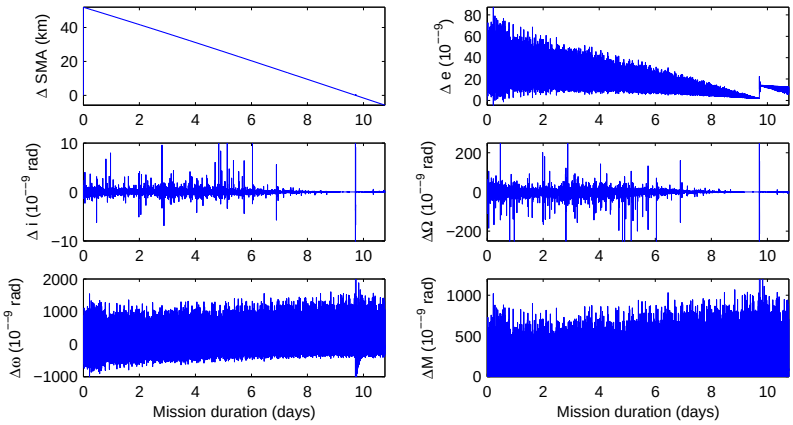

(a) Variations in the orbital element differences.

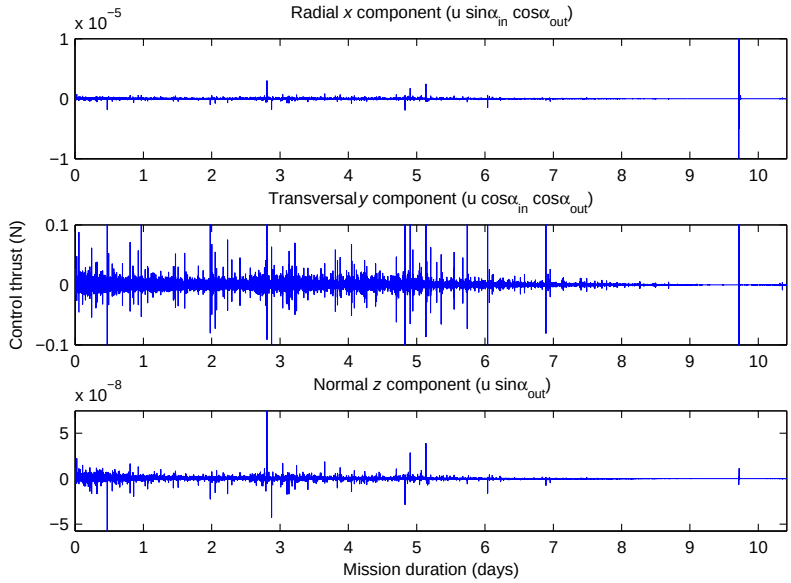

(b) Control thrust components.

Figure 4.32: Integration control law for spacecraft formation $\delta\mathbf{k}_{5/4}$ with triple fixed mirror configuration.

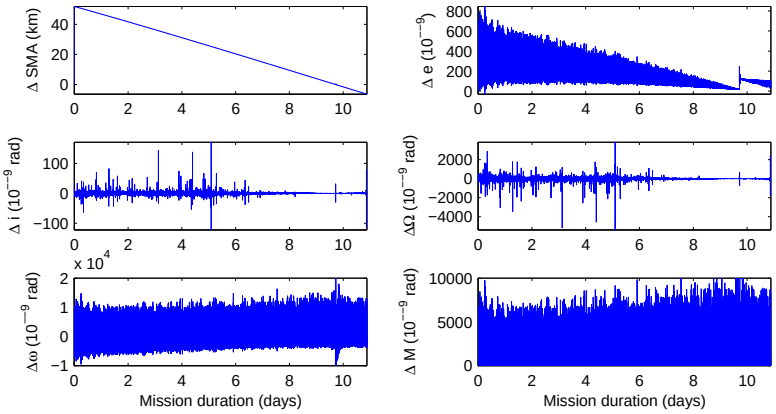

(a) Variations in the orbital element differences.

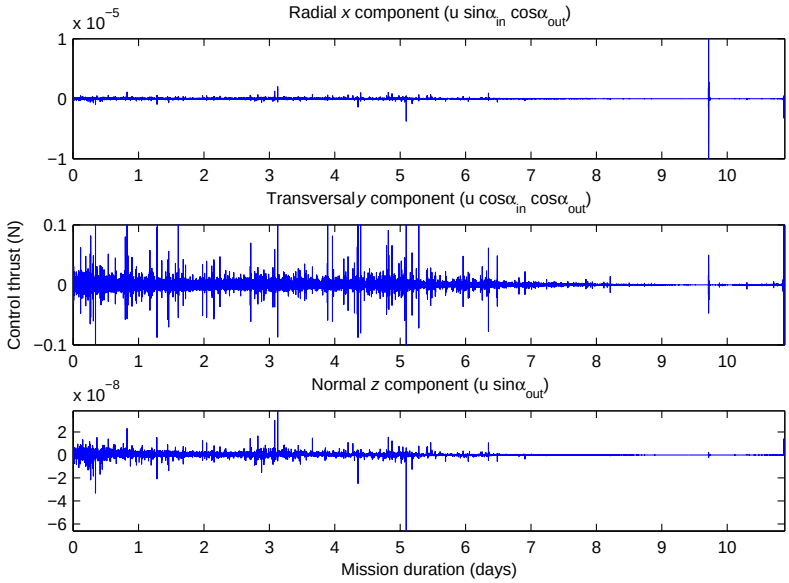

(b) Control thrust components.

Figure 4.33: Integration control law for spacecraft formation $\delta\mathbf{k}_{5/5}$ with triple fixed mirror configuration.

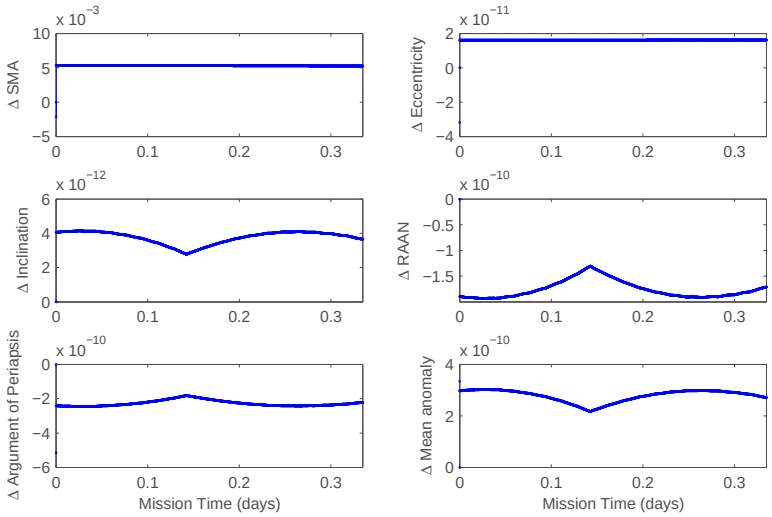

(a) Variations in the orbital element differences.

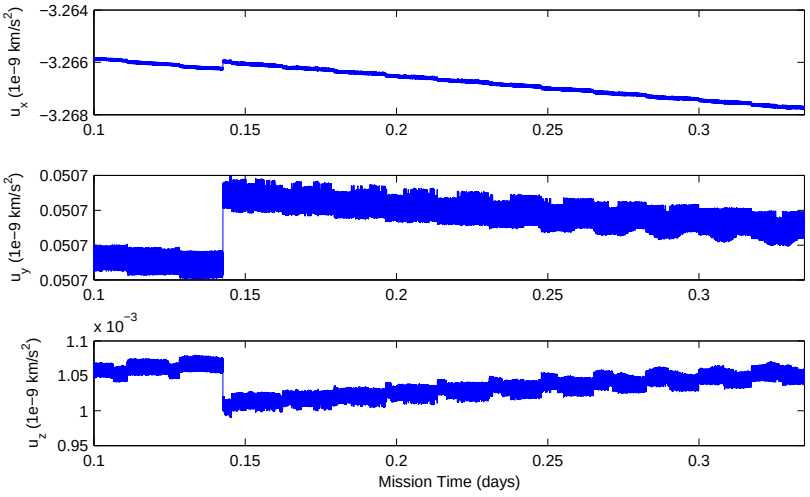

(b) Control thrust components.

Figure 4.34: Least-squared control law with $\delta t = 1$ s for spacecraft formation $\delta\mathbf{k}_{5/1}$ with the dual fixed mirror configuration.

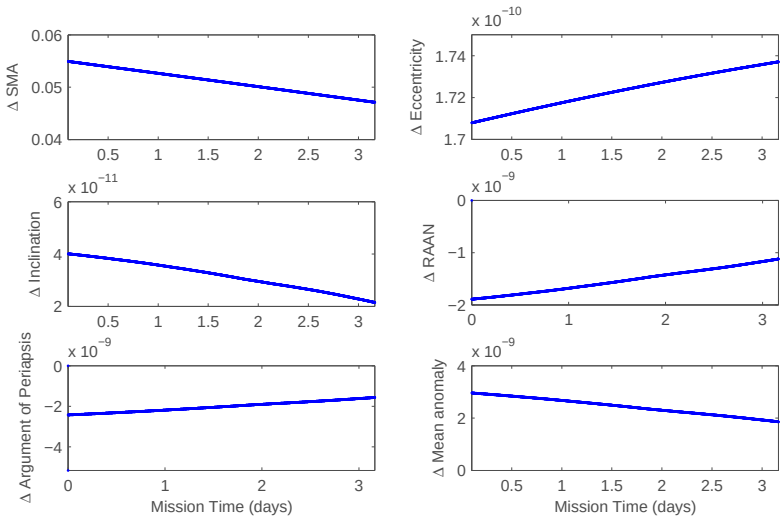

(a) Variations in the orbital element differences.

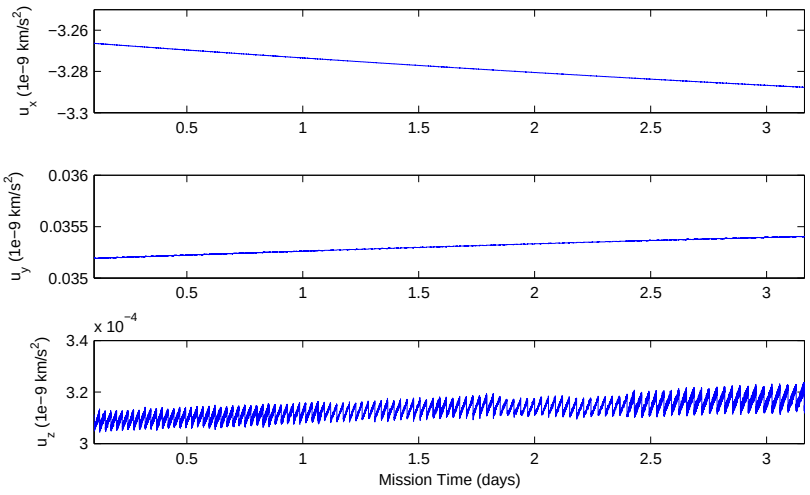

(b) Control thrust components.

Figure 4.35: Least-squared control law with $\delta t = 10$ s for spacecraft formation $\delta\mathbf{k}_{5/1}$ with the dual fixed mirror configuration.

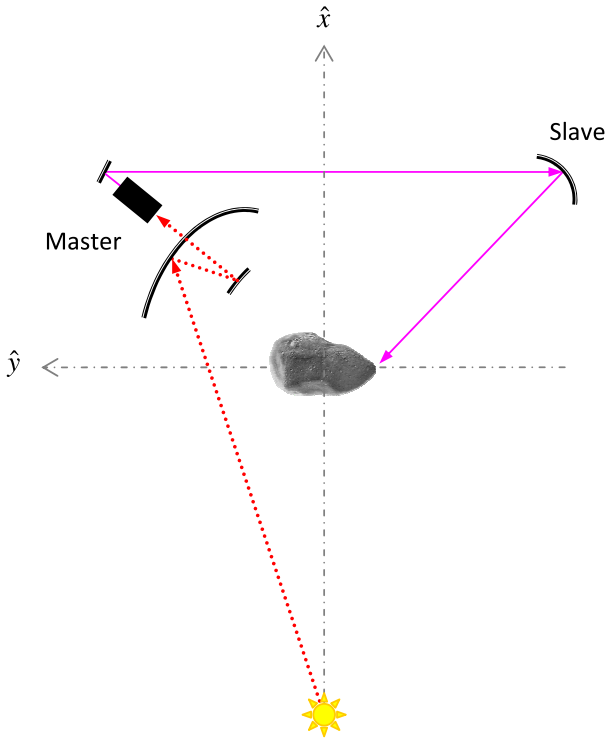

Figure 4.36: Dual-bee configuration with a master bee source and a slave bee reflector.

However, it is worth to underline that the control authority required to maintain the orbit under the effects of the inhomogeneous gravity field of the asteroid, solar pressure and deflection of the orbit, in both the AEP and the funnel case is extremely small and can be provided, over a long time, with a FEEP system or an ion engine for attitude control at minimum power and propellant cost.

5 Attitude Dynamics

5.1 Introduction

The following section details a preliminary analysis of the attitude dynamics of the spacecraft, in the case of the dual and triple mirror configuration. The aim of this section is to estimate the required control authority (magnitude of the control torque) to maintain the attitude of the spacecraft.

The analysis is limited to the fixed mirror case in its various configurations. The single mirror case is far more complicated due to the asymmetric shape of the mirror and to the variable shape. The attitude dynamics of the single mirror solution is therefore left to future developments of this research.

5.2 Spacecraft attitude

The directional cosine matrix $\mathbf{D}$, quaternions $\mathbf{q}$ and Euler angles $[\mathbf{e}, \psi]$ can all be used interchangeably for conversion from one coordinate system to another [43].

$$q_1 = e_1 \sin(\tfrac{1}{2}\psi) = \frac{1}{4q_4}(D_{23} - D_{32}) \tag{5.1a}$$

$$q_2 = e_2 \sin(\tfrac{1}{2}\psi) = \frac{1}{4q_4}(D_{31} - D_{13}) \tag{5.1b}$$

$$q_3 = e_3 \sin(\tfrac{1}{2}\psi) = \frac{1}{4q_4}(D_{12} - D_{21}) \tag{5.1c}$$

$$q_4 = \cos(\tfrac{1}{2}\psi) = \pm\tfrac{1}{2}\sqrt{1 + D_{11} + D_{22} + D_{33}} \tag{5.1d}$$

In particular, we are interested in the rotational matrix $\mathbf{D}_{\mathcal{O}/\mathcal{S}}$ that translates a vector from the heliocentric inertial reference frame $\mathcal{O}$ to the spacecraft-centric reference frame $\mathcal{S}$. The body reference frame is defined, nominally, in the local radial-transverse-normal frame originating from the centre of mass of the spacecraft.

$$\mathbf{D}_{\mathcal{O}/\mathcal{B}} = \begin{bmatrix} r_x/r & (\mathbf{h} \wedge \mathbf{r})_x/\|(\mathbf{h} \wedge \mathbf{r})\| & h_x/h \\ r_y/r & (\mathbf{h} \wedge \mathbf{r})_y/\|(\mathbf{h} \wedge \mathbf{r})\| & h_y/h \\ r_z/r & (\mathbf{h} \wedge \mathbf{r})_z/\|(\mathbf{h} \wedge \mathbf{r})\| & h_z/h \end{bmatrix}^{-1} \tag{5.2}$$

where $\mathbf{r} = \mathbf{r}_{\odot/sc}$, $\mathbf{v} = \mathbf{v}_{\odot/sc}$ are position and velocity vectors from the Sun to a given spacecraft in the inertial $\mathcal{O}$ frame, and the angular momentum $\mathbf{h} = \mathbf{r}_{\odot/sc} \wedge \mathbf{v}_{\odot/sc}$.

Given the pointing vector from the spacecraft to the NEO $\delta\mathbf{r}_{sc/A}$ in the body reference frame, the attitude quaternions can be determined since the reflector must always be inline with the Sun, and the normal of the directional mirror surface must bisect the Sun-spacecraft angle (given by $\mathbf{r}_{sc}$, $\delta\mathbf{r}_{sc}$). Figures 5.1–5.5 shows the quaternions over one orbit for each spacecraft in Table 4.2.

5.3 Torque

The torque τ for any body is given by the applied force $\mathbf{F}$, and the distance l from the centre of mass, $\tau_i = l_i \wedge \mathbf{F}_i$.

The force in this analysis is due primarily to the solar radiation, shown in Fig. 5.6. The only disturbing, or non-symmetrical force acting on the system is the directional mirror, and possibly the solar arrays depending on the arrangement. The distance between the directional mirror and the primary mirror is dictated by geometry. The directional mirror must be far enough away from the primary that can see the NEO at all times during the orbit. The maximum and minimum angle of reflection ϕ was computed for each formation orbit, and used to compute the distance l_{M_3}. The angles of reflection are listed in Table 5.1.

The torque was computed assuming a direction mirror with a diameter of 1 m. The solar arrays were estimated at 2×8 m, with the short end aligned with the axis.

Table 5.1: Maximum and minimum values of the angle of reflection ϕ on the directional mirror.

	$\min_{\nu}(\phi)$	$\max_{\nu}(\phi)$
$\delta\mathbf{k}_{5/1}$	0.666282677717407 rad	0.906417646233451 rad
$\delta\mathbf{k}_{5/2}$	0.701638085152963	0.869206003684102
$\delta\mathbf{k}_{5/3}$	0.612704122366686	0.978286440727879
$\delta\mathbf{k}_{5/4}$	0.72791899785277	0.842870660468973
$\delta\mathbf{k}_{5/5}$	0.736191106671985	0.834527096418112

Figures 5.7–5.11 show the torque produced by the direction mirror (e.g. M_3 in the tri-mirror system) over one orbit. Figure 5.12 show the effects of a non-symmetrical positioning of the solar arrays, for example only positioned above and below the primary mirror along either the y- or z-axis.

5.4 Discussion

The preceding showed a preliminary investigation into the attitude requirements of the spacecraft in the formation. The quaternions were calculated, along with the torque due to SRP. Future work will include determining the angular velocity ω and moments of inertia for the spacecraft, to complete the dynamical model of the Mirror Bees and develop a control strategy.

In this study, on the solar radiation pressure was considered in calculating unwanted torque on the spacecraft assembly. Other sources of disturbance, such as the gravity gradient, will need to be included in future work. In addition, the spacecraft is not a rigid body, as assumed here, but due to the size will be

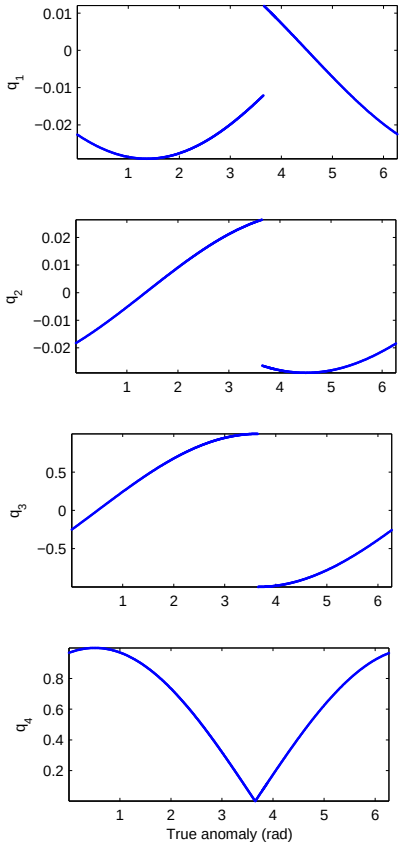

Figure 5.1: Quaternions for $\delta\mathbf{k}_{5/1}$

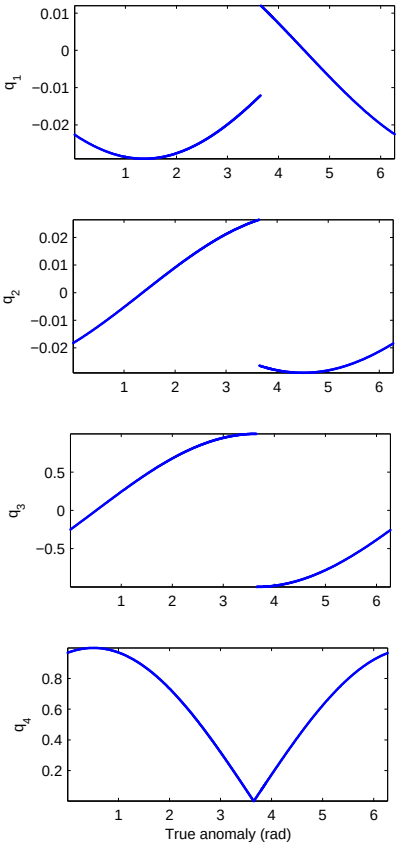

Figure 5.2: Quaternions for $\delta\mathbf{k}_{5/2}$

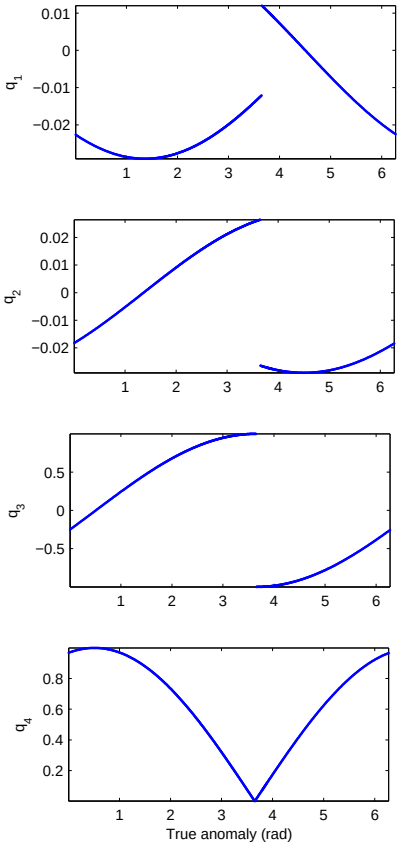

Figure 5.3: Quaternions for $\delta\mathbf{k}_{5/3}$

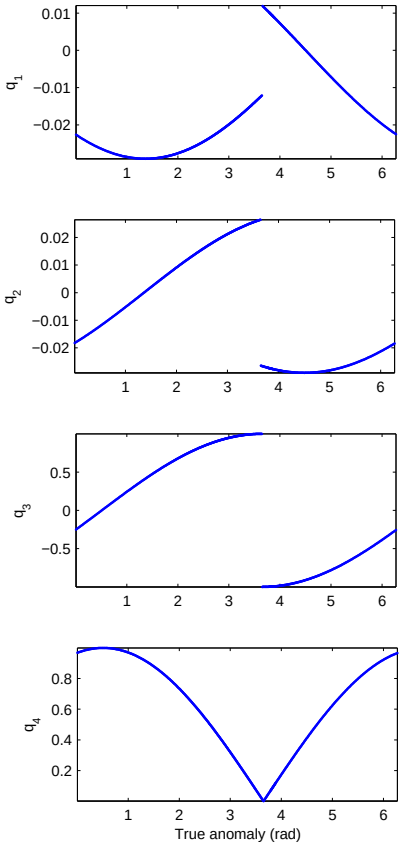

Figure 5.4: Quaternions for $\delta\mathbf{k}_{5/4}$

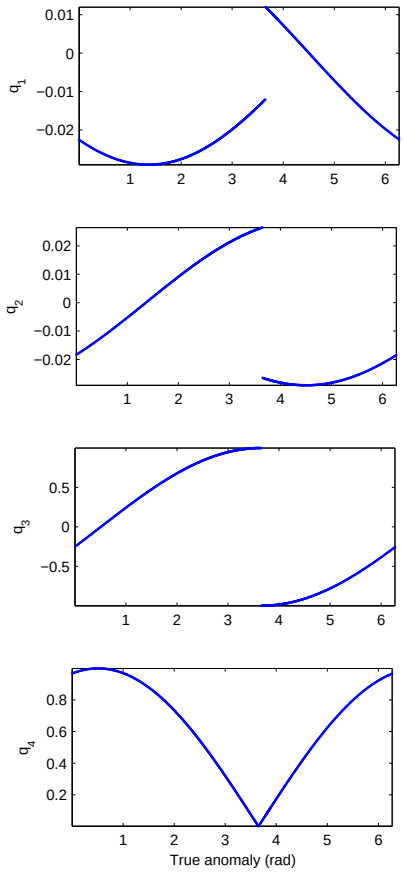

Figure 5.5: Quaternions for $\delta\mathbf{k}_{5/5}$

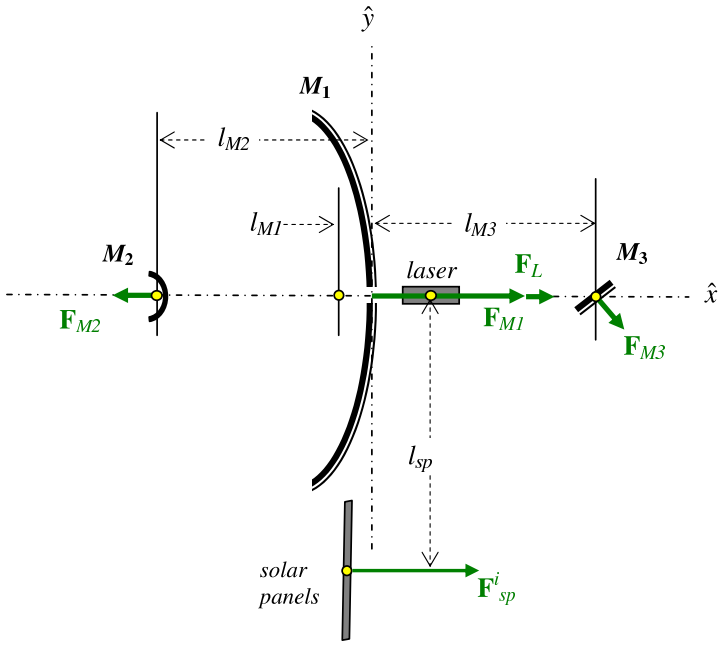

(a) Dual mirror system, with either a collimating lens or laser between M_1 and M_2.

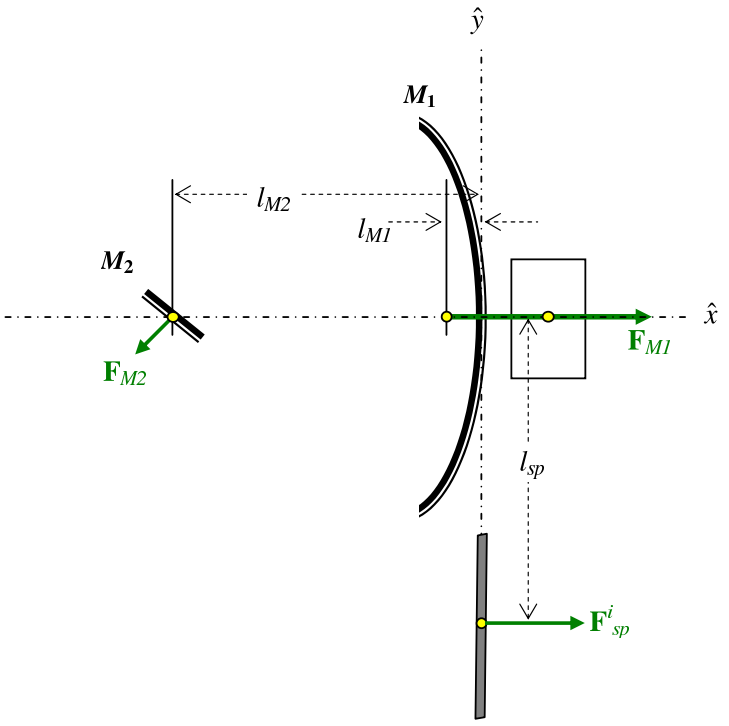

(b) Tri-mirror system with laser behind primary mirror.

Figure 5.6: Conceptual force diagram on the spacecraft including the mirror assembly, spacecraft body and solar panels. Note: only one solar panel is shown in the diagram, however the solar panel arrangement is symmetrical about the $\pm y$, $\pm z$ axes to balance the moments of inertia, and is composed of either 2 or 4 panels.

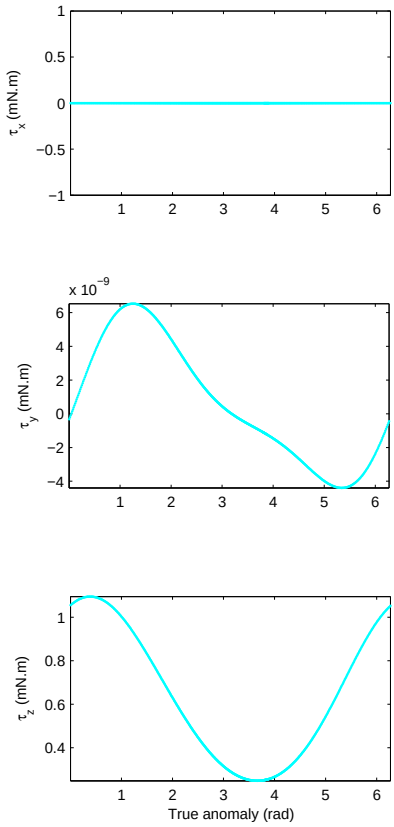

Figure 5.7: Torque produced by the directional mirror for $\delta\mathbf{k}_{5/1}$

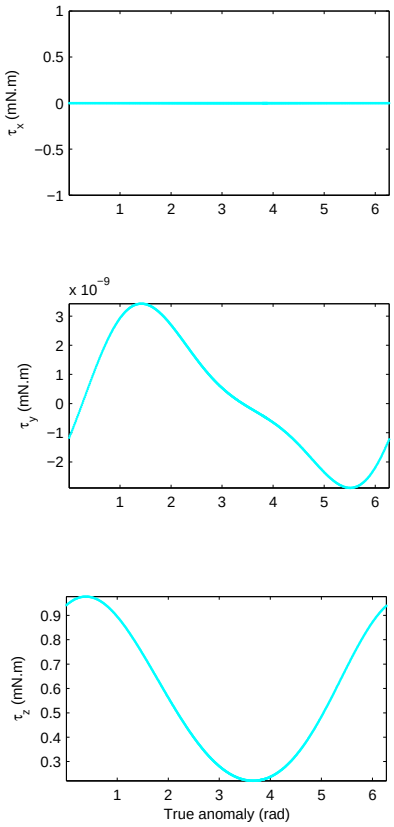

Figure 5.8: Torque produced by the directional mirror for $\delta\mathbf{k}_{5/2}$

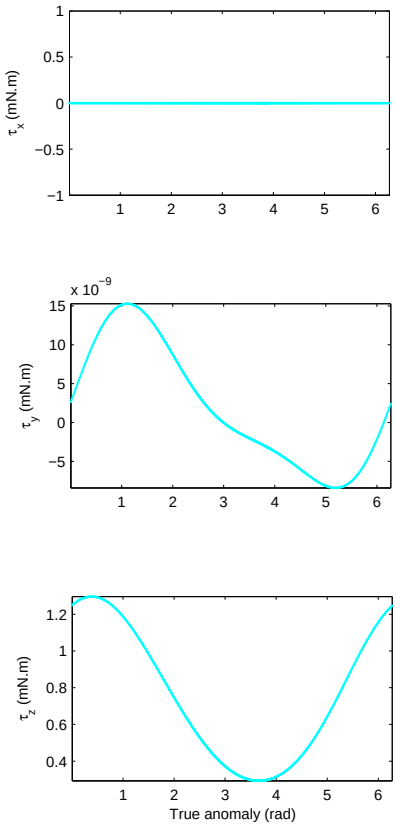

Figure 5.9: Torque produced by the directional mirror for $\delta\mathbf{k}_{5/3}$

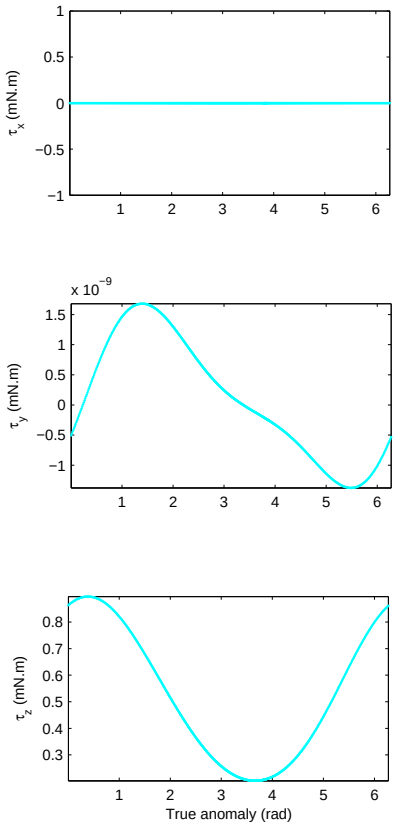

Figure 5.10: Torque produced by the directional mirror for $\delta\mathbf{k}_{5/4}$

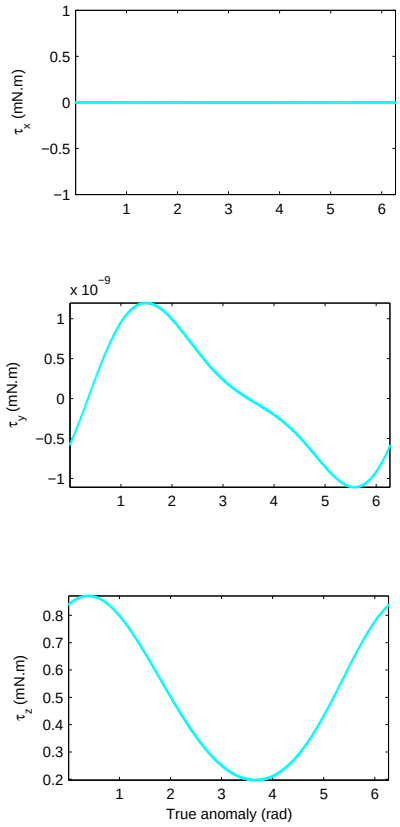

Figure 5.11: Torque produced by the directional mirror for $\delta\mathbf{k}_{5/5}$

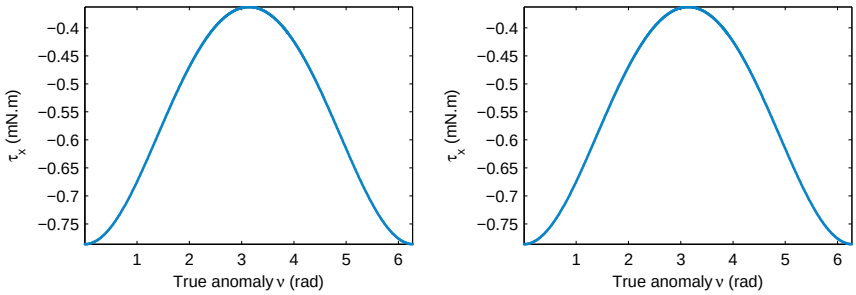

(a) $\delta\mathbf{k}_{5/1}$.

(b) $\delta\mathbf{k}_{5/2}$.

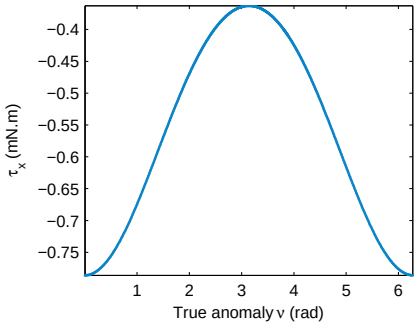

(c) $\delta\mathbf{k}_{5/3}$.

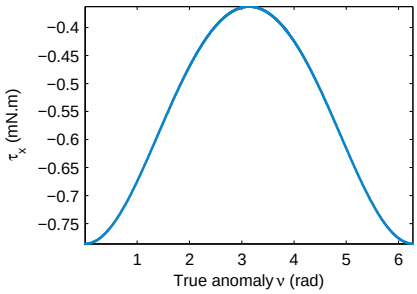

(d) $\delta\mathbf{k}_{5/4}$.

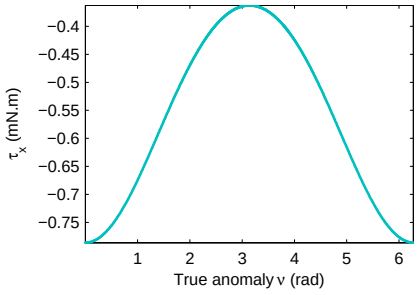

(e) $\delta\mathbf{k}_{5/5}$.

Figure 5.12: Torque produced by y-axis symmetric solar panels.

flexible. This will have to be accounted for in the analysis once a more detailed structural design is completed.

The majority of the spacecraft is designed to be symmetric around the principal axes, however the directional mirror by design will always produce a torque. As seen from the figures, near all of the induced torque is in the z-direction, up to 1 mN·m. The mirror diameter is set to 1 m, however this is an overestimation. In the case of a laser, the beam could be on the order of centimetres, with the only limit being the maximum temperature of the reflector.

6 Navigation Strategy

6.1 Introduction

A number of systems, such as the control law, require knowledge of the position and velocity of the asteroid relative to the spacecraft in the formation. It is assumed that the inertial position and velocity of each spacecraft are known from ground measurements. Furthermore, it is assumed that each spacecraft can measure its attitude with a star tracker. In order to determine the location of the asteroid, an onboard camera is used to first determine the angular direction of the asteroid. Using the formation, the range can than be determined by triangulation. With the same technique we can coordinate the steering of all the beams in order to hit the same spot on the surface of the asteroid.

In this section we present a preliminary analysis of the relative orbit determination of the spacecraft with respect to asteroid. We focus our attention on the dual mirror case since it is the most critical one. The single mirror spacecraft, in fact, has to maintain a fixed angular distance between the spacecraft-asteroid direction and the spacecraft-Sun direction, therefore the beaming direction is constant in time and does not need to be controlled if not to compensate for the rotation of the asteroid.

Previous studies have addressed the navigation in the proximity of minor bodies (see [44, 45] just to quote two) with particular attention to the problem of landing. Here the requirements are substantially different and therefore some of the strategies that could be found in the literature cannot be used. On the other hand the a wide range of navigation techniques based on optical devices, radar, lidar and other instruments have been already developed for past and future missions and are expected to be used for this application as well.

6.2 Simulation

The first step is to correctly locate the asteroid, using a nominal lead spacecraft. Each spacecraft should have a basic idea of the region of space in which the asteroid should be located, however even in the worst cast where no region is known, a wide-coverage scan/search procedure can be implemented. Once the asteroid is in view of the camera, the camera aligns the calculated centre of the asteroid with the boresight of the camera (i.e. the origin $(0, 0)$ on the camera image plane). The camera reference frame $\mathcal{C}$ is defined with the z-axis giving the boresight pointing direction of the camera, and the x-y axes composing the image plane (see Fig. 6.1). For this simulation, the local $y^{\mathcal{C}}$-axis was nominally set parallel to the angular orbital momentum of the spacecraft.

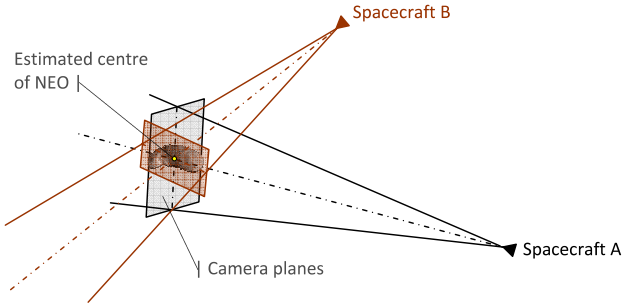

Figure 6.1: Navigation strategy using on-board cameras.

The asteroid is modelled as a series of discrete points composing a hollow ellipsoid, since we are only interested in the surface boundaries of the image (see Fig. 6.2a). The physical dimensions used to model Apophis are given in Table 4.1.

In Fig. 6.2a, $[u, v, w]$ are the axes of inertia of a rotating ellipsoid. As not much is known about the rotational characteristics of Apophis, the smallest radius, w here, was nominally aligned with the direction of orbital momentum ($\hat{z}^{\mathcal{S}}$) with the asteroid rotating about w in the u-v plane. Depending on the geometry of the spacecraft and camera, the points are projected onto the image plane and discritized according to the given pixel size, to account for the errors introduced by rasterization.

A simple equation was used that estimates the average horizontal and vertical pixel locations within the asteroid image on the camera plane. If we defined a set $\mathbf{p}$ of points on the surface of the NEO in 3D mapped onto the discretized 2D camera (or image) plane, then the estimated centre of the asteroid is defined as,

$$\begin{cases} \min \mathbf{p}_x^{\mathcal{C}} + \frac{1}{2}\left(\left|\max \mathbf{p}_x^{\mathcal{C}} - \min \mathbf{p}_x^{\mathcal{C}}\right|\right) \\ \\ \min \mathbf{p}_y^{\mathcal{C}} + \frac{1}{2}\left(\left|\max \mathbf{p}_y^{\mathcal{C}} - \min \mathbf{p}_y^{\mathcal{C}}\right|\right) \end{cases} \tag{6.1}$$

For this study, the approximation is sufficient however a more advanced algorithm is clearly necessary for future studies due to a number of sources of errors, such as the distortion of the image due to high elevation angles. Clipping errors are also a factor, since the vector of points $\mathbf{p}$ given by the camera only contains those seen within the field-of-view (FOV) of the camera. For the simulation, the camera is designed with specification such that the entire asteroid can be contained with the FOV of the camera.

The estimation of the centre gives the angles – spacecraft-relative azimuth and elevation – required by the mirror pointing system, however the range is still outstanding.

If each camera is aligned with the centre of the image on the estimated centre of the asteroid, then all the cameras should be pointing along the spacecraft-asteroid vector. Logically then, the intersection point(s) of these beams will create the spot area. For this simulation, the centre of the NEO was used; in future studies, this should be adjusted to cross on the surface instead, accounting for the changes in range due to rotation.

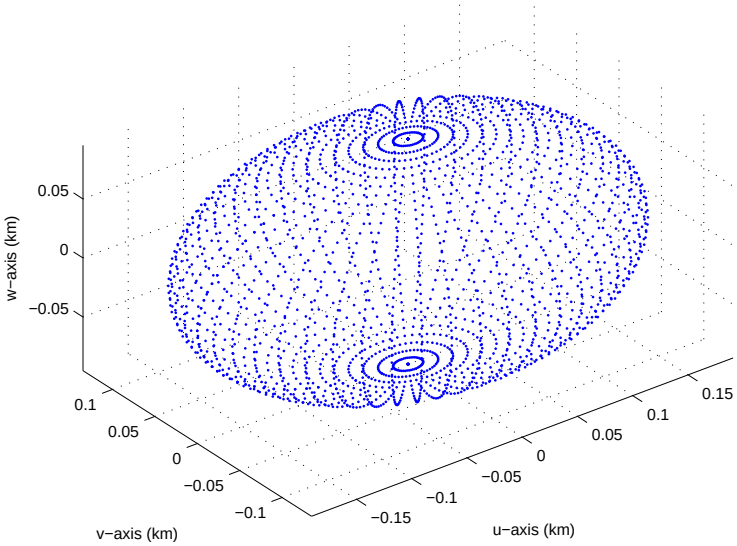

(a) Model of Apohis as a set of discrete surface points of an ellipsoid with dimensions $R_u = 190.92$ m, $R_v = 135.0$ m, $R_w = 95.46$ m. [30]

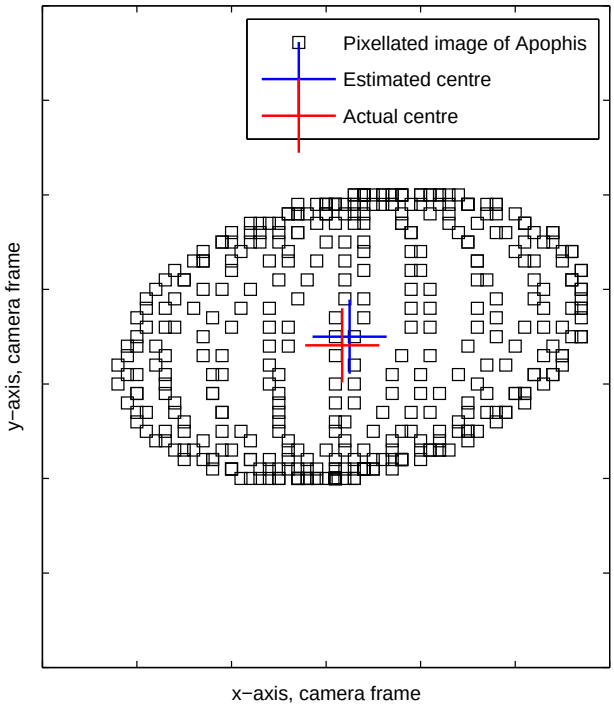

(b) Camera image view of the asteroid Apophis. The pixel size in this plot was enlarged to 10×10 m in order to see the effects of rasterization on the object.

Figure 6.2: Asteroid representations for navigation simulation.

The spacecraft-asteroid vector (i.e. from the camera to the centre of the NEO) can be written in parametric form as,

$$x = v_x t + x_0 \tag{6.2}$$
$$y = v_y t + y_0 \tag{6.3}$$
$$z = v_z t + z_0 \tag{6.4}$$

where $\mathbf{v}$, $[x, y, z]^{\mathcal{O}}$ are in the inertial reference frame. From a simulation point of view, with the angles determined, the only remaining factor to solve is t_A and t_B (corresponding to two spacecraft, e.g. A and B). This can be solved by a minimization function (in this case `fminbnd` in Matlab) where t_A is the free variable. Fixing the direction of camera pointing vector $z_A^{\mathcal{O}}$, the intersection point is moved until the $z_B^{\mathcal{O}}$ camera vector is aligned with the estimated centre of the asteroid from spacecraft B.

Measurement errors were introduced on the position estimate of the spacecraft in inertial space, and the attitude determination each spacecraft. Table 6.1 lists the three different sets of errors used in the simulations, depending on the accuracy of the onboard devices.

Table 6.1: Errors on positional and angular measurements.

		Error set A	Error set B	Error set C
Position	m	5	100	1000
Angle	deg	0.003	0.01	0.001

The camera parameters are given in Table 6.2. For ease of simulation, all the parameters, such as the CCD matrix are assumed to be square, e.g. 800×800 px instead of the more common 600×800 px. Three different cameras configurations were used, representing good (A), poor (B), and optimal (C) which was used for testing only. The focal length is calculated by simple trigonometry,

$$f_\ell = \frac{ccd \times l_{px}}{\tan(fov)} \tag{6.5}$$

For reference, Apophis subtends a half-angle of 76.146 mrads, as seen from a distance of 2.5 km (the minimum distance from the formation).

Table 6.2: Parameters of on-board camera (all dimensions are assumed square, $x^{\mathcal{C}} = y^{\mathcal{C}}$).

		Camera A	Camera B	Camera C
Total field-of-view (fov)	deg	10	20	10
Pixel size (l_{px})	m	$5E$-7	$9E$-6	$1E$-12
CCD Array dimensions (ccd)	pixels	1768	800	8000
Focal length (f_ℓ)	m	$2.5067E$-3	$9.8909E$-3	$2.0417E$-7

To compensate for the errors introduced by rasterization and pointing errors, the intersection points were calculated for each pair of spacecraft. Figure 6.3 shows the differences between the estimated centres determined by each spacecraft-pair combination relative to the actual centre, located at $(0, 0)$. The

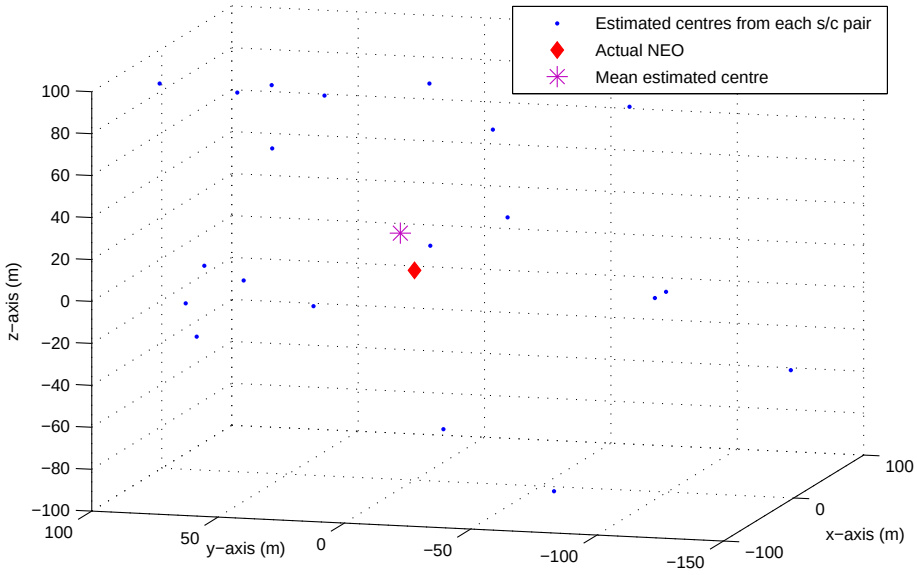

Figure 6.3: Positions of the estimated centres relative to the actual centre of Apophis.

5-spacecraft formation was used, giving 20 estimated values for the centre of the NEO in inertial space, with camera A and error set B, taken at a nominal true anomaly of $\nu = 20°$.

Figures 6.4–6.14 show the mean and standard deviation of the set of estimated centres relative to the actual centre of Apophis in the heliocentric inertial reference frame $\mathcal{O}$, over one full orbit, for each camera and error set.

6.3 Discussion

The navigation strategy proposed in this chapter has two goals:

- coordinate the pointing control of all the spacecraft in order to intersect the beams and hit the same spot on the surface of the asteroid,
- estimate the position of the asteroid during the deflection manoeuvre.

As seen from the figures, the method shown for the navigation works in principle provided that the position of the satellites is known with good accuracy. Although an accuracy of 1 km in position has to be expected for a single spacecraft in deep space, a formation can improve this accuracy by combining the intersatellite position measurements with the position measurement based on other navigation approaches. The use of intersatellite measurements, in fact, would filter out all position errors with opposite sign. A substantial improvement in the estimation of the position of the spacecraft was theoretically proven for the mission LISA in a recent study (see [46]).

Furthermore, note that the algorithm used to isolate the centre from the 2D image plane is overly simplistic and does not use measurements over long arcs. In addition, in the orbits chosen the spacecraft are often in close proximity to

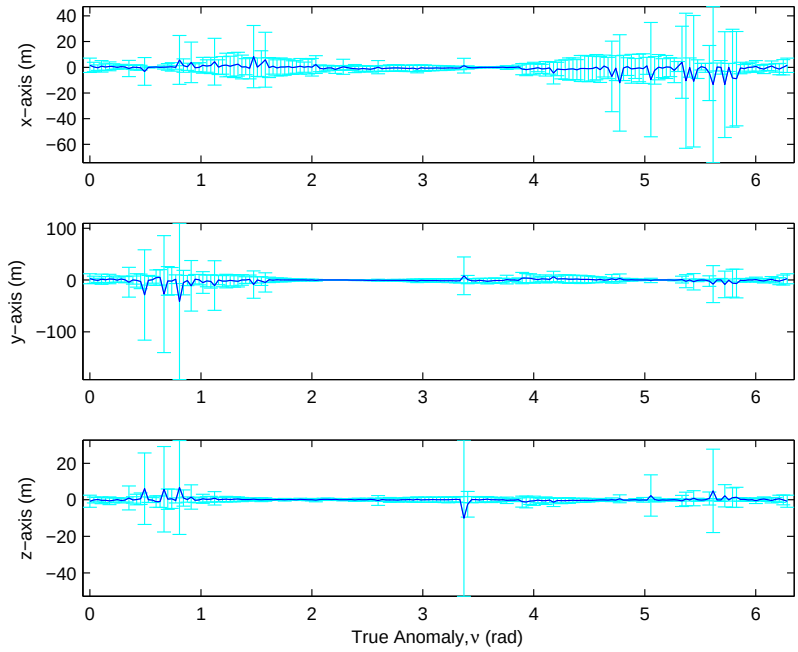

Figure 6.4: Mean and standard deviation (shown as error bars) of estimated centres relative to the actual centre of Apophis in the heliocentric inertial reference frame $\mathcal{O}$, over one full orbit using 5 spacecraft each with Camera A, no errors.

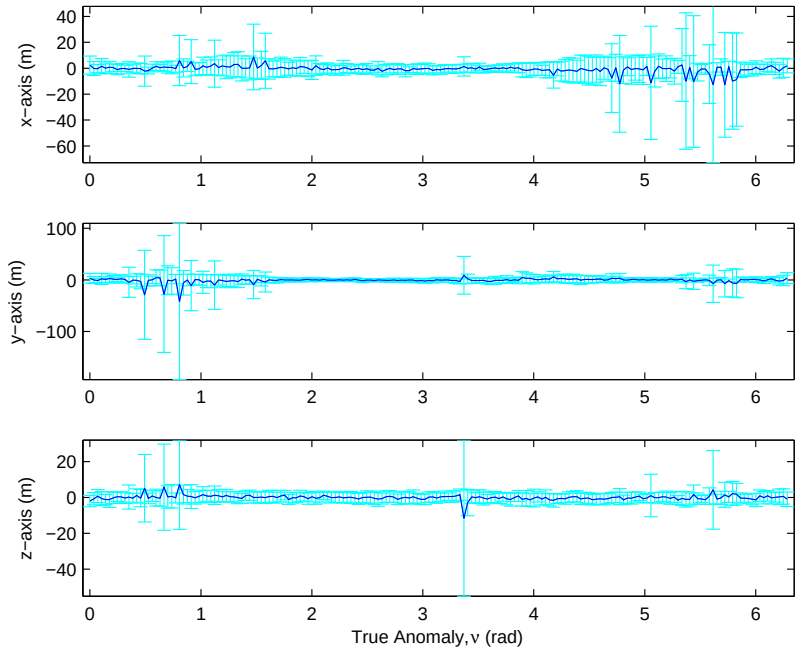

Figure 6.5: Mean and standard deviation (shown as error bars) of estimated centres relative to the actual centre of Apophis in the heliocentric inertial reference frame $\mathcal{O}$, over one full orbit using 5 spacecraft each with Camera A, Error set A.

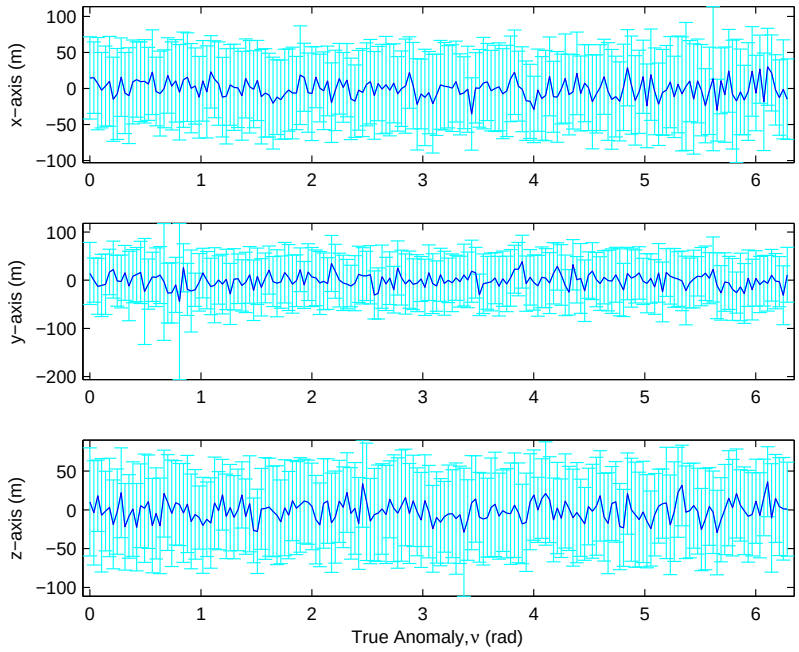

Figure 6.6: Mean and standard deviation (shown as error bars) of estimated centres relative to the actual centre of Apophis in the heliocentric inertial reference frame $\mathcal{O}$, over one full orbit using 5 spacecraft each with Camera A, Error set B.

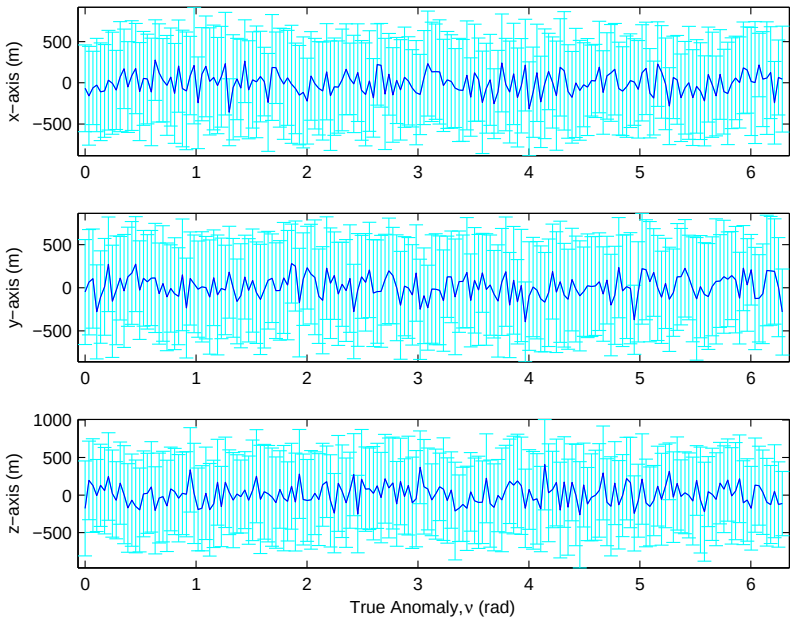

Figure 6.7: Mean and standard deviation (shown as error bars) of estimated centres relative to the actual centre of Apophis in the heliocentric inertial reference frame $\mathcal{O}$, over one full orbit using 5 spacecraft each with Camera A, Error set C.

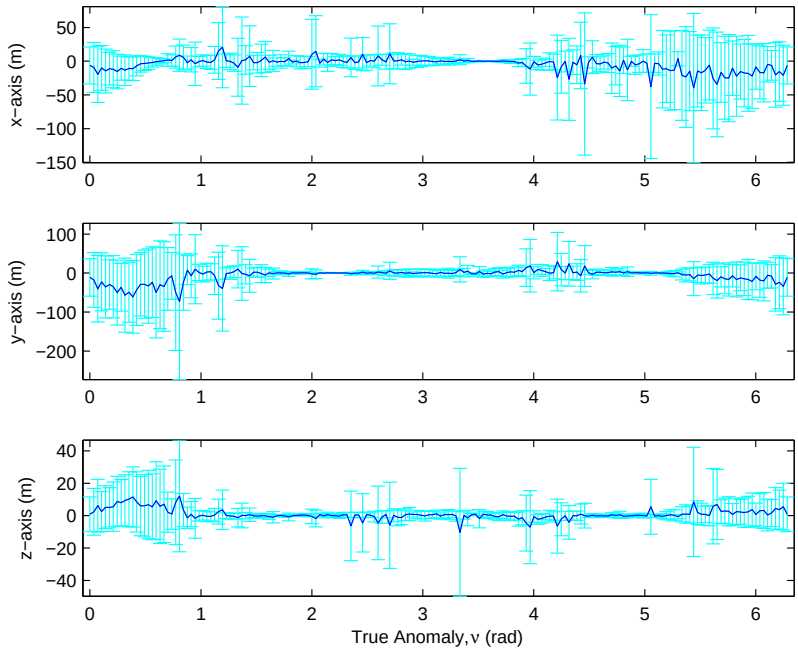

Figure 6.8: Mean and standard deviation (shown as error bars) of estimated centres relative to the actual centre of Apophis in the heliocentric inertial reference frame $\mathcal{O}$, over one full orbit using 5 spacecraft each with Camera B, no errors.

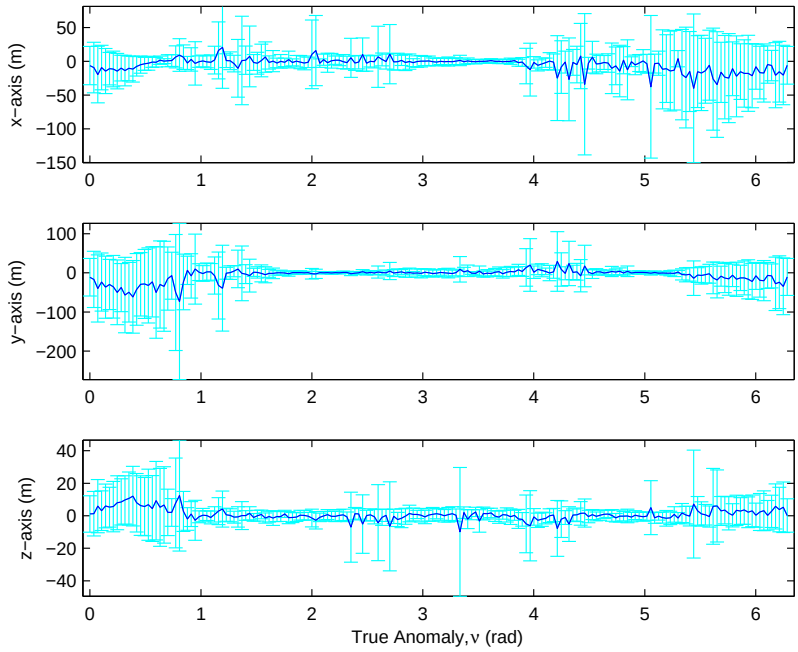

Figure 6.9: Mean and standard deviation (shown as error bars) of estimated centres relative to the actual centre of Apophis in the heliocentric inertial reference frame $\mathcal{O}$, over one full orbit using 5 spacecraft each with Camera B, Error set A.

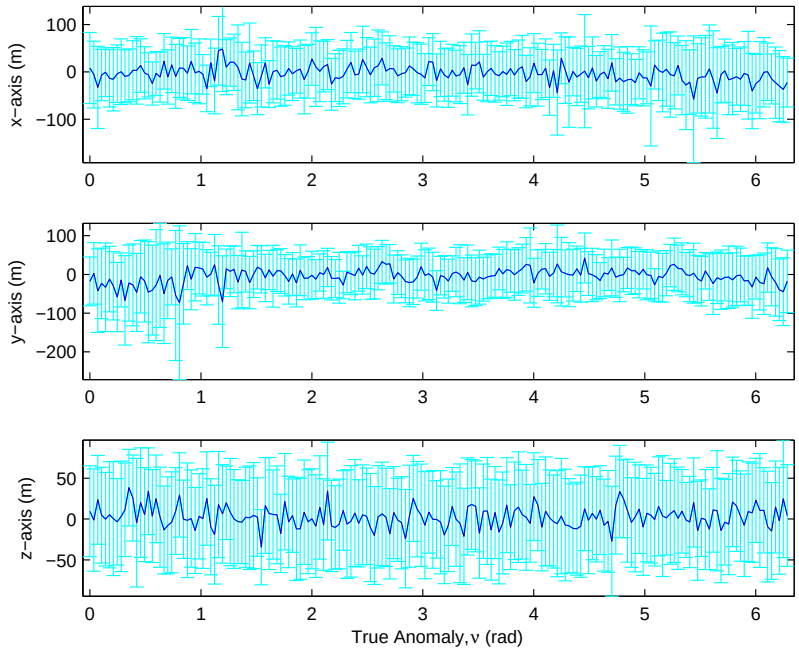

Figure 6.10: Mean and standard deviation (shown as error bars) of estimated centres relative to the actual centre of Apophis in the heliocentric inertial reference frame $\mathcal{O}$, over one full orbit using 5 spacecraft each with Camera B, Error set B.

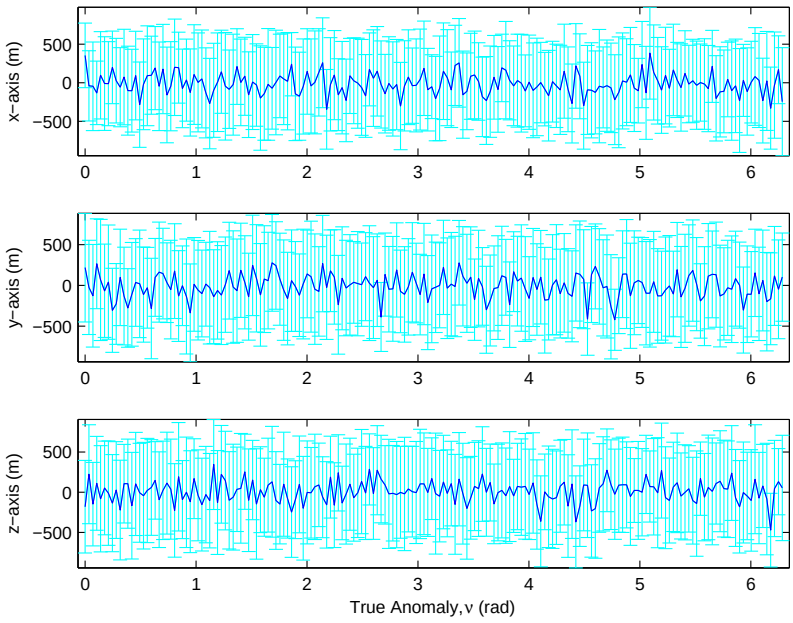

Figure 6.11: Mean and standard deviation (shown as error bars) of estimated centres relative to the actual centre of Apophis in the heliocentric inertial reference frame $\mathcal{O}$, over one full orbit using 5 spacecraft each with Camera B, Error set C.

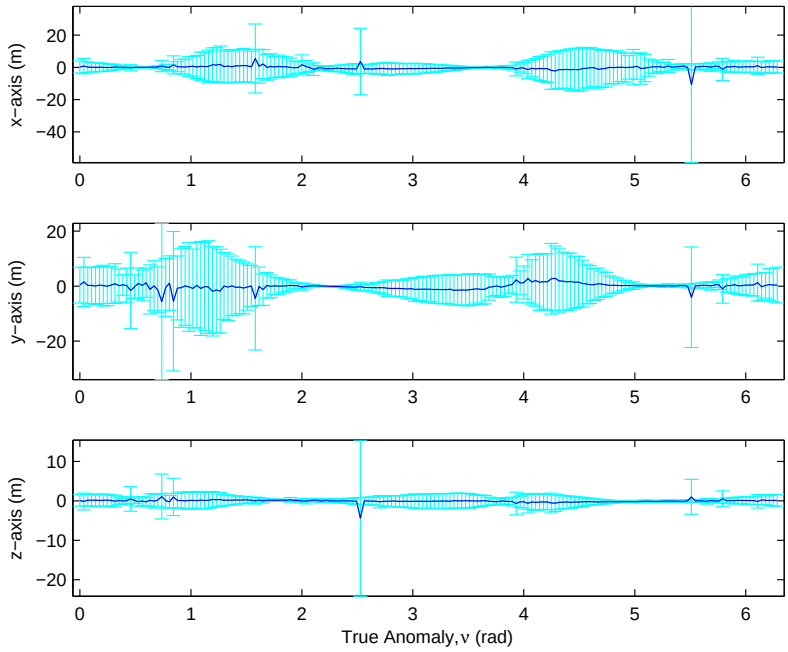

Figure 6.12: Mean and standard deviation (shown as error bars) of estimated centres relative to the actual centre of Apophis in the heliocentric inertial reference frame $\mathcal{O}$, over one full orbit using 5 spacecraft each with Camera C, no errors.

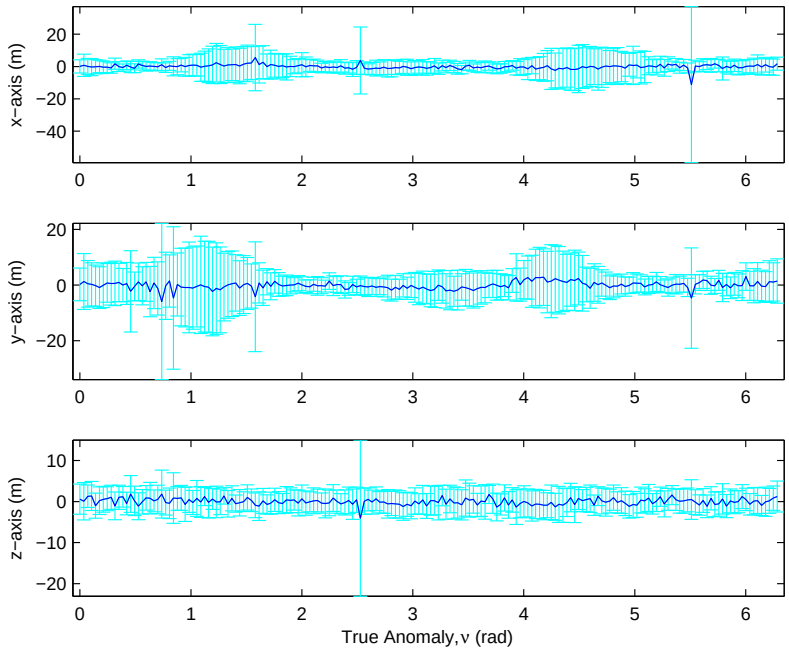

Figure 6.13: Mean and standard deviation (shown as error bars) of estimated centres relative to the actual centre of Apophis in the heliocentric inertial reference frame $\mathcal{O}$, over one full orbit using 5 spacecraft each with Camera C, Error set A.

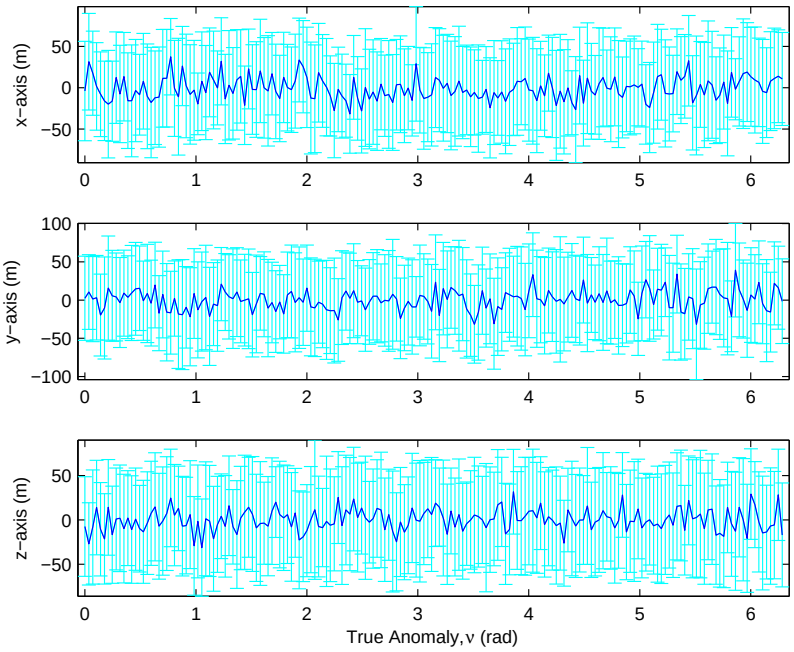

Figure 6.14: Mean and standard deviation (shown as error bars) of estimated centres relative to the actual centre of Apophis in the heliocentric inertial reference frame $\mathcal{O}$, over one full orbit using 5 spacecraft each with Camera C, Error set B.

each other, reducing the accuracy of the differential measurements. This can been seen when the standard deviation in measurements increase around the periapsis.

A better choice of the satellites and of the set of measurements would certainly improve the estimation.

For future work, a Kalman could be added to improve the centre-finding algorithm for elliptical and non-regular objects, and to determine the velocity. The simulation above assumed that the asteroid was a geometric object with no irregularities in the surface beyond those introduced by rasterisation. Moreover, the NEO will be partially in shadow, or eclipse, which the algorithm will have to compensate for.

Therefore, the irregular shape of the asteroid should be known in advance or better the ellipsoid enveloping the true shape of the asteroid should be known in advance.

Last but not least, if the laser option is considered the quality of the beam needs to be controlled during the operations. Existing studies and patents [47] suggest that this is doable with an evolution of current technology.

7 Deployment Options and Mass Budgets

7.1 Requirements for Mirror Bees

Individual mirror bees will comprise a large collector with an area of order 200 m^2, an optical collimator and a spacecraft bus comprising conventional power, data and telemetry subsystems yielding a total bee mass of order 2000 kg (including large mass margins). While the application of a swarm of deployable solar collectors to near Earth hazard mitigation is novel, recent developments in both solar sail technology and inflatable reflectors provide a route towards the key technologies required for the mirror bees system. Solar sail technology development has seen advances in thin film and deployable structures technologies, with 20×20 m sails ground test in both Europe and the US. Inflatable reflectors have been developed for radio frequency antennae and optical telescopes, with active closed-loop shape control.

7.2 Ground and in-orbit tests of deployable reflectors

As part of international efforts to develop solar sail technology for future science missions a number of ground and sub-orbital test campaigns have been undertaken. A DLR/ESA funded ground test of a 20×20 m solar sail in 1999 demonstrated the ability to fabricate, pack and deploy a large reflector using composite booms (Fig. 7.1). A similar NASA ground test in 2004 demonstrated similar capability using inflatable boom technology (Fig. 7.2). A somewhat different configuration was adopted by JAXA for a spinning 10 m diameter reflector deployed in a 2004 sub-orbital sounding rocket test (Fig. 7.3).

Other examples of in-orbit deployment test include the NPO Energia Corp. deployment a spinning 20 m reflector from a Progress supply vehicle in February 1993 (Fig. 7.4). The deployment process was driven by slowly spinning up the stowed reflector using a drive motor. Another spectacular demonstration of a large deployable reflector was achieved in May 1996 during the STS-77 space shuttle mission (Fig. 7.5). The 14 m diameter Inflatable Antenna Experiment (IAE) was designed to test the deployment of a large inflatable structure, to be used principally as a radio frequency reflector.

Also of particular note is a 10×12 m meter offset reflector antenna for L-band communications developed by Contraves Space AG (now Oerlikon Contraves

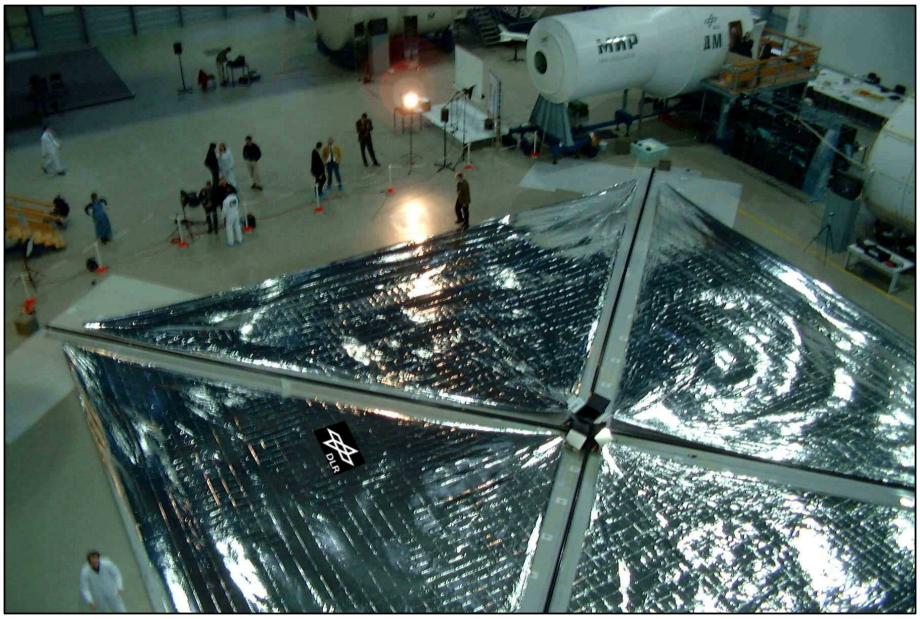

Figure 7.1: 1999, 20×20 m solar sail ground test (DLR/ESA)

Figure 7.2: 2004, 20×20 m solar sail ground test (NASA/AEC)

Figure 7.3: 2004, 10 m diameter disk reflector suborbital test 2004 (JAXA)

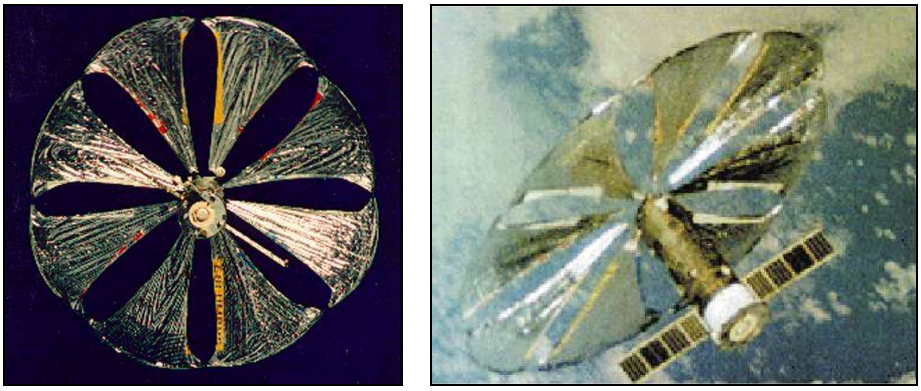

Figure 7.4: 1993, 20 m diameter Znamya-2 spinning reflector experiment (SRC/Energia)

Apace AG) under ESA funding in the early 1980s. Although not deployed in-orbit, this long-term ESA funded technology development activity greatly advanced European capability in inflatable structures technology. The reflector precision was measured while inflated, but not rigidised, and was of order a few mm RMS. The construction of the antennas was based on using two parabolic membranes, supported at their periphery by a toroidal structure.

7.3 Deployable structures technology

Two deployable structures technologies are currently well advanced in Europe - carbon fibre reinforced plastic (CFRP) booms manufactured by DLR and inflatable ISRS booms developed by Contraves Space AG (now Oerlikon Contraves Apace AG). The CFRP booms have already been qualified and ground tested with a 20×20 m solar sail. The inflatable technology for the ISRS booms has been developed by Contraves through ESA funding over many years for a range of inflatable structures applications. Example deployable boom technologies are shown in Fig. 7.6.

The CFRP booms are fabricated by curing and bonding composite shells to form a tubular structure which can be rolled flat for packing, but opens into an

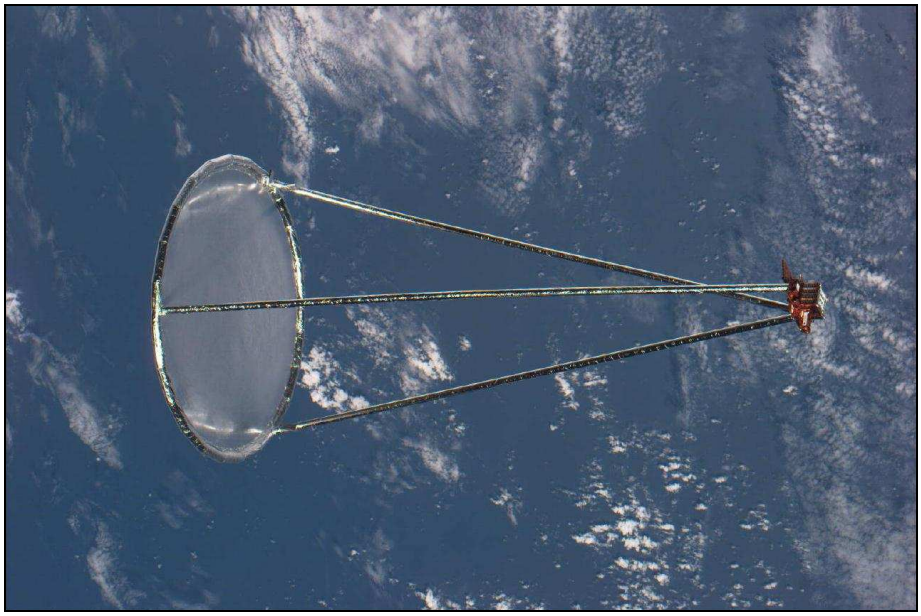

Figure 7.5: 1996, 14 m diameter Inflatable Antenna Experiment (NASA/JPL)

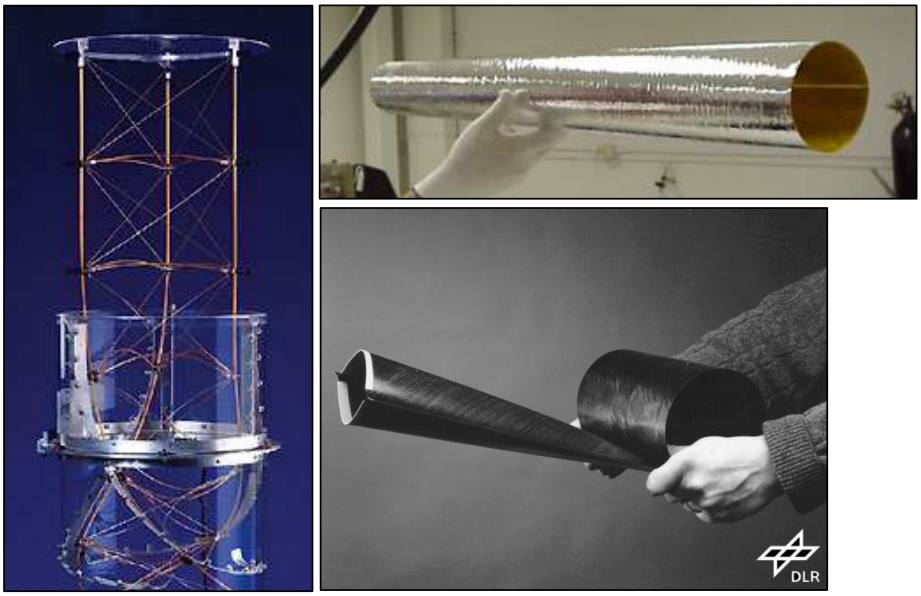

Figure 7.6: Deployable structures technologies: *left* coilable (ATK Inc.), *top right* inflatable space rigidised (L'Garde), *bottom right* composite (DLR)

Figure 7.7: Thin film reflector technologies: *left* CP-1 film, *right* 0.9 μm Mylar

elliptical cross-section under the action of stored strain energy on deployment. The carbon fibre plies used to fabricate the booms are arranged in a symmetric pattern so that there is very low thermal expansion due to differential heating on the boom faces. For the 20×20 m ground test, DLR fabricated 14 m booms with a specific mass of 101 g/m and a stiffness of order 5000 Nm^2. While the DLR booms have desirable mass, stiffness and thermal properties, mass is also be required for a drum to store the booms and for mechanisms, such as drive motors and guides.

The ISRS booms are fabricated from thin layers of fibre-reinforced, chemically rigidised plastic film. After deployment by gas pressure, the booms must be cured under the action of solar heating, which requires a particular set of attitude manoeuvres to ensure uniform curing. An advantage of ISRS type booms is that inflatable structures have been shown to deploy reliably on-orbit. After rigidisation the booms must also be vented to ensure that disturbance torques are not generated by gas leaks through impact damage. To obtain a bending stiffness equal to that of the CFRP booms, inflatable booms require a somewhat greater specific mass, although the mass of the gas inflation system is likely to be less than the mechanical subsystem mass for storing and deploying composite booms. To provide a bending stiffness of order 5000 Nm^2, equal to the CFRP composite booms, the ISRS booms would require a specific mass of approximately 125 g/m.

7.4 Thin film technology

Two options are available for the plastic substrate of the reflector - commercially available 7.6 m aluminised DuPont Kapton film and 1.5 m CP1 film, developed by SRS Technologies for NASA/JPL. While Kapton is readily available in bulk at low cost, the cost of CP1 is significantly higher than Kapton and availability is uncertain since the commercial supplier is manufacturing the product under license to NASA. Mylar is not seen as a suitable substrate for long-term use since it will degrade under the action of solar UV radiation. Example thin film reflector technologies are shown in Fig. 7.7.

Kapton is a widely used polyimide film manufactured by DuPont with a range of desirable mechanical and thermal properties. The HN type film is

available in a minimum thickness of 7.6 m, providing an areal density 10.79 g/m^2. The film can be metalised by vapour deposition and can be readily bonded by a suitable adhesive tape. It is possible to chemically etch Kapton to thinner gauge than 7.6 m, but large-scale processing would be required to produce the bulk quantity for a solar sail. Kapton HN film is available metalised in a roll width of 1.4 m. CP1 film is available from SRS technologies who have developed the film for solar sail applications under license to NASA. The film has similar mechanical properties to Kapton, but is available in a significantly thinner gauge. The 1.5 m CP1 film is available in roll widths of order 1 m and provides an areal density of only 2.15 g/m^2.

An addition possibility which will not be pursued here is Mylar film. Mylar is available in extremely thin gauge and at relatively low cost, but degrades under the action of solar UV radiation. Protection of the film by the sail metallic coating is unlikely to be sufficient due to small-scale cracks in the coating which could allow UV penetration and local degradation of the film mechanical properties. Although Mylar poses issues associated with survivability, it may represent an option for limited, short duration demonstration missions.

In addition to a polyamide substrate, a reflective film also requires a suitable metallic coating. The optimum coating for the Sun facing surface of the reflector is generally accepted as aluminium with a rear surface coating of high emissivity chromium for thermal control. However, for a demonstration mission in Earth orbit thermal loads are such that a coating of aluminium on both sides of the sail is acceptable. Using vapour deposition techniques a coating of order 0.1 m can be deposited providing a contribution to the areal density of 0.54 g/m^2.

The individual strips of aluminised film must also be bonded and reinforcements added at the stressed edges of the film. Bonding can be achieved using adhesive tape or heat sealing, although adhesive is a simpler fabrication method to use. Previous studies show that bonding will add a mass penalty of approximately 10% of the mass of the coated sail film. Aluminised 7.6 m Kapton HN film with bonding will therefore have a total areal density of 12.46 g/m^2.

7.5 Other deployable reflector programmes

A number of other technology development programmes indicate concepts suitable for mirror bees. The centre of the use of inflatable structures technology to deploy a large passive or actively controlled reflector with a typical areal density of order 1 – 5 kg/m^2.

7.5.1 Inflatable power antenna

A 6.7 m aperture inflatable reflector with a subsystem mass of 21.9 kg is used as a solar concentrator for outer solar system mission and a high gain antenna (Fig. 7.8). A torus is used to support a lenticular reflector, both of which are deployed using gas pressure. Since the mass of gas to maintain pressure would be prohibitively large due to micro-meteorite leaks, rigidisation is required after deployment using a thermal setting resin. Ground testing has demonstrated an RMS surface precision less than 1 mm. The areal density of the reflector for the combined solar/RF concentrator subsystem is 6.4 kg/m^2.

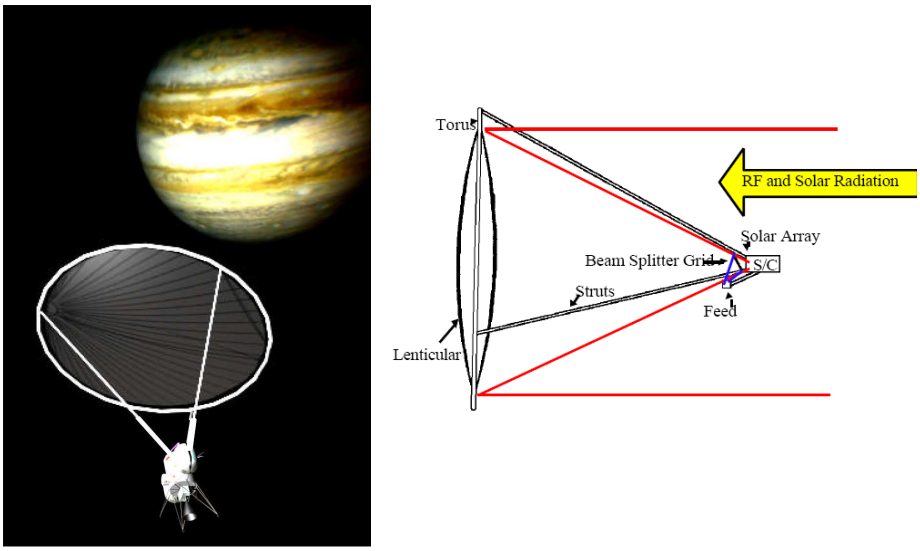

Figure 7.8: Inflatable Power Antenna optical and RF path (L'Garde Inc)

7.5.2 ARISE

A 25 m aperture RF (GHz range) reflector with a subsystem mass of 215 kg is used for a space-based radio astronomy mission (Fig. /reffig:sys9). Using heritage from the 1996 inflatable antenna experiment, a torus and 3 booms are used to attach the main reflector to secondary systems. The expected RMS surface precision is of order 0.2 mm. The areal density of the RF reflector subsystem is 0.44 kg/m^2. Precision surface control can be achieved using piezo-electric actuators to manipulate the edge tension of the reflector membrane (Fig. 7.10).

7.5.3 Mirror Bees

The ARISE areal density is low since the reflector is for an RF system. However, assuming an optical quality reflector system an areal density of order 5 kg/m^2 can be expected, based on future requirement for 20 – 40 m class deployable optical mirrors (Fig. 7.11). For a mirror bee area of order 200 m^2, the expected primary reflector mass can be estimated at 1000 kg. However, this estimate is in the extreme case of an optically flat reflector. This leaves 1000 kg for additional subsystems for an estimated bee mass of 2000 kg.

7.6 Mass Budget

In order to assess the dry mass for a single mirror bee a range of technology levels have been assumed, from existing flight hardware (Inflatable Antenna Experiment) through to a conceptual membrane system with embedded sensing and actuation. The key driver for the mirror bee mass budget is the areal density of the adaptive reflector assembly. A range of technology readiness levels (TRL)

Figure 7.9: ARISE inflatable reflector (NASA/JPL)

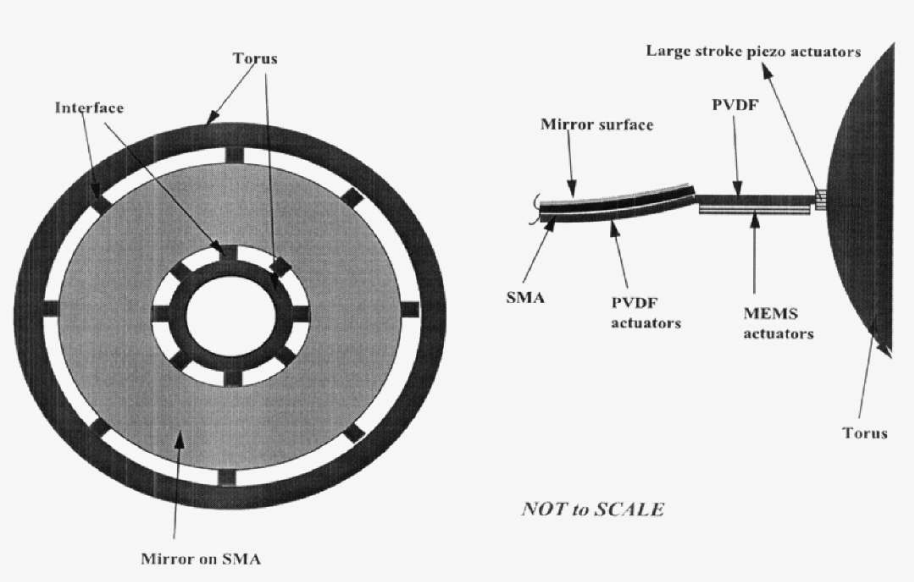

Figure 7.10: Active shape control using edge tension MEMS elements (NASA/JPL)

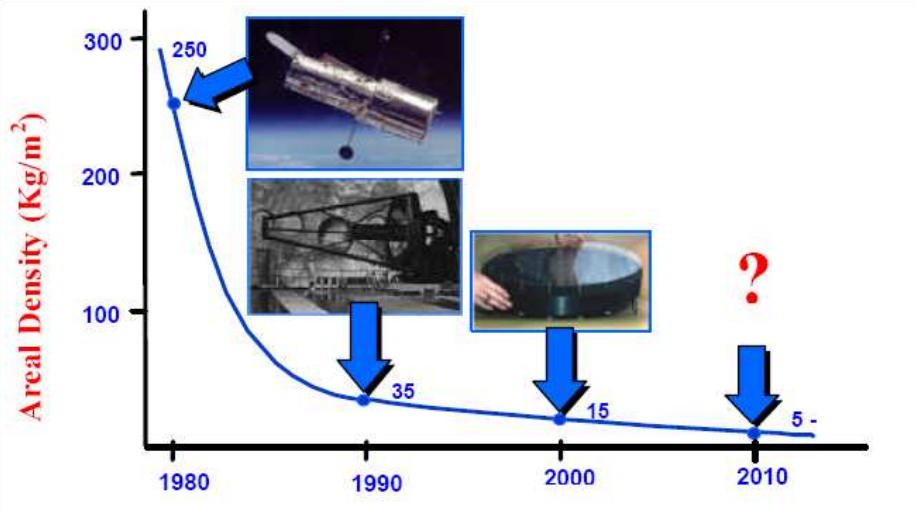

Figure 7.11: Future trends in mirror areal density (Composite Optics Inc)

will be considered with appropriate mass margins. It will be assumed that the reflector mass includes all associated control hardware.

The spacecraft bus is assumed to be comparable to the NEAR spacecraft and is representative of a mid-sized bus operating in deep space at a solar distance of up to 2.2 AU. The NEAR dry mass is 487 kg so that a 500 kg bus is assumed with a 10% mass margin given the flight heritage of the NEAR spacecraft. The bus is assumed to provide power, telecommunications and attitude sensing functions. It is assumed that the adaptive reflector is used to manage the off-set of centre-of-mass and centre-of-pressure which is the primary attitude disturbance.

In addition to the adaptive reflector and bus, with appropriate mass margins, a system contingency of 20% is added to provide margin for integration of the bus and adaptive reflector.

The following 3 levels of system performance are considered:

Mass Budget A Based on Inflatable Antenna Experiment flight hardware $\sim$5 kg/m^2 [48]. The TRL is assumed to be 6 since flight hardware has been demonstrated, although for an RF rather than optical system. A subsystem mass margin of 10% is added. See Table 7.1.

Mass Budget B Based on ARISE RF Radio Telescope study $\sim$0.5 kg/m^2 [49]. The TRL is assumed to be 4 initial technology development for the ARISE mission has been undertaken. A subsystem mass margin of 15% is added. See Table 7.2.

Mass Budget C Based on Innovative Large-Aperture Concepts, $\sim$0.05 kg/m^2 [50]. The TRL is assumed to be 2 since the adaptive membrane system in at a conceptual level, although mass estimates have been made. A subsystem mass margin of 20% is added. See Table 7.3.

The mass in each one of the tables has to be increased to consider the mass at launch and the propellant needed for orbit maintenance. However, as shown

Table 7.1: Mass budget A: Based on Inflatable Antenna Experiment flight hardware, 5 kg/m^2.

Item	TRL	Area (m^2)	Mass (kg)	Margin (%)	Total (kg)
Adaptive reflector	6	3000	15000	10	16500
Bus	9		500	10	550
Contingency				20	3410
Dry Mass					20460

Table 7.2: Mass budget B: Based on ARISE RF Radio Telescope study, 0.5 kg/m^2.

Item	TRL	Area (m^2)	Mass (kg)	Margin (%)	Total (kg)
Adaptive reflector	4	3000	1500	15	1725
Bus	9		500	10	550
Contingency				20	455
Dry Mass					2730

Table 7.3: Mass budget C: Based on advanced membrane primary mirror study, 0.05 kg/m^2.

Item	TRL	Area (m^2)	Mass (kg)	Margin (%)	Total (kg)
Adaptive reflector	2	3000	150	20	180
Bus	9		500	10	550
Contingency				20	146
Dry Mass					876

in Section 4 on the orbit control of the spacecraft, the level of thrust required to maintain the orbit is very low. From previous studies [1, 8], we could see that Apophis could be rendezvoused with a low thrust transfer about 470 days long and a maximum thrust level of 0.6 N for a 3000 kg spacecraft and 3200 s of I_{sp}. For this types of transfers we can have a non-optimised propellant consumption of 30% of the initial mass. We maintain the same assumption in this estimation of the total mass of the spacecraft. Therefore, each mass in the previous tables has to be augmented by a factor of 1.4 due to the transfer cost.

The orbit control in the case of the AEP solution is negligible and could be performed with high I_{sp} FEEP engines (I_{sp} = 10000 s) with a negligible mass consumption compared to the transfer.

If a laser system is used instead of the direct imaging, the spacecraft is more complex and requires more elements. We consider here the following configurations:

- primary adaptive solar collector, solar arrays to convert the solar energy into electric power, semiconductor laser as beaming system, cooling system for solar arrays and laser (Table 7.4)
- primary parabolic (or spherical) solar collector, solar arrays to convert the

solar energy into electric power, semiconductor laser as beaming system, cooling system for solar arrays and laser (Table 7.5)

- large solar arrays (standard technology) to convert the solar energy into electric power, semiconductor laser as beaming system, cooling system for solar arrays and laser (Table 7.6)
- large solar arrays (advanced technology) to convert the solar energy into electric power, semiconductor laser as beaming system, cooling system for solar arrays and laser (Table 7.7)

The mass of the bus and of the primary mirror are based on the previous estimation for the direct imaging system. The laser mass accounts for the mass of the semiconductor, the cavity but no optics, however we use a 50% to include the mass of casing and optical elements. The mass of the cooling system, which is generally the most massive part is computed separately.

The mass of the solar arrays in the case of the configurations with solar collector is for a standard solar array with high efficiency, rigid structural support and not concentrator.

The cooling system is a critical component for the laser option. If large solar arrays are used, with no solar collector, the cooling system needs only to refrigerate the laser and not the solar panels. If the solar collector solution is used instead, the cooling process has two stages: refrigeration of the solar array, refrigeration of the laser. The assumption here is that the laser can operate between 0°C and 40°C while the solar array cannot operate above 100°C. Assuming an efficiency of the laser that can go up to 75%, the largest part of the power needs to be dissipated at the first stage since we do not expect an efficiency of the solar arrays higher than 40%.

For this mass budget we assumed a reference case consisting of a solar collector (or equivalent large solar array) with a surface area of 314 m^2, collecting, at 1 AU, 429.5 kW of power. If the solar arrays are operating at 40% efficiency the cooling system will have to dissipate 257.7 kW at the first stage.

The radiator is located on the shadow cone of the primary mirror for all cases. However, in the case of the adaptive mirror the laser has to be placed between the primary mirror and the asteroid. Therefore, the heat has to be transported from the laser/solar panel to the radiator. In order to maintain the temperature of the solar array below 100°C, the radiator has to have a total irradiating area of about 300 m^2 therefore comparable with the surface area of the solar collector (see Section 3.4).

Note that the dissipated power is irradiated in every direction randomly and therefore does not provide an additional thrust. This assumption will have to be verified once a structural configuration for the radiators is defined.

In order to transport the heat we assume the use of a dual-phase system with ammonia as working fluid. A pumping system is placed in the shadow cone with a mass of 3 kg per pump and a total of 10 pumps (based on the transport rate of standard pumping systems and on the Joules per second that need to be removed). The distance of the solar array from the surface of the primary mirror is assumed to be 2 times the aperture therefore 40 m in this case (the diameter of the mirror is 20 m). We consider a mass of 0.3 kg/m for the pipes 3 g/m for the ammonia. The system is assumed to transport 200 L of

Table 7.4: Adaptive primary mirror plus laser.

Component	Specific mass	Mass (kg)	Margin (%)	Subtotal (kg)	Accumulative total (kg)
Primary mirror	0.1 kg/m^2	32.52	25	40.65	40.65
Laser	0.005 kg/W	601.24	50	901.86	942.51
Solar arrays	1 kg/m^2	3.14	15	3.611	946.12
Cables	20% m_{elec}	189.22	0	189.22	1135.35
Radiator (solar array)	1.4 kg/m^2	420	20	504	1639.35
Radiator (laser)	1.4 kg/m^2	112	20	134.40	177.75
Pipes	0.3 kg/m	12	20	14.4	1788.15
Pumps	10×3 kg	30	20	36	1824.15
Bus	-	500	20	600	2424.15
Propellant	40% m_{dry}	969.66	0	969.66	3393.80
Tanks	10% m_{fuel}	96.97	0	96.97	**3490.77**

ammonia per hour which corresponds to 8 m/s of flow speed in the pipes with a $R_e = 150000$ and a pressure loss in the pipes of 16 bars.

The radiator mass is based on advanced technology for all the configurations [51].

If the laser and the solar array are both in the shadow cone of the primary mirror (see Table 7.5)the system simplifies a bit because there is no need to transport the heat and pumps and pipes are not necessary. The idea is to place a secondary reflective mirror that reflects the concentrated light through hole in the primary mirror to the back of the primary. The solar array and the laser are directly connected to the radiator.

If we assume a reflectivity of the secondary mirror of 99% we would need an additional radiator attached to the secondary with a total area of 7 m^2 (assuming an absorptivity of 0.2).

The total mass of the spacecraft is lower than in the previous case and also the complexity of the cooling system is reduced.

If no solar collector is used (see Tables 7.6 and 7.7) then the cooling system and the laser are placed in the shadow cone of the solar array. The mass of the solar arrays is taken from [52] for the standard and for the advanced technology. Assuming standard technology the system with large flexible solar arrays is expected to be more massive mainly for two reasons: the overall power system including power distribution and cabling is more massive and solar arrays need stretched lenses to increase efficiency.

The advanced system in Table 7.7 would be lighter and closer in mass to the system in Table 7.4.

7.7 Discussion

This preliminary analysis of the mass budget is meant to provide a comparative assessment of some of the alternative solutions proposed in this study.

From the computation of the mass budget for the direct imaging system it appears that a swarm of 26 satellites with TRL 4 for the mirror would be

Table 7.5: Fixed primary mirror plus laser.

Component	Specific mass	Mass (kg)	Margin (%)	Subtotal (kg)	Accumulative total (kg)
Primary mirror	0.05 kg/m^2	15.71	25	19.63	19.63
Directional mirror	0.1 kg/m^2	0.650	25	0.813	20.45
Laser	0.005 W/m^2	601.24	50	901.86	922.30
Solar arrays	1 kg/m^2	3.14	15	3.611	925.92
Cables	20% m_{elec}	185.18	0	185.18	1111.10
Radiator (solar array)	1.4 kg/m^2	420.0	20	504.0	1615.10
Radiator (laser)	1.4 kg/m^2	112.0	20	134.4	1749.50
Radiator of reflective mirror	1.4 kg/m^2	9.79	20	11.76	1761.26
Bus	-	500	20	600	2361.26
Propellant	40% m_{dry}	944.50	0	944.50	3305.76
Tanks	10% m_{fuel}	94.45	0	94.45	**3400.21**

Table 7.6: Primary solar array plus laser, using standard solar array technology.

Component	Specific mass	Mass (kg)	Margin (%)	Subtotal (kg)	Accumulative total (kg)
Directional mirror	0.1 kg/m^2	0.3251	25	0.406	0.406
Laser	0.005 kg/W	601.24	50	901.86	902.26
Solar arrays	150 kg/W	1145.22	15	1317.00	2219.26
Cables	20% m_{elec}	443.79	0.00	443.79	2663.11
Radiator (laser)	1.4 kg/m^2	112.00	20	134.40	2797.51
Bus	-	500.00	20	600.00	3397.51
Propellant	40% m_{dry}	1359.01	0	1359.01	4756.52
Tanks	10% m_{fuel}	135.90	0	135.90	**4892.42**

composed of satellites with a 80 m diameter mirror and a mass between 3.5 and 4.5 tons per spacecraft at launch. A more reasonable swarm would need a lighter adaptive mirror which at present appears to be at TRL 2.

A system based on a solar pumped laser with a primary mirror of smaller size (20 m diameter) would have a comparable mass per spacecraft with the same number of spacecraft.

It should be noted that for both the direct imaging system and for the laser system the mass is directly proportional to the surface area and therefore it is proportional to the square of the aperture of the collector. This would suggest in both cases to go for many spacecraft of small size rather than a single large one.

On the other hand a small reflector in the case of a direct imaging system would provide a little concentration factor. A complete trade off of the number of satellites against the mass and size of each satellite for this concept is still required to complete this analysis.

The TRL of the laser solution strongly depends on the TRL of the laser and of the solar arrays. Most of the assumptions are based on current laboratory

Table 7.7: Primary solar array plus laser, using advanced solar array technology.

Component	Specific mass	Mass (kg)	Margin (%)	Subtotal (kg)	Accumulative total (kg)
Directional mirror	0.1 kg/m^2	0.3251	25	0.406	0.406
Laser	0.005 kg/W	601.24	50	901.86	902.26
Solar arrays	350 kg/W	490.81	15	564.43	1466.69
Cables	20% m_{elec}	293.28	0	293.28	1760.03
Radiator (laser)	1.4 kg/m^2	112.00	20	134.40	1894.43
Bus	-	500.00	20	600.00	2494.43
Propellant	40% m_{dry}	997.77	0	997.77	3492.20
Tanks	10% m_{fuel}	99.78	0	99.78	**3591.98**

tests in both areas (which means TRL 4 or higher) but the overall system for space applications has still to be developed (TRL 2-4). The investment in the development of highly efficient lasers and solar arrays goes beyond the deflection of asteroids and is progressing very fast due to the thousands of commercial applications.

We would like to conclude this section by underlining that the mass budget and most of the calculations in this report are based on the assumption that the system requires a concentration factor of 2500. This assumption corresponds to a deflection of over 20000 km with a 60 m in diameter mirror in 2 years of operation time before the expected impact (see [8]). If the warning time is extended from 2 to 5 years, the required concentration ratio can be reduced for the same deflection distance. Note that this performance is comparable to a nuclear stand-off system of similar mass.

Figures 7.12–7.13 provide an estimation of the required operation time, along the x axis, against the concentration ratio for different warning times (i.e., time from the beginning of the deflection operation to the date of the forecasted impact) and two different estimated masses of Apophis for each of the two systems. The warning times are given as multiples of the orbital period of the NEO ($T_{\text{A}} = 323.5599$ days) instead of Earth years, such the starting true anomaly is always the same. Due to the eccentricity of the orbit of Apophis, the effect of the thrust on the deflection distance changes depending on the orbital location. Figure 7.14 show the differences in required thrust time for a set of warning times between 4–6 T_{A}, or 1294–1941 days prior to the t_{MOID} on 13 April 2036 (64796.56736 MJD). The thrust duration is plotted against both the true anomaly of the NEO at the start of the thrust segment (Fig. 7.14a), and the warning time (Fig. 7.14b).

The figures suggest an important point about the mirror bee system: the system is very flexible and scalable. It is therefore expected that an optimal trade off point exists between warning time, number of spacecraft, size of the spacecraft, deflection and total operation time.

Figure 7.15 shows the total expelled mass (from $\dot{m}_{exp}$ in (4.5)) versus a fixed value of the 'system' concentration ratio, i.e. the number of spacecraft times the concentration ratio of each individual spacecraft. It is clearly shown in the plot, that for a larger number of spacecraft (e.g., 3) with a smaller individual concentration ratio (e.g., 1000), a greater thrust and hence deflection can be

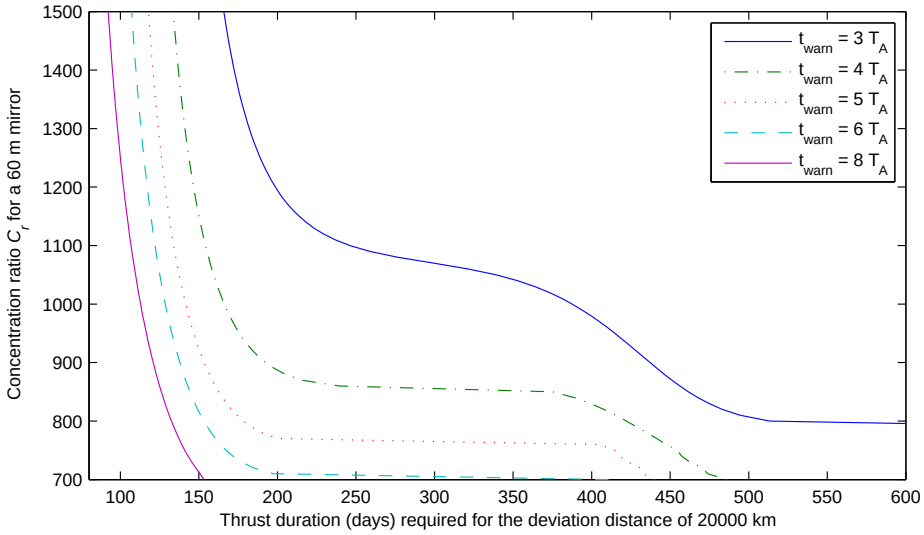

(a) Mass of Apophis $2.7E10$ kg.

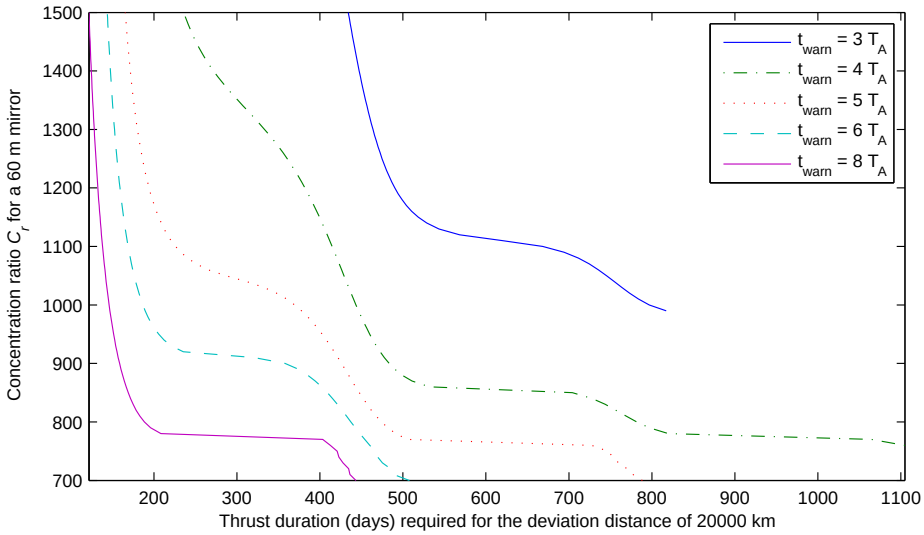

(b) Mass of Apophis of $4.6E10$ kg.

Figure 7.12: Concentration ratio vs required thrust time for a single 60 m diameter mirror using direct imaging to achieve a deflection of 20000 km at the 2036 MOID.

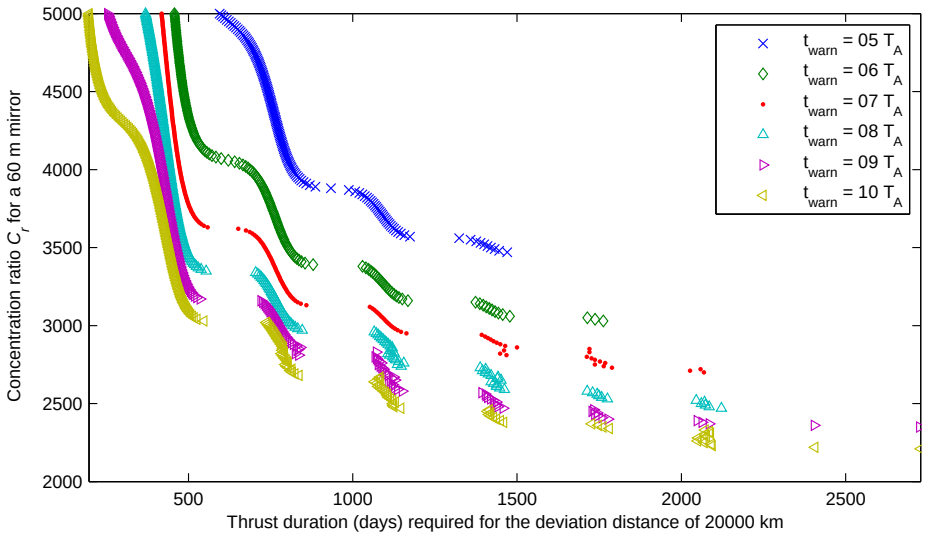

(a) Mass of Apophis $2.7E10$ kg.

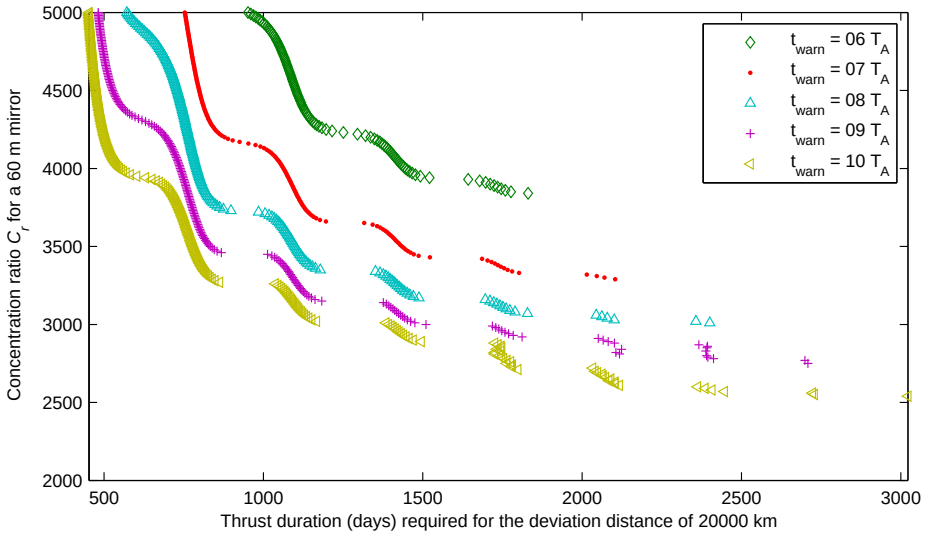

(b) Mass of Apophis of $4.6E10$ kg.

Figure 7.13: Concentration ratio vs required thrust time for a single 60 m diameter mirror using the laser to achieve a deflection of 20000 km at the 2036 MOID.

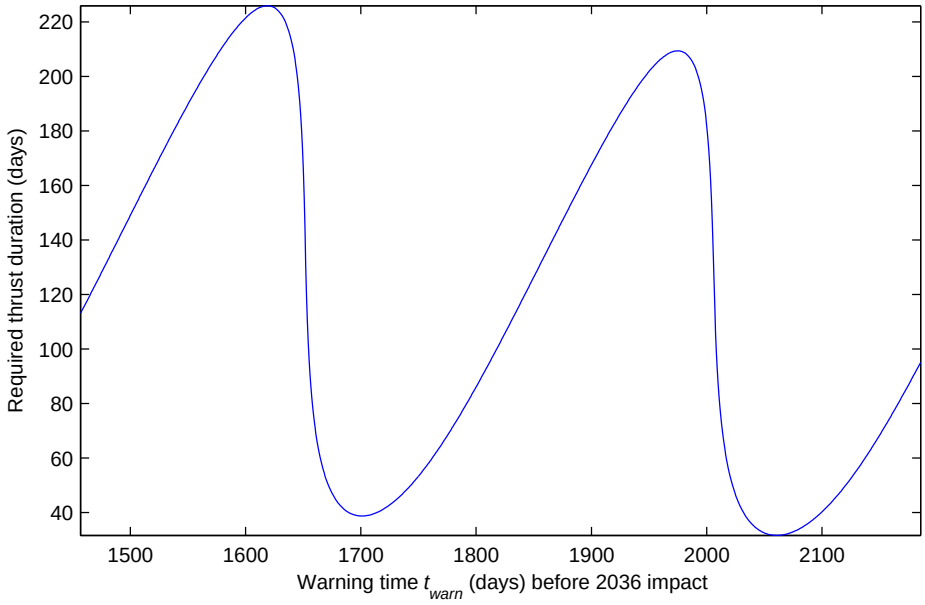

(a)

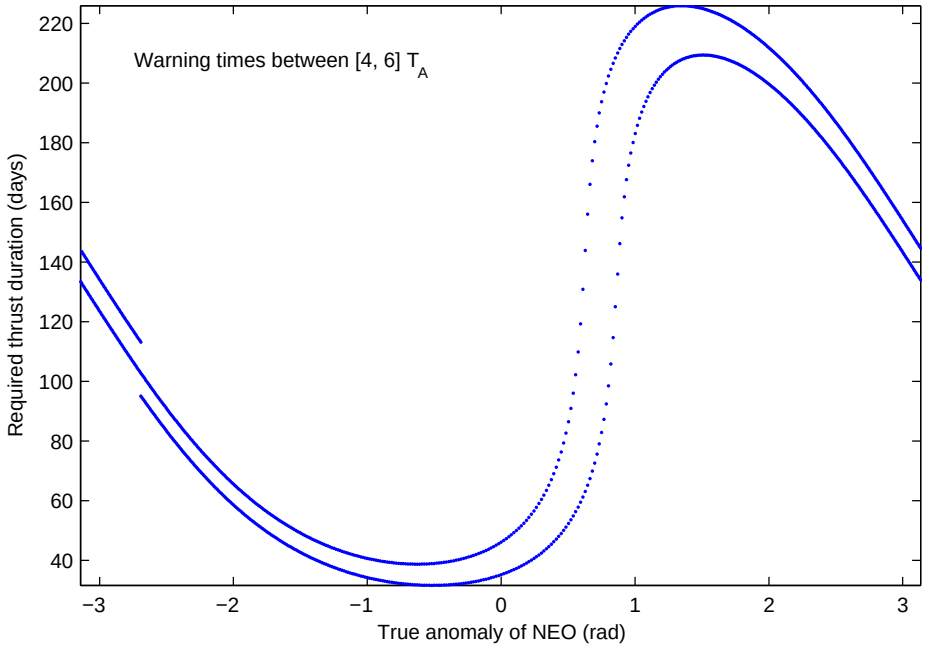

(b)

Figure 7.14: Effect of orbital location at the start of thrust period, on the required duration to achieve a deflection of 10000 km at $t_{\text{MOID}} = 64796.56736$ MJD using a single 60 m mirror with direct imaging ($C_r = 1000$).

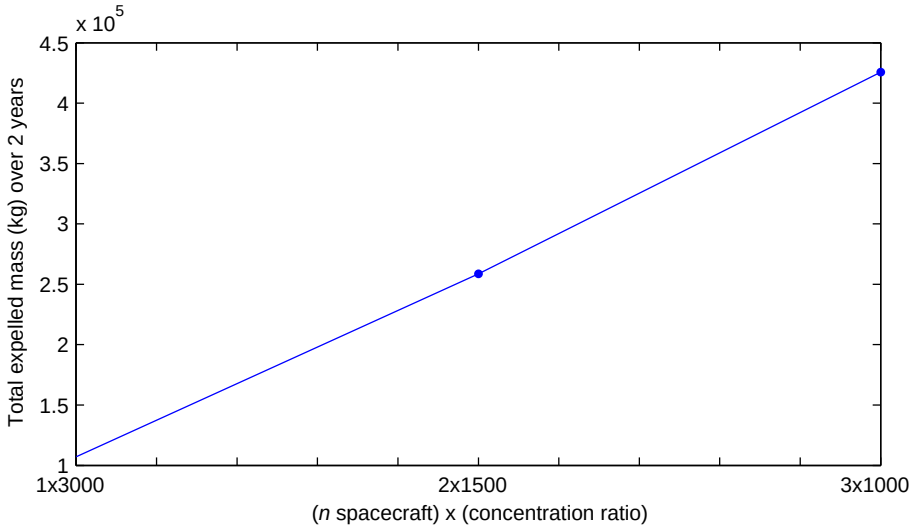

Figure 7.15: Total asteroid debris mass expelled by sublimation vs a system concentration factor which is composed of the number of spacecraft in the formation multiplied by the individual concentration ratio of each onboard focusing system.

achieved.

Figure 7.15 also shows that below a given number of satellites and a given concentration ratio (lower left corner of the plot), deviating the asteroid is not possible. The power density is too low and the sublimation process does not start.

Figures 7.16–7.24 show the achieved deflection distance at the MOID with the Earth in 2036 (t_{MOID} =13252.06736 MJD2000) versus a given number of satellites, concentration ratios, different warning and thrusting times (t_{warn}, t_{thrust}), a fixed aperture diameter of the primary mirror (d_{M}) and system power efficiency (η_{sys}). In the case of the laser system, the efficiency is set to 25%, whereas for the direct imaging, a system efficiency of 90% was used. The thrust leg is assumed to start at ($t_{\text{MOID}} - t_{warn}$), and thrust continuously until ($t_{\text{MOID}} - t_{warn} + t_{thrust}$).

One important thing to note is that increasing the concentration ratio does not improve the deviation. According to the thrust model in equations (4.5) and (4.6), the thrust magnitude depends on the input power and surface area illuminated by the beam. As the concentration ratio increases, the area, for a fixed size mirror, decreases and therefore the thrust does not improve. On the other hand superimposing the beams increases the power density and leaves the size of the spot area unchanged. Therefore, rather than increasing the concentration ratio, the ideal strategy would be to increase the number of beams with constant concentration ratio.

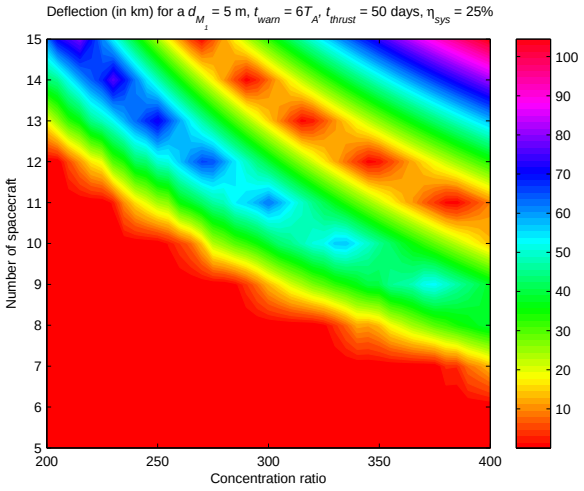

(a)

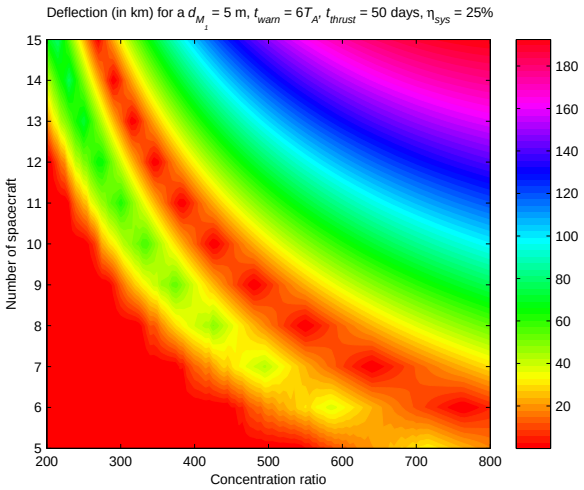

(b)

Figure 7.16: Deviation distance for various concentration ratios and number of spacecraft, assuming a 5 m diameter mirror using the laser system ($\eta_{sys} = 25\%$), a warning time of $6T_{\text{A}}$ (1941.36 days), and a thrust period of $\frac{1}{3}T_{\text{A}}$ (107.8 days).

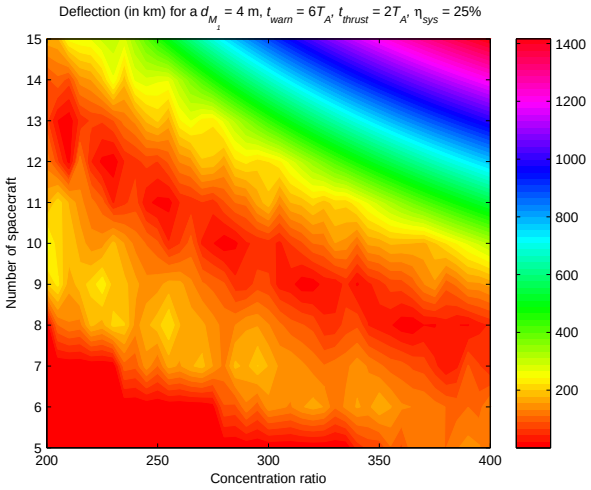

Figure 7.17: Deviation distance for various concentration ratios and number of spacecraft, assuming a 4 m diameter mirror using the laser system ($\eta_{sys} = 25\%$), a warning time of $6T_{\mathrm{A}}$ (1941.36 days), and a thrust period of $2T_{\mathrm{A}}$ (647.12 days).

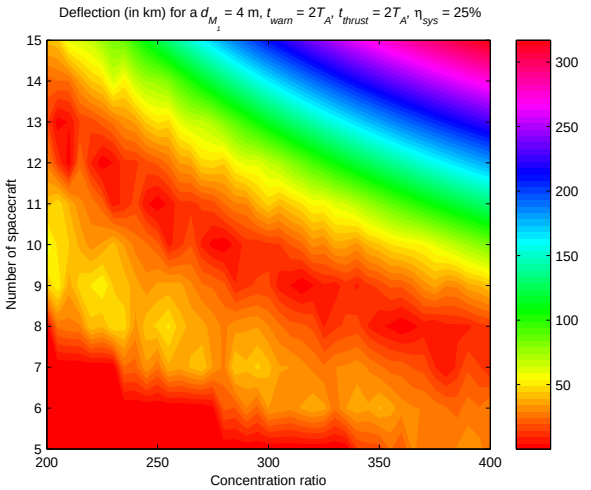

Figure 7.18: Deviation distance for various concentration ratios and number of spacecraft, assuming a 4 m diameter mirror using the laser system ($\eta_{sys} = 25\%$), a warning time of $2T_{\mathrm{A}}$ (647.12 days), and a thrust period of $2T_{\mathrm{A}}$ (647.12 days).

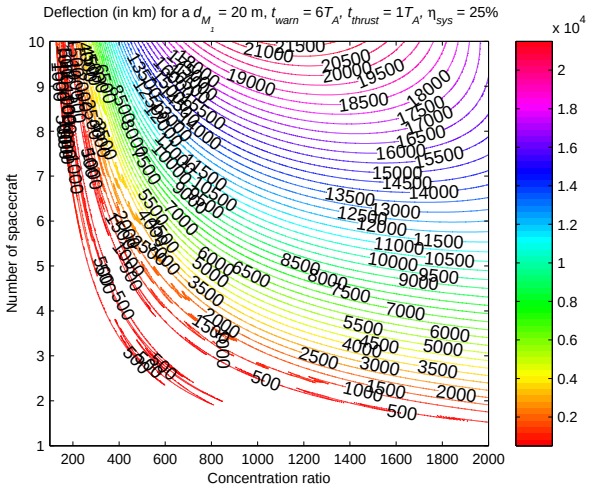

Figure 7.19: Deviation distance for various concentration ratios and number of spacecraft, assuming a 20 m diameter mirror using the laser system ($\eta_{sys} = 25\%$), a warning time of $6T_{\mathrm{A}}$ (1941.36 days), and a thrust period of T_{A} (323.56 days).

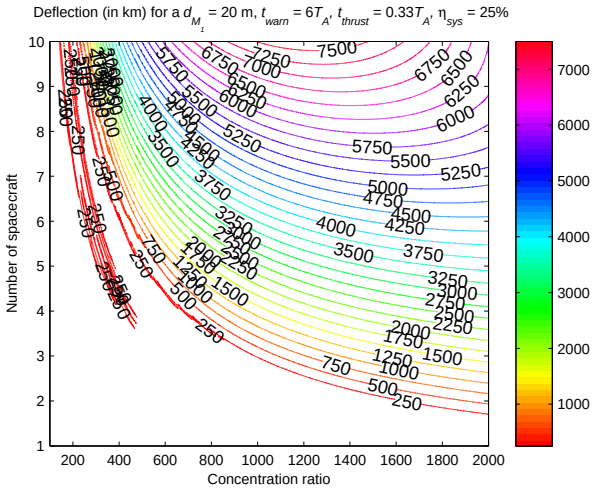

Figure 7.20: Deviation distance for various concentration ratios and number of spacecraft, assuming a 20 m diameter mirror using the laser system ($\eta_{sys} = 25\%$), a warning time of $2T_{\mathrm{A}}$ (647.12 days), and a thrust period of $\frac{1}{3}T_{\mathrm{A}}$ (107.8 days).

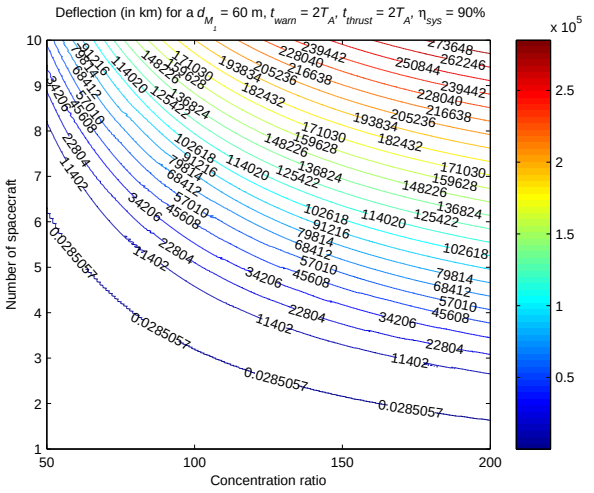

(a)

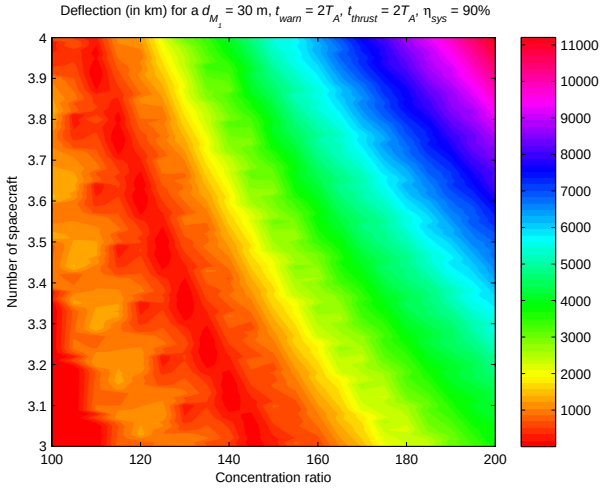

(b)

Figure 7.21: Deviation distance for various concentration ratios and number of spacecraft, assuming a 60 m diameter mirror using direct imaging ($\eta_{sys} = 90\%$), a warning time of $2T_A$ (647.12 days), and thrusting for the entire duration until the MOID (i.e. $2T_A$).

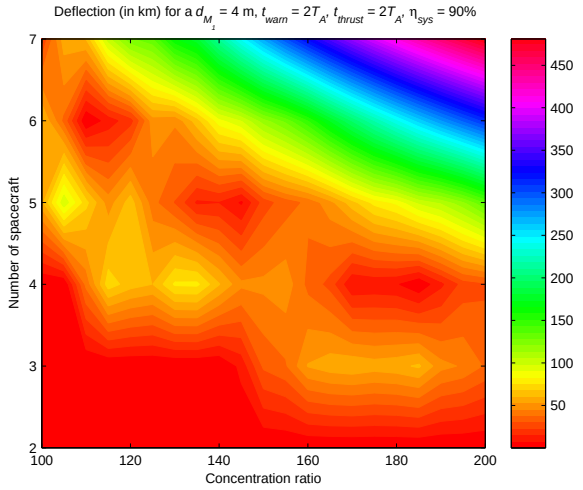

Figure 7.22: Deviation distance for various concentration ratios and number of spacecraft, assuming a 4 m diameter mirror using direct imaging ($\eta_{sys} = 90\%$), a warning time of $2T_A$ (or 647.12 days), and thrusting for the entire duration until the MOID (i.e. $2T_A$).

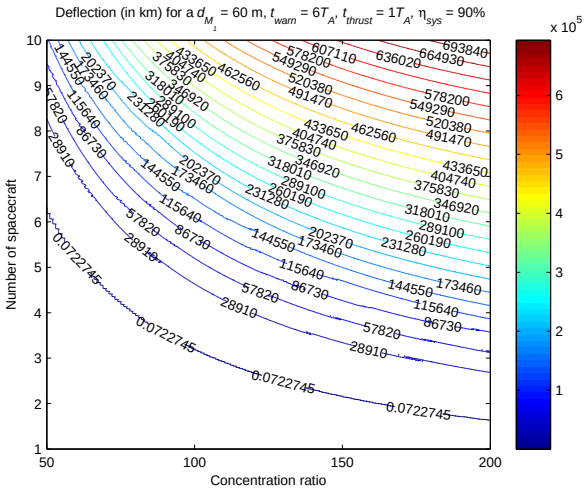

Figure 7.23: Deviation distance for various concentration ratios and number of spacecraft, assuming a 60 m diameter mirror using direct imaging ($\eta_{sys} = 90\%$), a warning time of $6T_A$ (1941.36 days), and thrusting for T_A (323.56 days).

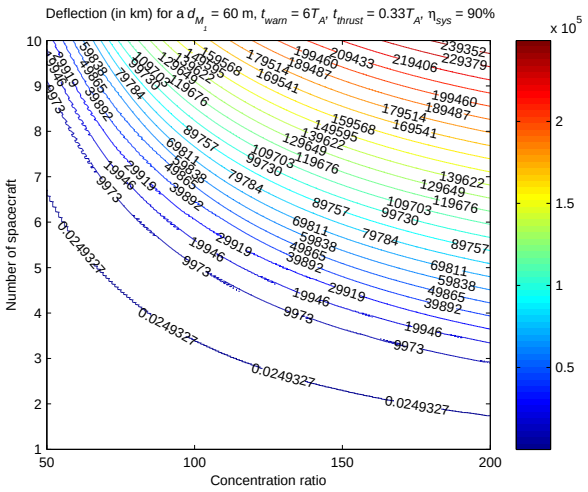

Figure 7.24: Deviation distance for various concentration ratios and number of spacecraft, assuming a 60 m diameter mirror using direct imaging ($\eta_{sys} = 90\%$), a warning time of $6T_A$ (1941.36 days), and thrusting for $\frac{1}{3}T_A$ (107.8 days).

8 Limitations and Improvements

This study addressed some of the problems related to the implementation of the solar sublimation concept for asteroid deflection. They can be summarised as follows:

Orbital dynamics and control in proximity of an irregular body We proved that the mirrors can be maintained at close distance with minimum control. Furthermore, the use of a formation can provide improved orbit determination capabilities both to keep track of the motion of the spacecraft of the spacecraft with respect to the asteroid and of the asteroid with respect to the Sun.

Deployment of a large reflector in space Although the direct imaging concept still requires a reflector of considerable aperture, we demonstrated that a significant deflection can be achieved with reflectors that are one to two order of magnitude smaller than the ones proposed in the literature for this deflection methods. In particular, for the solar pumped laser concept the reflector can be as small as 5 m in diameter. From the preliminary system design we demonstrated that the size and mass of the spacecraft can be within the present launch capabilities. Furthermore the TRL of the individual pieces of technology for the indirect solar pumping is higher than 4 making and is expected to increase regardless the specific application to asteroid deflection.

Contamination of the optics This is probably the most critical aspects and we are going to address this point in the remainder of this section.

8.1 Contamination and Lifetime

Due to the time limitation of this study, it was not possible to develop a new plume expansion model for the sublimation process. Therefore, following analysis relies on the model proposed by Kahle et al. [13].

The model of Kahle is based on some assumptions on the expansion of the plume and on the sublimation process. The first assumption is that the sublimation process is comparable to the generation of jets in comets. The asteroid is assumed to contain a reservoir of material underneath the surface. The gas generated in this reservoir expands through a throat into vacuum.

The second assumption is that the plume expansion is similar to the expansion of gas of a rocket engine outside the nozzle. The density of the gas can be computed with the following analytical formula,

$$\rho(r,\Theta) = \rho^* j_c \frac{d_{spot}^2}{(2r+d_{spot})^2}\left(\cos\left(\frac{\pi\Theta}{2\Theta_{max}}\right)\right)^{\frac{2}{k-1}} \tag{8.1}$$

where r is the distance from the spot on the surface of the asteroid, d_{spot} is the illuminated spot diameter, Θ is the elevation angle of the spacecraft with respect to

the y axis of the asteroid Hill reference frame $\mathcal{A}$ ($\Theta = 0^\circ$ means the spacecraft is along the y axis, while $\Theta = 90^\circ$ means it is along the x). The jet constant j_c was taken equal to 0.345 and the maximum expansion angle $\Theta_{max} = 130.45^\circ$. These are empirical values that need to be verified and can be substantially different in the case of the sublimation of an asteroid. However, in this section we will use these values for comparison with the results of Kahle et al.

The value ρ^* is the density at the sublimation point and in our model is computed as the total mass flow $\dot{m}_{exp}$ divided by the product of the spot area A_{spot} and gas exhaust velocity v_{gas},

$$\rho^* = \frac{\dot{m}_{exp}}{(A_{spot} v_{gas})} \tag{8.2}$$

If the expression for ρ^* is substituted into (8.1) we get,

$$\rho(r, \Theta) = \frac{4\dot{m}_{exp}}{\pi v_{gas}} j_c \frac{1}{(2r + d_{spot})^2} \left(\cos\left(\frac{\pi\Theta}{2\Theta_{max}} \right) \right)^{\frac{2}{k-1}} \tag{8.3}$$

This model predicts that the density at a given distance r is mildly dependent on the size and geometry of the spot. In particular the maximum expansion angle is not a function of the spot geometry. It can be argued that in the case of an extended body which is an order of magnitude bigger than the spot, the expansion cone is probably different from the one reported in the work of Kahle.

The third assumption is that all the particles impacting the surface of the mirror condense and stick to the mirror. The flow of particles per unit area is given by $\rho(r, \Theta) v_{gas}(\rho)$ where the velocity of the particles is assumed to be independent of the spacecraft elevation angle Θ.

Kahle assumes that the mirror is perpendicular to the flow and that the density of the condensed material is $\rho_{layer} = 1$ g/cm^3 therefore, for the conservation of the mass the height of the condensed material is,

$$h_{cond} = \frac{\rho(r, \Theta)\, v_{gas}(\rho)}{\rho_{layer}} t_h \tag{8.4}$$

and the time t_h to reach a given thickness is easily computed as

$$t_h = \frac{h_{cond} \rho_{layer}}{\rho(r, \Theta)\, v_{gas}(\rho)} \tag{8.5}$$

The contamination time, therefore, is inversely proportional to the mass flow, while the thrust is directly proportional to the mass flow. In our model the exhaust velocity is constant and function of the sublimation temperature, therefore the thrust depends only on the mass flow. A higher thrust results in a higher mass flow and thus in a faster contamination.

However, as presented in Fig. 8.1 in the case of the solar pumped laser, the spacecraft has a 'dancing-ballerina' configuration with the primary mirror never facing the asteroid or the plume. In particular for more than half of the orbit the primary mirror is shielded by the spacecraft itself. The steering mirror, on the other hand, though it is in the plume, it is not perpendicular to the flow. Following the approach used to compute the contamination of surfaces due to outgassing we can add a view factor to (8.5),

$$t_h = \frac{h_{con} \rho_{layer}}{\rho(r, \Theta) v_{gas}(\rho) \sin\Theta_2} \tag{8.6}$$

where Θ_2 is the angle between the laser beam and the surface of the steering mirror, e.g. if the laser beam is parallel to the y axis, Θ_2 is 45°. Note that the primary mirror is protected not only from the flow of gas but also from the debris. As the gas expands its velocity increases till it reaches the free molecular flow state, at that point, following the assumption of Kahle, we considered the velocity constant. Since

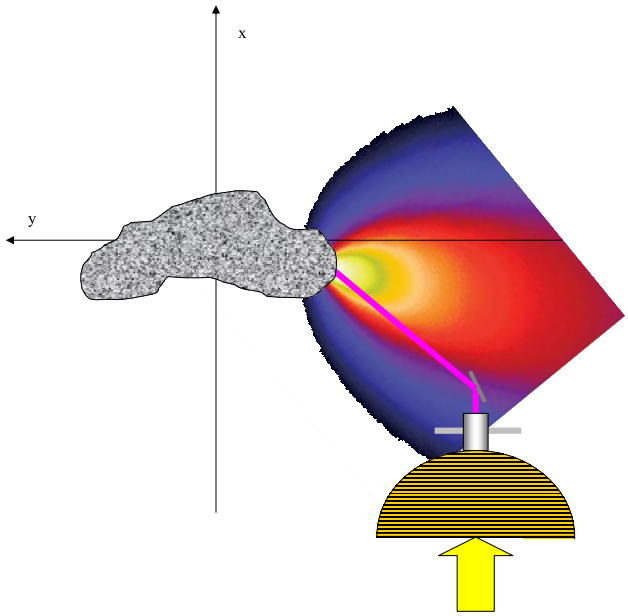

Figure 8.1: Cartoon of the plume-spacecraft interaction for the case of the solar pumped laser.

in our model the temperature is 1800 K, the initial velocity is 550 m/s and in 1.3 m it doubles. At that point the Knudsen number is about 1 and from that moment on the gas can be considered in free molecular state. Note that, although in (8.6) the velocity is considered to be directed toward the mirror, in reality the velocity field will present more scattered directions of motion.

Another important consideration is that the gas flowing toward the steering mirror is continuously illuminated by the laser beam, therefore either the wavelength of the laser is such that there is no interaction or the gas is not cooling down but is further heated up. The additional heat will further expand and likely ionise the gas. If the gas is ionised a simple electrostatic field would maintain the mirrors clean. If the gas is not ionised, since it is not cooling down a condensation is less probable.

Assuming that the gas is actually condensing on the surface of the mirror, the condensed layer will be constantly illuminated by the laser, therefore either it is not absorbing the light of the laser or it is heated up and will evaporate again. Thus, it is possible that the laser system is also keeping the mirrors clean (as it happens in the ignition system of some experimental car engines).

Figures 8.2–8.4 represent the deflection that can be achieved assuming that the system can operate only until the steering mirror is completely contaminated. Therefore, although the warning time is increasing the push time depends on the lifetime of the mirror. For the contamination the simulations are using the model in (8.6) and (8.4) and assume that the gas flow corresponds to the maximum sublimation point (maximum ejection of material). The asteroid is pushed continuously till the mirror cannot be operated due to the contamination. This is not an optimal strategy, as shown in Colombo and Vasile (2009) [1] but it will serve here as an illustrative example.

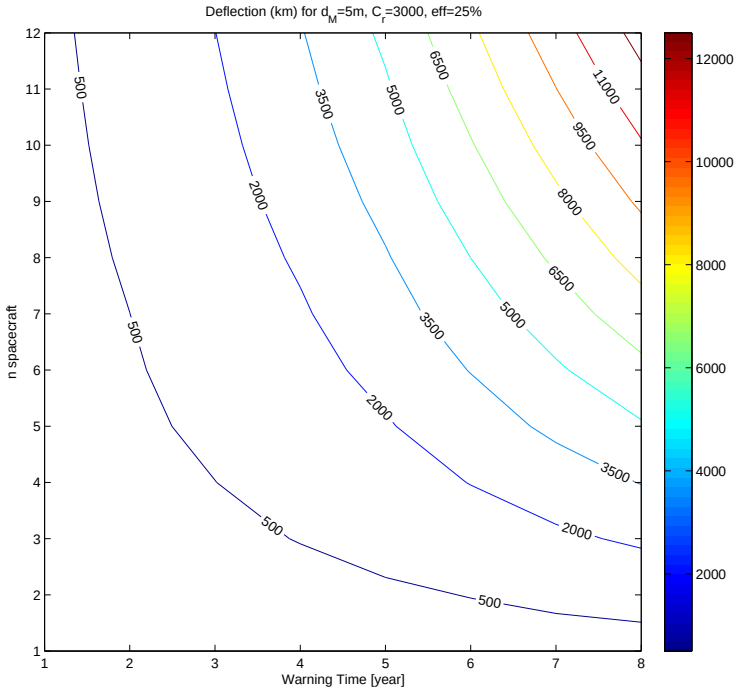

Figure 8.2: Deflection as a function of the warning time and number of satellites, including mirror degradation. Aperture of the primary mirror is 5 m.

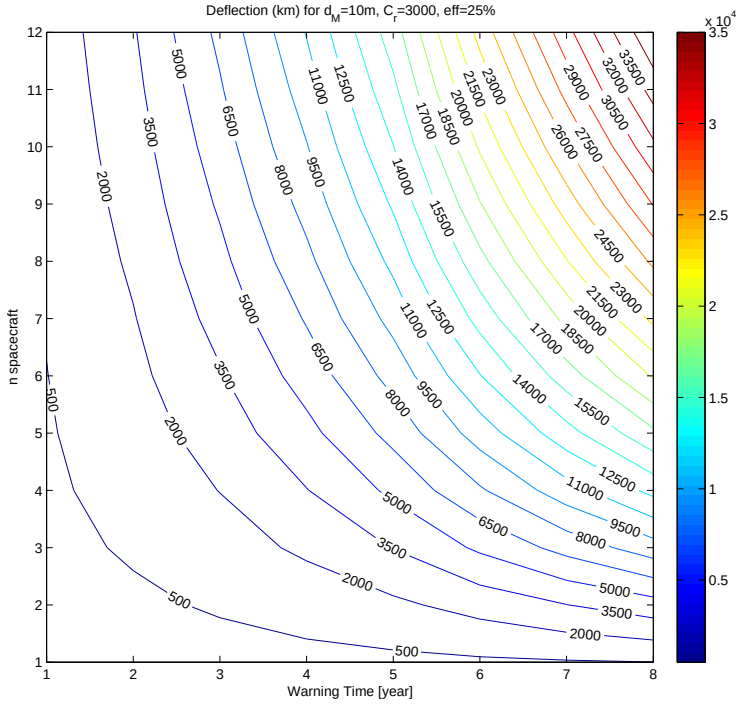

Figure 8.3: Deflection as a function of the warning time and number of satellites, including mirror degradation. Aperture of the primary mirror is 10 m.

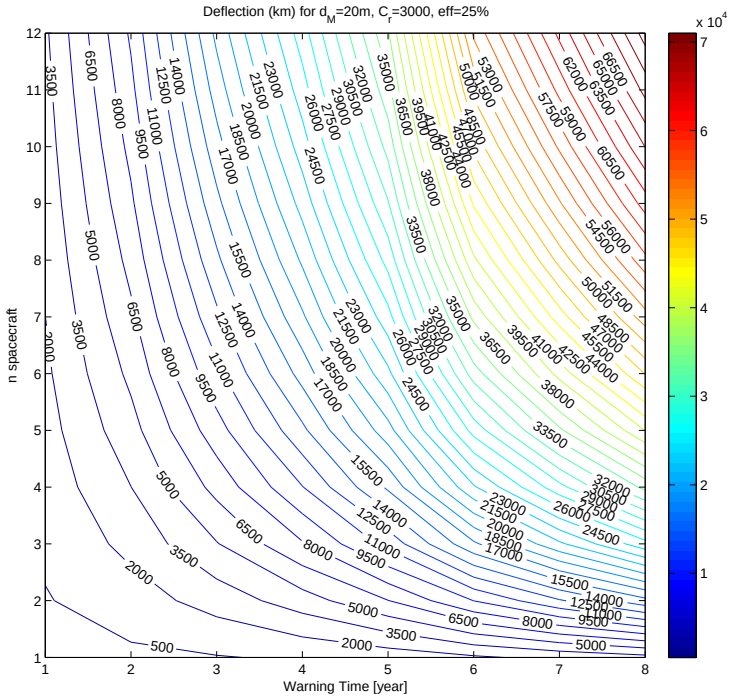

Figure 8.4: Deflection as a function of the warning time and number of satellites, including mirror degradation. Aperture of the primary mirror is 20 m.

8.2 Possible Improvements

We conclude this section with few possible suggestions for an improvement of the overall concept. Note that the calculations performed in this study did not aim at an optimisation of the performances. For example the mass of propellant required for the transfer, that now is estimated as 40% of the dry mass, can be largely reduced.

Another possibility to reduce the mass of the spacecraft is to use frequency selective mirrors. In fact a substantial part of the mass of the spacecraft is made of the cooling system of the solar panel which can range between 15% to 27% of the dry mass of the spacecraft for a 5 m and 10 m diameter mirror, respectively. The idea is to let the mirror absorb the part of the spectrum that the solar cells are not using.

For the contamination problem the solar pumped laser option offers a range of possible solutions which can be explored. The primary can be further protected by shielding the exterior part of the spacecraft and by adding baffles along the rim of the mirror. The steering mirror can be protected using a counter flow of inert gas, though this solution would require extra mass, and a shutter that is timed with the flow of debris and gas.

However, if the laser interacts with the plume, or even if the surface of the mirror is kept at high temperature, the system could be potentially self-cleaning. In fact the average time of residence of a contaminant on a surface can be estimated as, [53],

$$\bar{t}_{res} = \tau_0 \exp^{E_a/\bar{R}T_{\text{M}}} \tag{8.7}$$

where τ_0 is oscillation period of molecule, and $\bar{R} = 8.314472$ J/K·mol is the gas constant. If the temperature T_{M} of the mirror or layer of material is kept high, most of the contaminants with a low activation energy E_a could sublimate again after a few

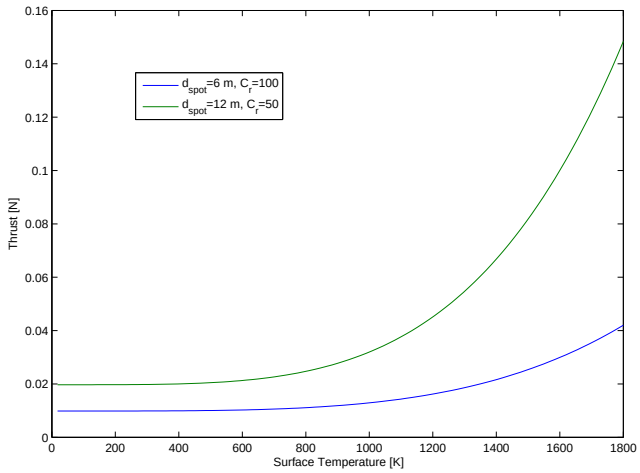

Figure 8.5: Total thrust due to combined Yarkovsy and solar pressure effects.

seconds of residence.

The absorption of the laser beam by the plume also means a reduction in the power density on the surface. A reduction of the power density would correspond to an interruption of the sublimation process. As the sublimation stops, the plume would dissipate quite fast and the laser would be able to sublimate again. Therefore, the overall system would work through a sequence of impulses. These impulses can be timed with the duty cycle of the laser to maximise performance.

As stated above the current computation of the deflection is not optimal. As shown in Colombo and Vasile (2009) [1], a proper scheduling of the thrusting operations would greatly increase the deflection. In particular, thrusting around the perihelion for deflection strategies that are pushing in the direction of the velocity is optimal while for other values of the true anomaly the deflection action is not very effective.

Although pushing only at the perihelion would increase the warning time, it would also mitigate the contamination problem extending the lifetime.

The direct imaging system may represent a problem if the optics cannot be protected. It is expected that the flow of gas will be excited by the flux of light and therefore will not condense as the model of Kahle predicts. On the other hand the flux is not dense enough to sublimate the debris, which may represent a severe problem. Therefore, the study of the optical system and of the contamination of the optics in the case of the direct imaging remains an open problem.

8.2.1 Enhanced Yarkovsky Effect

The direct imaging concept offers an interesting possibility. If the power density is not enough to sublimate the surface material, it can be anyway sufficient to heat up the surface.

Let us assume that the reflectivity σ_{M} is 0.2, the absorptivity is $\alpha_{\text{A}} = 0.8$ and the emissivity is $\epsilon_{\text{A}} = 0.9$. Then given a reflector with a diameter of 60 m, a spot size diameter d_{spot} and a concentration ratio C_r, we get that the simple force due to the light projected onto the asteroid is,

$$F_{light} = 2(1-\alpha_{\text{A}})\sigma_{\text{M}} C_r \pi \frac{d_{spot}^2}{4} P_0 \left(\frac{r_{AU}}{r_{\odot/sc}}\right)^2 + \alpha_{\text{A}}\sigma_{\text{M}} C_r \pi \frac{d_{spot}^2}{4} P_0 \left(\frac{r_{AU}}{r_{\odot/sc}}\right)^2 \quad (8.8)$$

where $P_0 = S_0/c$ given in (4.13). The first component is the reflected light and the second component is the absorbed light.

On top of this, if the surface temperature is T, then the emission of photons will add the force component [54],

$$F_{ir} = \frac{2}{\pi}\frac{\epsilon_{\text{A}}\sigma T^4}{c}\pi\frac{d_{spot}^2}{4} \tag{8.9}$$

The temperature of the spot surface can be computed with the simple one-dimensional model,

$$\chi\frac{\partial^2 T}{\partial x^2} = \frac{\partial T}{\partial t} \tag{8.10}$$

where

$$\chi = \frac{K_{\text{A}}}{\rho_{\text{A}} c_{\text{A}}}$$

is the thermal diffusivity of the material, $K_{\text{A}} = 2$ W/m/K is the conductivity, $\rho_{\text{A}} = 2$ kg/m^3 is the density of the material and $c_{\text{A}} = 750$ J/kg/K is the heat capacity [8]. The boundary conditions are then,

$$-K_{\text{A}}\frac{\partial T}{\partial x} + \epsilon_{\text{A}}\sigma T^4 = \alpha_{\text{A}}\sigma_{\text{M}} C_r \pi\frac{d_{spot}^2}{4} S_0\left(\frac{r_{AU}}{r_{\odot/sc}}\right)^2 \tag{8.11a}$$

$$T(0, x) = T_0 \tag{8.11b}$$

$$T(t, L) = T_0 \tag{8.11c}$$

The initial temperature T_0 is taken to be 278 K [8] and we considered that the internal temperature, at distance $L = 50$ m from the surface is constantly 278 K. A scattering factor Λ of $2/\pi$ is multiplied by the total force to account for emissions in all directions on a dome. Figure 8.5 shows the sum of the two force components as a function of the surface temperature for two different spot sizes. Note that this total force is comparable to the one exerted by a gravity tug of 5000 kg (see Sanchez et al. [8] for more details).

Figure 8.6 shows the deflection that can be achieved with the simple combination of forces given in (8.8) and (8.9), for two illustrative examples.

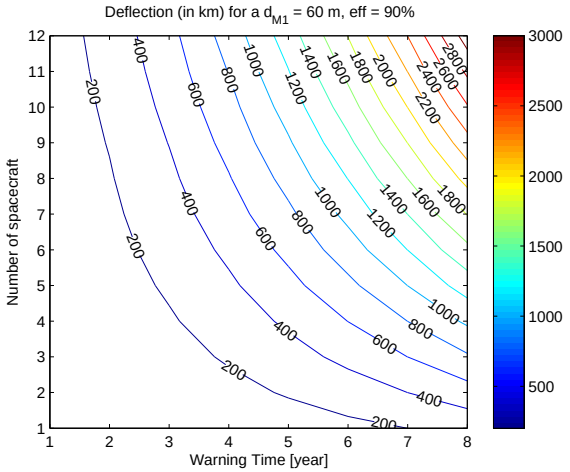

(a) Solar collector with a 60 m aperture diameter and a concentration ratio of 34.

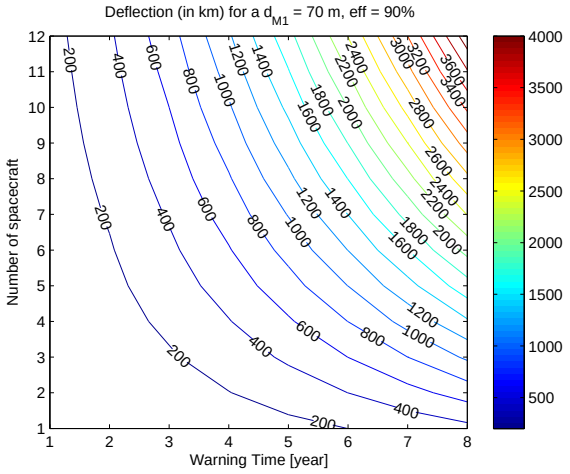

(b) Solar collector with a 70 m aperture diameter and a concentration ratio of 34.

Figure 8.6: Deflection achievable with the enhanced Yarkovsy effect.

9 Roadmap

The following roadmap contains the required steps to put a NEO-defence system based on solar concentrators (also referred to as Mirror Bees in this report) into space. The roadmap contains a number of fundamental steps toward the implementation of the Mirror Bees and a description of the technologies that are currently under development independently of the development of the Mirror Bees but are essential for their implementation.

The roadmap contains the fundamental steps for the implementation of both concepts presented in this report. Note that their development has commonalities but some key elements are expected to follow substantially different development paths. In particular, the development of efficient semiconductor lasers or high efficiency solar cells is relevant for many fields of application not related to space. It is therefore likely that the key components of the laser concept will be developed independent of the development of the mirror bee concept.

By 2029 it is expected that the following key technologies will be fully developed independent of the Mirror Bee concept:

- High efficient solar arrays with a total efficiency of 40% or higher. See for example the current research in this direction [28, 55]
- High efficiency semiconductor laser, electrically pumped, with efficiency of 70% or higher. See the current results of Alfalight* and nLight†.
- Directly solar pumped laser with an efficiency up to 35%. Although it is more likely that the research in electrically pumped semiconductor lasers and in highly efficient solar cells will progress faster then the one in directly pumped solutions, the reduced complexity of a directly pumped system may suggest an independent stream of research in this direction for many different applications.
- Accurate orbit determination of satellite formations in deep space, with a mean error lower than 100 m in position.
- Autonomous swarm control.
- Development of light-weight high-efficiency cooling system for space.

Furthermore, it is expected that the knowledge of the following main characteristics of Apophis will be improved or available:

- Knowledge of the orbit of Apophis. This is not strictly required but a good knowledge of the orbit of Apophis is expected in order to take a decision on whether the asteroid is actually impacting the Earth or not. This applies to any threatening asteroid.

The beauty of the Mirror Bees concept is that most of the technologies required for the implementation of the Bees are expected to be fully developed by 2029, independent of the actual development of the Bees. In fact, many other applications

*http://compoundsemiconductor.net/cws/article/news/19664

†http://www.nlight.net/news/releases/41~nLIGHT-Demonstrates-73-WallPlug-Efficiency

exist that require similar developments, with many space missions already planned or scheduled for launch before 2029 such as TechSat21 and LISA, as well as the research into solar powered satellites. However, a better knowledge of the characteristics of the asteroid Apophis would be desirable. In particular:

- Three dimensional map of the surface of the asteroid
- Measurement of the rotational state
- Knowledge of the morphology and composition of Apophis. In particular the geometric characteristics of the ellipsoid enclosing the asteroid, the absorptivity bands of the surface material and the conductivity of the subsurface material.

Furthermore a number of technologies specific to the implementation of the Mirror Bees concept would be required. In particular:

- Deployment and control of large, lightweight, flexible structures into space.
- Adaptive control of the optics of the mirror and mirror assembly (shape control)

9.1 Fundamental Steps toward the Mirror-Bees concept

9.1.1 Step 1: Detailed Feasibility Study

The initial effort to assess the feasibility and optimality of the Mirror Bee concept [1, 8, 56, 57, 36, 14, 58, 59], suggested that the use of a solar concentrator is extremely competitive against a number of existing deviation methods (i.e. nuclear blast, kinetic impactor, low-thrust propulsion, mass driver).

This report can be seen as a first preliminary analysis. Although some fundamental questions have found an answer, like where to place the spacecraft, other questions still remain open. In particular the following issues require a conclusive answer:

- From this preliminary analysis it appeared that a simple optical system could not provide the required collimation due to the angular aperture of the Sun disk. However, more investigations are required to rule out this possibility. Note that at a distance from the Sun farther away than 1 AU a greater concentration/collimation can be achieved since the light rays get progressively more an more parallel. Therefore, paradoxically, such a system would be suitable for deflection actions far away from the Sun.
- Navigation and attitude dynamics for the direct imaging system where not addressed in this study due to the limited time. Although the navigation for this concept should be easier than in the case of the funnel orbits, an analysis is required.
- For both the direct imaging and the laser concept it is required to close the loop between navigation and orbit/attitude control to verify that the spacecraft can maintain the fix on the target spot on the surface of the asteroid.
- a More detailed system design analysis is required. In particular there was no time to go through a complete trade off analysis of all the possible options in terms of number and size of the spacecraft.

A detailed feasibility study is therefore required to obtain a detailed design of the mirrors, the spacecraft and the whole system. The detailed feasibility study aims at:

- Analysing the deployment and control of the formation. In particular, accurate orbital and attitude control of the mirror assembly in order to superimpose the beams and guarantee the required power density on the surface of the asteroid.

- Developing the required level of autonomy and control for each individual spacecraft and for the formation.
- Computing a detailed system budget for each individual spacecraft and for the formation.
- Detailed modelling of the sublimation process.
- Computing an accurate estimation of the deviation action and achievable variation of the MOID.
- Defining the adaptive optics for the direct imaging concept.
- Producing a detailed design of the laser system both for the case of the direct and indirect pumping.

9.1.2 Step 2: Lab experiments of the sublimation process

The physical principle behind the mirror bees idea is the sublimation of the surface material of an asteroid, induced by a high energy light beam. The power density required to generate the sublimation of the surface material can be generated either with a solar concentrator or laser. Given the correct power density at a given radiation frequency, the sublimation process can be reproduced and tested in a lab.

A campaign of lab tests is already ongoing as part of the preliminary feasibility study. The laboratory tests use a CO_2 laser capable of delivering the required power density ($5.058E5$ W/m^2). Different rocks of different composition and porosity are used in the tests. These tests aim at measuring: the scattering factor due to the inhomogeneous morphology and composition of the surface, the rate of expelled material for a given power density, and the total change in linear and angular momentum. During the experiment, the sample is located in a vacuum chamber. A high speed camera records the plume of expelled material, and a weight scale is used to measure the mass of expelled material and the induced thrust. The rotational state of the asteroid is reproduced by spinning the sample.

9.1.3 Step 3: Development of ultra light adaptive structures for the mirror

A key technology for the implementation of the Mirror Bee concept is the deployment and control of the mirrors. Although the bees only require a relatively small mirror, a deployable light-weight structure would be required. This structure would also be required to actively control the focal point (shape) of the mirror. The deployment of ultra-lightweight adaptive structures is a technology that is already under development for other applications. We expect that before 2029, the technology will have reached the required stage of maturity and can be used to build the Bees.

The following lists some reference material on the current state of the art:

- ESA Inflatable Structures for Space Systems – Approved Activities, `http://mechanical-engineering.esa.int/structures/inflatableactivities.html`
- ESA News: Expanding Frontiers, Intelligent textiles for large space structures, `http://www.esa.int/esaCP/SEMB8W5TI8E_Expanding_0.html`
- Composite ultra-light weight active mirror for space applications, United States Patent 7064885.
- A new deployable thin-film, ultralight mirror for future space telescopes and surveillance satellites, *Science* **79**(1), July 2000.
- Stretched membrane with electrostatic curvature (SMEC): A new technology for ultra-lightweight space telescopes, Angel R., Burge J., Hege K., Kenworthy M., Woolf N., *SPIE Proceedings* **4013**, 2000.

- Gossamer Sailcraft Technology: Membrane/Inflatable Structures Technology for Space Applications, Salama, M., McInnes, C.R., and Mulligan., P., *AIAA Progress in Astronautics and Aeronautics* **191**, 2001.
- Solar sail technology development and demonstration, M. Leipold, M. Eiden, C. E. Garner, L. Herbeck, D. Kassing et al., *Acta Astronautica* **52**(2–6): 317–326, 2003.
- The Deployment Experiment of Solar Sail with a Sounding Rocket, Nishimura Yusuke, Tsuda Yuichi, Mori Osamu, Kawaguchi Junichiro, Proceedings of the *55th International Astronautical Congress*, Vancouver Canada, October 2004, pp. 1–8.

9.1.4 Step 4: Development of a solar pumped laser system

A directly pumped system is currently far from having the required efficiency. A system with 4-6% of efficiency (from solar power to laser output power) would require an excessive number of satellites and an excessive mass of the cooling system. The target is to reach an overall efficiency of 40% or more.

At present the combination of solar arrays and semiconductor laser seems to be closer to the target, achieving already wall plug efficiencies, in labs, of up to 20% for the whole system. Translating the current technology to a space system capable of several hundred kW of output power is not an easy task. Semiconductor laser can currently reach few kW of output power, therefore 100 kW system would require to stack up several semiconductor laser. Although possible, it represent an engineering challenge.

Furthermore, the quality of the beam will have to be improved to be able to hit a surface of 1-3.14 m^2 at 2 km or more as proposed in this study. Even in this case such an optical system is possible though it requires some development.

9.1.5 Step 5: Development of the required autonomy for the control of the swarm of bees

In parallel with the development of the technology for the deployment and control of the mirror assembly, the technology for the control of the formation will also be developed. In particular, this step includes: the development of an optical navigation system to control the beam pointing, the beam size and the position of the satellites with feedback on the achieved spot size and the induced acceleration, orbit determination for the spacecraft and the asteroid during the deviation operations, orbit and attitude maintenance. A lot of work has already been done on the control of formations and swarms and we expect an advanced development of this technology for a number of future application.

The following lists some reference material on the current state of the art:

- Vortex Formation in Swarms of Interacting Particles, McInnes, C. R., *Physical Review E* **75**(3), 2007.
- Pattern Transition in Spacecraft Formation Flying via the Artificial Potential Field Method and Bifurcation Theory, Bennet, D. J., McInnes, C. R., Proceedings from *3rd International Symposium on Formation Flying, Missions and Technologies*, ESTEC/ESA Noordwijk Netherlands, 23–25 April 2008.
- On-Orbit Assembly Using Superquadric Potential Fields, Badawy, A., McInnes, C. R., *Journal of Guidance, Control and Dynamics* **31**(1): 30–43, 2008.
- Autonomous and Distributed Motion Planning for Satellite Swarm, Izzo, D., Pettazzi, L., *Journal of Guidance Control and Dynamics* **30**(2): 449–459, 2007.

- Use of Swarm Intelligence in Spacecraft Constellations for the Resource Exploration of the Asteroid Belt, Curtis, S. A., Rilee, M. L., Clark, P. E., Marr, G. C., Proceedings from the *3rd International Workshop on Satellite Constellations and Formation Flying*, Pisa, Italy, 2003.
- NASA's Swarm Missions: The Challenge of Building Autonomous Software, Truszkowski, W., Hinchey, M., Rash, J., Rouff, C., *IEEE Computer Society: IT Pro*, September/October 2004, pp. 47–52,

9.1.6 Step 6: Prototyping

Development of the mirrors assembly and of the deployment system. Once the detailed feasibility analysis is completed, an engineering prototype of the mirror assembly can be developed. In particular, the laser system, the adaptive shape of the mirror and the deployment system have to be designed and developed.

9.1.7 Step 7: On ground testing of the mirror bees concept

A test campaign on the ground is required to test the following pieces of technology:

Deployment and maintenance of the solar concentrator. The reflector is required to be supported by a lightweight structure. At the same time the shape and curvature of the mirror has to be maintained during the entire operation cycle. If MEMS are used to control the shape of the mirror, the control of the shape has to be tested after deployment.

Adaptive optics control. Besides the control of the shape of the mirror, the collimation of the beam has to be tested. The collimation can be achieved through an adaptive series of lenses which have to be deployed and controlled. The collimation has to be maintained, within a relatively small tolerance, over a distance of several kilometres. The control of the focal point of the mirror is also a key technology in maintaining the required pointing accuracy.

Sublimation process due to radiation over the range of the solar spectrum. A number of test sites have already been identified (e.g. Las Palmas). This test campaign has the additional advantage of testing a spin-off of the mirror bees technology: a portable (or transportable) power generation device. Other military applications are possible, and were recently proposed however by personal choice are not covered in this proposal. The limits of this tests are: the presence of the atmosphere along the beam path (dissipation and diffraction effects) and around the surface of the sample (combustion process not existing in space), the gravity acceleration that influences the deployment of the mirror and the maintenance/control of its shape.

9.1.8 Step 8: Sounding Rocket Experiment

The first sub-orbital experiment to test the deployment of the mirror. In particular, the mission has the following key objectives:

- Deployment of the mirror assembly in microgravity,
- Measurement and verification of the curvature/shape of the mirror after deployment.

9.1.9 Step 9: LEO deployment experiment

The first in-orbit experiment to test the deployment of the mirror and formation. In particular, the mission has the following key objectives:

- In-orbit deployment of the mirror assembly
- In-orbit control of the mirror and of the adaptive optics
- In-orbit deployment and control of the formation (two satellites)
- Accurate beam pointing
- In orbit testing of the laser system

9.1.10 Step 10: NEO sample return mission

Second technology demonstrator. The mission aims at assessing the effectiveness of the solar sublimation concept in the final operational environment. Other key objectives of the mission are:

- Provide a three dimensional map of the surface of the asteroid
- Return a sample(s) of the surface material
- Test the coordination and controls of the Bees
- Test the deployment of the mirror and formation
- Test the direct imaging system or the laser system

The mission can be composed of 2 to 4 satellites, out of which one is carrying an aerogel collector similar to the one used onboard the mission Stardust. The other satellites will carry the mirrors and will create an artificial comet tail. The satellite carrying the aerogel will fly in the plume and collect samples of the gas and debris coming from the asteroid.

9.1.11 Step 11: LEO applications of the mirror bees concept

An interesting aspect of the mirror bees concept is that it has several possible applications and spin-offs that do not require a conceptual re-design of the spacecraft or formation. Before using the formation as an actual deflection device, the satellites could be employed for a number of terrestrial applications. These applications have the dual advantage of making the system cost effective and ready-to-use. We list two possible applications.

Environmental control This application, suggested by a number of people, is in line with the effort of the Russians to increase the illumination of some portions of their territory. Solar concentrators can be used for the same application, or for increasing the irradiance of some layers of the atmosphere, or portions of the surface of the Earth (land or ocean). The increased irradiance would locally alter the climate, influencing the agriculture and could modify/control some natural phenomena [60].

LEO power generation This application is in line with the current efforts to produce power from space. Once the effectiveness of the use of adaptive optics to maintain a collimated beam is proven, a formation of solar concentrators can be used to directly beam solar energy down to Earth or to an orbital energy conversion system, e.g. thermo-power generator or photovoltaic device. Note that though the satellites used for one of these applications might not be able to be re-used in the case a deflection mission is needed (mainly due to a lack of propellant or a degradation of the optics), nonetheless no new design and development is needed and manufacturing a new formation of satellites (all identical) would be relatively fast.

9.1.12 Step 12: NEO interception and deflection

The need for a deflection mission is contingent upon the results from Apophis' resonant flyby of the Earth in April 2029. If required, the Mirror Bees would then be launched on an intercept mission. Even if Apophis avoids the keyhole and is no longer considered an imminent threat, it still represents an interesting mission for the examining the performance of this deviation method for future NEOs.

10 Conclusion

In this report we presented a preliminary analysis of an asteroid deflection method called Mirror Bee. In particular this document contains the result of a short 4 moth study that addressed a number of potential show stopper for this deflection approach.

The Mirror Bee concept is a response to the criticisms against the original idea of Lunan and Melosh of using a solar concentrator to generate a thrust by sublimating part of the surface of an asteroid:

- Impingement of the solar collector with the plume of gas and debris coming from the asteroid
- Problematic control of the collector in the proximity of an irregular body

Furthermore, it gives a partial answer to the technological requirements to put this concept into space by 2029.

Two configurations for the mirrors were analyzed and for each one a different strategy for orbit maintenance was considered. In particular, the dual-mirror configuration led to the definition of a particular set of formation orbits composing two symmetric funnels with the principal axis aligned with the y-axis of the Hill reference frame. These funnel orbits allow the spacecraft to have a very good visibility of the target spot on the surface of the asteroid and at the same time allow room for the plume of gas to flow with minimal impingement. The funnel orbits are located outside a limiting sphere where the gravity field of the asteroid can be considered homogenous. This limit sphere imposes requirements on the pointing accuracy and focusing capabilities of the mirror assembly. The orbital maintenance strategy is based on the computation of the control components that minimize the difference between the current and target value of the relative Keplerian elements.

The control compensated for two sources of perturbations: solar radiation pressure due to the large surface area of the mirror assembly and third body effects due to proximity of Apophis, and for the constantly deviating orbit of the NEO. The decrease in mass of Apophis due to the solar sublimation was also accounted for. The control is only required for the duration of the mission, in this case to amount of time necessary to achieve a deviation distance equal to the Earth-Moon separation.

A second option considered a single-mirror configuration. For this option, the mirror can be placed at artificial equilibrium points highly inclined over the y-axis of the Hill frame. From this position the spacecraft sees the target spot from a high angle, however AEPs can be found that allow the spacecraft to maintain a reasonable size of the spot area. A control strategy was proposed that allows the spacecraft to oscillate in a confined region in the proximity of the asteroid with a very low control thrust. Even adding the effect of the gravity field of an elongated body, the magnitude of the required control thrust remains limited. The low level of thrust would suggest the use of FEEP engines, which would lead to a minimal propellant consumption even over long operation times.

The results in this report shows that the Mirror Bee concept is an effective solution to the drawbacks of the original idea of a solar sublimation system. However many key points remain open. For example, though we demonstrated that a simple optical

system cannot collimate the light of the Sun at the required distance from the asteroid, the arguments in this report are not conclusive and more investigations are required. Furthermore, the system design analysis is only partial and does not include any trade off between number of spacecraft, achieved deviation, warning time and overall system mass. The design of the bees, therefore, has large margins for improvement.

We would like to underline that this report does not claim in any measure that the solar sublimation technique or the Mirror Bee concept are the right solution to deflect asteroids. On the other hand, the more we study this idea in detail, the more we discover, with surprise, its potential. The more we look for show-stoppers, the more we find good reasons for a further development of this idea.

Last but not least, the deflection of asteroid seems to stimulate the imagination of many scientists and the plethora of deflection methods continuously proposed by several people, would make any science fiction writer or every film maker extremely happy. On the other hand, at present, apart from foraging the science fiction industry there are no technical reasons that would suggest that new deflection methods are needed. In fact the depth of the analysis of existing method is still very shallow, often based on oversimplified theoretical considerations, and not sufficient to rule out most of them.

References

[1] Colombo, C., Vasile, M., and Radice, G., Semi-analytical solution for the optimal low-thrust deflection of Near-Earth Objects, *Journal of Guidance, Control and Dynamics* **32** (2009): 796–809.

[2] Vasile, M. and Colombo, C., Optimal impact strategies for asteroid deflection, *Journal of Guidance, Control and Dynamics* **31** (2008): 858–872.

[3] Izzo, D., On the deflection of potentially hazardous objects, in *15th AAS/AIAA Space Flight Mechanics Conference*, Copper Mountain, Colorado, 2005.

[4] Scheeres, D. J. and Schweickart, R. L., The mechanics of moving asteroids, in *Planetary Defense Conference*, Orange County, California, 2004, AIAA.

[5] Conway, B., Near-optimal defection of Earth-approaching asteroids, *Journal of Guidance, Control and Dynamics* **24** (2001): 1035–1037.

[6] Carusi, A., Valsecchi, G. B., D'abramo, G., and Bottini, A., Deflecting NEOs in route of collision with the Earth, *Icarus* **159** (2002): 417–422.

[7] Hall, C. D. and Ross, I. M., Dynamics and control problems in the deflection of Near-Earth Objects, *Advances in the Astronautical Sciences* **67** (1997): 1–18.

[8] Sanchez Cuartielles, J. P., Colombo, C., Vasile, M., and Radice, G., Multi-criteria comparison among several mitigation strategies for dangerous near earth objects, *Journal of Guidance, Control and Dynamics* **32** (2009): 121–142.

[9] Sanchez Cuartielles, J. P., Vasile, M., and Radice, G., On the consequences of a fragmentation due to a NEO mitigation strategy, in *International Astronautical Congress (IAC-08-C1.3.10)*, Glasgow, UK, 2008.

[10] Lunan, D., Need we protect Earth from space objects and if so, how?, *Space Policy* **8** (1992): 90–91.

[11] Melosh, H. J. and Nemchinov, I. V., Solar asteroid diversion, *Nature* **366** (1993): 21–22.

[12] Melosh, H. J., Nemchinov, I. V., and Zetzer, Y. I., Non-nuclear strategies for deflecting comets and asteroids, in *Hazard due to comets and asteroids*, edited by Gehrels, T., pp. 1111–1132, University of Arizona Press, 1994.

[13] Kahle, R., Kührt, E., Hahn, G., and Knollenberg, J., Physical limits of solar collectors in deflecting Earth-threatening asteroids, *Aerospace Science and Technology* **10** (2006): 253–263.

[14] Sanchez Cuartielles, J. P., Colombo, C., Vasile, M., and Radice, G., A multi-criteria assessment of deflection methods for dangerous NEOs, in *American Institute of Physics – New Trends in Astrodynamics and Applications III*, edited by Belbruno, E., pp. 317–333, 2007.

[15] ASTM E490–2000a(2006), Standard solar constant and zero air mass solar spectral irradiance tables, Technical report, American Society for Testing and Materials International, West Conshohocken PA, USA, 2006.

[16] Fröhlich, C., Solar irradiance variations, in *ISCS-2003 Symposium*, volume 535 of *ESA-SP*, pp. 183–193, Tatranskà Lomnica, Slovakia, 2003.

[17] Hedgepeth, J. M. and Miller, R. K., Structural concepts for large solar concentrators, Contractor report 4075, NAS1-17536, NASA Langley Research Center, 1987.

[18] Young, C. G., A sun-pumped CW one-watt laser, *Applied Optics* **5** (1966): 993-997.

[19] Brauch, U., Schall, W., and Wittwer, W., Hochleistunglaser für Raumfahrtaufgaben (High power laser for space duties), Technical Report 65, DLR Nachrichten, Institut für Technische Physik, Deutsche Forschungsanstalt für Luft- und Raumfahrt (DLR), Stuttgart, 1991.

[20] Shaltens, R. and Wong, W., Advanced Stirling technology development at NASA Glenn research center, Technical Report 44135-3191, NASA John H. Glenn Research Center, Cleveland, Ohio, 2007.

[21] Wua, Y.-T., Renb, J.-X., Guob, Z.-Y., and Liangb, X.-G., Optimal analysis of a space solar dynamic power system, *Solar Energy* **74** (2003): 205–215.

[22] Shaltens, R. and Mason, L., 800 hours of operational experience from a 2 kWe solar dynamic system, Technical Report NASA/TM–208840, NASA John H. Glenn Research Center, Cleveland, Ohio, 1999.

[23] Adbel-Hadi, Y. A.-F., *Development of optical concentrator systems for directly solar pumped laser systems*, PhD thesis, Technischen Universität Berlin, 2005.

[24] Weksler, M. and Shwartz, J., Solar-pumped solid-state lasers, *IEEE Journal of Quantum Electronics* **24** (1988): 1222–1228.

[25] Lando, M., Kagan, J., Linyekin, B., and Dobrusin, V., A solar-pumped Nd:YAG laser in the high collection efficiency regime, *Optics Communications* **222** (2003): 371-381.

[26] Landis, G. A., Prospects for solar pumped semiconductor lasers, in *Paper SPIE 2121-09, Laser Power Beaming, SPIE Proceedings Volume 2121*, pp. 58–65, Los Angeles CA, 1994.

[27] nLIGHT, nLIGHT demonstrates 73 percent wall-plug efficiency, Press Release, `http://www.nlight.net/news/releases`, 2006.

[28] Luque, A. et al., FULLSPECTRUM: A new PV wave making more efficient use of the solar spectrum, in *Nineteenth European Photovoltaic Solar Energy Conference and Exhibition*, Paris, France, 2004.

[29] NASA Near Earth Object program, 99942 Apophis (2004 MN4) impact risk, Online database, `http://neo.jpl.nasa.gov/risk/a99942.html`, 2008.

[30] Delbò, M., Cellino, A., and Tedesco, E., Albedo and size determination of potentially hazardous asteroids: (99942) Apophis, *Icarus* **188** (2007): 266-269.

[31] Schaub, H. and Junkins, J. L., *Analytical mechanics of space systems*, AIAA Education Series, Virginia, U.S.A., first edition, 2003.

[32] Battin, R. H., *An Introduction to the Mathematics and Methods of Astrodynamics*, AIAA Education Series, revised edition, 1999.

[33] Hu, W. and Scheeres, D. J., Spacecraft motion about slowly rotating asteroids, *Journal of Guidance, Control and Dynamics* **25** (2002): 765–775.

[34] Rossi, A., Marzari, F., and Farinella, P., Orbital evolution around irregular bodies, *Earth, Planets, Space* **51** (1999): 1173–1180.

[35] Song, Y.-J., Park, J.-Y., and Choi, K.-H., Optimal deflection of Earth-crossing object using a power limited spacecraft, in *17th AAS/AIAA Space Flight Mechanics Meeting*, Sedona, AZ, 2007, American Astronautical Society.

[36] Maddock, C. and Vasile, M., Design of optimal spacecraft-asteroid formations through a hybrid global optimization approach, *Journal of Intelligent Computing and Cybernetics* **1** (2008): 239–268.

[37] Vasile, M., *Multi-Objective Memetic Algorithms*, chapter Hybrid Behavioral-Based Multiobjective Space Trajectory Optimization, Studies in Computational Intelligence, Springer, 2008.

[38] Petropoulos, A., Simple control laws for low-thrust orbit transfers, in *AIAA/AAS Astrodynamics Specialists' Conference*, Montana, U.S.A., 2003, AIAA.

[39] Vallado, D. A., *Fundamentals of Astrodynamics and Applications*, The Space Technology Library, Microcosm Press and Kluwer Academic Publishers, 2nd edition, 2004.

[40] Hexi, B. and McInnes, C. R., Solar sail equilibria in the elliptical restricted three-body problem, *Journal of Guidance, Control and Dynamics* **29** (2006): 538–543.

[41] Morimoto, M., Yamakawa, H., and Uesugi, K., Artificial equilibrium points in the low-thrust restricted three-body problem, *Journal of Guidance, Control and Dynamics* **30** (2007): 1563–1568.

[42] Baig, S. and McInnes, C., Artificial three-body equilibria for hybrid low-thrust propulsion, *Journal of Guidance, Control and Dynamics* **31** (2008).

[43] Wie, B., *Space Vehicle Dynamics and Control*, Education Series, AIAA, 1998.

[44] Kubota, T. et al., An autonomous navigation and guidance system for MUSES-C asteroid landing, *Acta Astronautica* **52** (2003): 125-131.

[45] Xiangyu, H., Hutao, C., and Pingyuan, C., An autonomous optical navigation and guidance for soft landing on asteroids, *Acta Astronautica* **54** (2004): 763-771.

[46] Chung, L. R., Orbit determination methods for deep space drag-free controlled laser interferometry missions, MSc thesis, University of Maryland, Maryland, USA, 2006.

[47] Bennett, H. E., United States patent 6914232: Device to control laser spot size, 05 July 2005.

[48] Freeland, R. E., Bilyeu, G. D., Veal, G. R., Steiner, M. D., and Carson, D. E., Large inflatable deployable antenna flight experiment results, *Acta Astronautica* **41** (1997): 267–277.

[49] Chmielewski, A. B., Noca, M., and Ulvestad, J., ARISE antenna, *IEEE Aerospace Conference Proceedings* **7** (2000): 439–445.

[50] Bekey, I., Very large yet extremely lightweight space imaging systems, in *Highly Innovative Space Telescope Concepts*, edited by MacEwen, H. A., volume 4849, pp. 17–27, SPIE, 2002.

[51] Arslanturk, C., Optimum design of space radiators with temperature-dependent thermal conductivity, *Applied Thermal Engineering* **26** (2006): 1149–1157.

[52] Carpenter, B. and Lyons, J., Lightweight flexible solar array experiment summary, Technical report, Preliminary Technology and Science Validation Report, NASA Goddard Space Flight Center, 2002.

[53] Tribble, A. C., *The Space Environment*, Princeton University Press, revised edition, 2003.

[54] Broz, M., *Yarkovsky Effect and the Dynamics of the Solar System*, PhD thesis, Faculty of Mathematics and Physics, Astronomical Institute, Charles University, Prague, Czech Republic, 2006.

[55] Scrutton, P., Sorel, M., Hutchings, D., Aitchison, J., and Helmy, A., Characterizing bandgap gratings in GaAs:AlAs superlattice structures using interface phonons, *IEEE Photonics Technology Letters* **19** (2007): 677–679.

[56] Vasile, M., A multi-mirror solution for the deflection of dangerous NEOs, *Communications in Nonlinear Science and Numerical Simulation* **10.1016** (2008).

[57] Vasile, M., Maddock, C., and Radice, G., Mirror formation control in the vicinity of an asteroid, in *AIAA/AAS Astrodynamics Specialist Conference and Exhibit (AIAA 2008-6252)*, Honolulu, Hawaii, 2008.

[58] Maddock, C., Sanchez Cuartielles, J. P., Vasile, M., and Radice, G., Comparison of single and multi-spacecraft configurations for NEA deflection by solar sublimation, in *American Institute of Physics – New Trends in Astrodynamics and Applications III*, edited by Belbruno, E., pp. 303–316, 2007.

[59] Colombo, C., Sanchez Cuartielles, J. P., Vasile, M., and Radice, G., A comparative assessment of different deviation strategies for dangerous NEO, in *56th International Astronautical Conference Proceedings*, Valencia, Spain, 2006.

[60] Lappas, V. et al., Micro solar sail for Earth magnetotail monitoring, *Journal of Spacecraft and Rockets* **44** (2007): 840–848.